



OTTO VON GUERICKE  
UNIVERSITÄT  
MAGDEBURG

VST

FACULTY OF PROCESS  
AND SYSTEMS ENGINEERING

**Otto von Guericke University of Magdeburg**

**Faculty of Process and Systems Engineering**

## **Master Thesis**

from

Bansidhar Kanubhai Patel

**Application of Loewner framework for data-driven  
modeling and diagnosis of polymer electrolyte membrane  
fuel cells**

Supervisors:

M.Sc. Antonio Sorrentino

Dr. Ion Victor Gosea (DRI Group, MPI)

Examiners:

Prof. Dr.-Ing. habil. Kai Sundmacher

Dr.-Ing. habil. Tanja Vidakovic-Koch

Date of Submission:

17.12.2020

Date of Defense:

26.01.2021

## **Task Description**



## **Declaration**

I hereby declare that I prepared the work submitted without inadmissible assistance and without the use of any aids others than those indicated. Fact or ideas taken from other sources, either directly or indirectly have been marked as such. Further, I have not made payments to third parties either directly or indirectly for any work connected with the contents of the submitted thesis.

The work has not so far submitted either in Germany or abroad in same or similar form as a Bachelor-/Master thesis and has also not yet been published as a whole.

Magdeburg, 17.12.2020

Bansidhar Patel

## Abstract

Environmental and resources problems have been the driving force behind the development of fuel cell technologies. The polymer electrolyte membrane fuel cell (PEMFC) is one of the highly promising fuel cells in terms of delivering energy requirements for a vast number of applications. Nevertheless, its commercialization has been restricted because of its limited durability and reliability. In order to enhance its performance, effective modelling, and diagnostic strategies are essential. Several technologies are employed to investigate the various degradation mechanisms occurring in the PEMFC. Among them, electrochemical impedance spectroscopy (EIS) is the most widely employed method. Nevertheless, it is not able to distinguish processes having a similar time constant, and thus alternative frequency response analysis (FRA) techniques have recently been developed involving non-electrical inputs and/or outputs, for instance, the concentration-alternating frequency response analysis (cFRA). However, these methodologies have required a longer period of experiments and their results are difficult to interpret, which requires complex models to understand them.

In order to tackle such challenges, the data-driven based approach, known as the Loewner Framework, is adopted in this thesis. Applying the Loewner framework, a new methodology is developed as a complementary analysis technique for interpreting EIS and cFRA data of the PEMFC. This novel method allows the identification of the different features of the individual physicochemical phenomena in a very clear manner and facilitates the decoupling of processes with comparable time constants. In addition, the cFRA experiment data are analysed by using the Loewner framework in order to shorten the duration of the experiments, and the results show the feasibility of a significant amount of time reduction of the cFRA experiments.

# Contents

Task Description .....	ii
Declaration .....	iv
Abstract .....	v
Contents .....	vi
List of Figures.....	viii
List of Tables.....	xi
Notation.....	xii
Abbreviations .....	xiv
1 Introduction.....	1
1.1 Outline of the thesis .....	2
2 Theoretical Background .....	4
2.1 Fuel cell technologies .....	4
2.2 Principle of PEMFC functioning.....	4
2.3 Dynamics of PEMFC.....	7
2.4 Electrochemical impedance spectroscopy (EIS).....	8
2.5 Concentration-alternating frequency response analysis (cFRA).....	9
2.5.1 Theoretical background and data analysis of cFRA .....	9
2.5.2 Strategy to decouple concentration inputs contribution .....	11
3 Methodology .....	12
3.1 The Loewner framework for linear systems .....	12
3.1.1 Development of the Loewner interpolation framework: .....	12
3.1.2 The Loewner pencil .....	16
3.1.3 Construction of reduced order models.....	17
3.2 Algorithm.....	18
3.3 Method validation with simple RLC circuit .....	21
4 EIS .....	23
4.1 Analysis of impedance spectra of PEMFC .....	23
4.2 Allocating the distribution of characteristic frequency peaks .....	25
4.3 Variation of the operating conditions .....	28

4.3.1	Variation of current density in the case of H <sub>2</sub> and air as inputs: .....	31
4.3.2	Variation of humidity in the case of H <sub>2</sub> and O <sub>2</sub> as inputs:.....	32
4.4	Analysis of simulated EIS spectra .....	34
5	cFRA .....	37
5.1	Analysis of cFRA experimental data .....	37
5.2	cFRA experimental time reduction .....	41
5.2.1	Confirmation with similar cFRA experimental data .....	42
5.3	cFRA O <sub>2</sub> .....	44
5.4	cFRA H <sub>2</sub> O.....	47
6	Conclusion and Future Suggestions .....	49
6.1	Conclusion .....	49
6.2	Future suggestions .....	50
7	References.....	51
8	Appendix.....	55
8.1	Fourier transform (FT) .....	55
8.1.1	Real and complex versions of transforms .....	55
8.1.2	Fast Fourier transform (FFT) .....	58
8.1.3	Interpreting the FFT results.....	58
8.2	Experimental parameters and model description .....	59
8.2.1	Experimental parameters.....	59
8.2.2	Model description .....	60
8.3	Different verifications.....	63

## List of Figures

Figure 2.1: The schematic representation of a PEMFC operation [9].....	5
Figure 2.2: Polarization characteristic curve for a PEMFC with different voltage losses [14]..	6
Figure 2.3: Overview of the wide range of dynamic processes in PEMFC [15]. .....	7
Figure 2.4: Principle of the EIS [15]. .....	8
Figure 2.5: Scheme of the cFRA experimental setup [4].....	10
Figure 3.1: RLC circuit .....	21
Figure 3.2: (a) Bode plot of RLC circuit, (b) Nyquist plot of RLC circuit, (c) Singular value decay of the Loewner matrix, (d) Frequency response comparison – state space model, (e) Model residuals, (f) Corresponding time constant spectrum. ....	22
Figure 4.1: Impedance spectra of PEMFC operated with Air and $T = 80^{\circ}\text{C}$ , $\text{RH}=33\%$ and $j=300\text{ mA cm}^{-2}$ . (a) Bode plot, (b) Nyquist plot, (c) The DCF spectra, and (d) Real part of the DCF spectra.....	23
Figure 4.2: (a1-a4) The DCF spectra for different values of order $k$ , (b1-b4) respective residual.....	24
Figure 4.3: Frequency response comparisons with the state space model of different model order $k$ (a-d).....	25
Figure 4.4: Impedance spectra of PEMFC operated with Air and $T = 80^{\circ}\text{C}$ , $\text{RH}=33\%$ and $j=300\text{ mA cm}^{-2}$ . (a) Magnitude spectra, (b) Imaginary part of spectra, (c) Nyquist plot, and (d) Relative residuals. ....	26
Figure 4.5: (a) The DCF spectra correspond to Impedance spectra in Figure 4.4, (b) Real part of the DCF spectra. ....	26
Figure 4.6: (a) Magnitude spectra, (b) Imaginary part of spectra, (c) Nyquist plot, and (d) Relative residuals. Impedance spectra of PEMFC operated with air and $T = 80^{\circ}\text{C}$ , $\text{RH} = 33\%$ , and $j=300\text{ mA cm}^{-2}$ are shown as blue data; impedance spectra of PEMFC operated with pure $\text{O}_2$ and $T = 80^{\circ}\text{C}$ , $\text{RH} = 33\%$ , and $j=300\text{ mA cm}^{-2}$ are displayed as black data; impedance spectra of PEMFCs operated at pure $\text{O}_2$ and $T = 80^{\circ}\text{C}$ , $\text{RH} = 55\%$ , and $j=300\text{ mA cm}^{-2}$ are represented as pink data.....	29
Figure 4.7: (a) The DCF spectra correspond to Impedance spectra in Figure 4.6, (b) Real part of the DCF spectra. ....	29
Figure 4.8: Variation of the current density ( $100$ to $300\text{ mA cm}^{-2}$ ) of PEMFC operated with air and $T = 80^{\circ}\text{C}$ , $\text{RH}=33\%$ . (a) Magnitude spectra, (b) Imaginary part of spectra, (c) Nyquist plot, and (d) Relative residuals. ....	32
Figure 4.9: (a) The DCF spectra correspond to Impedance spectra in Figure 4.8, (b) Real part of the DCF spectra. ....	32
Figure 4.10: Variation of the relative humidity ( $33$ to $55\%$ ) of PEMFC operated with pure $\text{O}_2$ and $T = 80^{\circ}\text{C}$ , $j=300\text{ mA cm}^{-2}$ . (a) Magnitude spectra, (b) Imaginary part of spectra, (c) Nyquist plot, and (d) Relative residuals.....	33
Figure 4.11: (a) The DCF spectra correspond to Impedance spectra in Figure 4.10, (b) Real part of the DCF spectra. ....	33



Figure 4.12: Experimental (a, c, e) and simulated (b, d, f) EIS spectra of PEMFC operated with air and $T = 80^{\circ}\text{C}$ , $\text{RH}=33\%$ for 100, 200, and 300 $\text{mA cm}^{-2}$ . Magnitude spectra (a, b), Imaginary part of spectra (c, d), and Nyquist plot (e, f).....	35
Figure 4.13: The DCF spectra correspond to EIS spectra in Figure 4.12 (a, c), a Real part of the DCF spectra (b, d). The experimental (a, b) and simulated (c, d) spectra. ....	35
Figure 5.1: The perturbation of the input (oxygen partial pressure) and the corresponding output response (electrical potential) as periodic signals for data set no. 1, 8, and 17 (a-c). ....	38
Figure 5.2: Fourier transform amplitude spectra correspond to the periodic signals in Figure 5.1 (a-c).....	39
Figure 5.3: Dominant Frequencies of the Input and Output signals for all data sets.....	40
Figure 5.4: Magnitude spectra of galvanostatic cFRA $\text{O}_2$ .....	40
Figure 5.5: Procedure for identifying the best group of six data sets among 12376 possible groups that approximate the response of all 17 data sets. ....	41
Figure 5.6: Frequency range vs root-mean-square error.....	42
Figure 5.7: Dominant frequencies of the input and output signals for six data sets.....	43
Figure 5.8: Magnitude spectra of galvanostatic cFRA $\text{O}_2$ for both all-17 data sets and six data sets. ....	43
Figure 5.9: Experimental cFRA $\text{O}_2$ spectra under galvanostatic (a-b) and voltastatic (c-d) control for 100, 200, and 300 $\text{mA cm}^{-2}$ . ....	45
Figure 5.10: The DCF spectra correspond to cFRA $\text{O}_2$ spectra in Figure 5.9 (a, c), Real part of the DCF spectra (b, d).....	45
Figure 5.11: Simulated cFRA $\text{O}_2$ spectra under galvanostatic (a-b) and voltastatic (c-d) control for 100, 200, and 300 $\text{mA cm}^{-2}$ .....	46
Figure 5.12: Simulated DCF spectra correspond to cFRA $\text{O}_2$ spectra in Figure 5.11 (a, c), Real part of the DCF spectra (b, d).....	46
Figure 5.13: Experimental (a-b) and simulated (c-d) cFRA $\text{H}_2\text{O}$ spectra under galvanostatic control for 100, 200, and 300 $\text{mA cm}^{-2}$ . ....	47
Figure 5.14: The DCF spectra correspond to cFRA $\text{H}_2\text{O}$ spectra in Figure 5.13 (a, c), Real part of the DCF spectra (b, d). The experimental (a, b) and simulated (c, d) spectra. ....	48
Figure 8.1: Four types of Fourier transforms [43].....	55
Figure 8.2: Real and complex DFT [44].....	56
Figure 8.3: Interpretation of frequencies in complex DFT output [44]. ....	57
Figure 8.4: A scheme of a PEMFC [3]. ....	60
Figure 8.5: Relative residuals corresponding to the experimental (a) and simulated (b) EIS spectra in Figure 4.12. ....	63
Figure 8.6: Magnitude spectra of galvanostatic cFRA $\text{O}_2$ for both all-17 data sets and six data sets (Verification with other cFRA experimental data).....	63
Figure 8.7: Original data of Experimental cFRA $\text{O}_2$ spectra shown in Figure 5.9 (a-b) under galvanostatic control for 100, 200, and 300 $\text{mA cm}^{-2}$ .....	64
Figure 8.8: Original data of Experimental cFRA $\text{O}_2$ spectra shown in Figure 5.9 (c-d) under voltastatic control for 100, 200, and 300 $\text{mA cm}^{-2}$ .....	64
Figure 8.9: Original data of Experimental cFRA $\text{H}_2\text{O}$ spectra shown in Figure 5.13 (a-b) under galvanostatic control for 100, 200, and 300 $\text{mA cm}^{-2}$ .....	65

Figure 8.10: Relative residuals corresponding to the experimental (a, c, e) and simulated (b, d, f) cFRA spectra shown in Figure 5.9, Figure 5.11, and Figure 5.13. (a, b) cFRA O<sub>2</sub> under galvanostatic control, (c, d) cFRA O<sub>2</sub> under voltastatic control, and (e, f) cFRA H<sub>2</sub>O under galvanostatic control..... 65

# List of Tables

Table 2.1: Different types of fuel cell [10]..... 4  
Table 8.1: Normal operating conditions of the PEMFC..... 59  
Table 8.2: Balance equations of the cell. .... 61  
Table 8.3: Constitutive equations. .... 61  
Table 8.4: Boundary conditions..... 62  
Table 8.5: Model parameters..... 63

# Notation

**For main part of the thesis:**

## List of symbols

$\mathbb{C}$	Set of complex numbers
$\mathbb{R}$	Set of real numbers
$\mathbb{R}^{n \times m}$	Set of real valued matrices with n rows and m columns
$X$	Matrix (in general) of size $n \times m$
$X^T$	Transpose of a matrix $X$
$X^*$	Conjugate transpose (or Hermitian transpose) of a matrix $X$
$rank(X)$	Rank of a matrix $X$
$diag(x)$	Diagonal matrix with the vector $x$ on its diagonal
$Z$	Impedance
$\zeta$	cFRA transfer function
$k$	Order (or dimension) of the matrix
$\omega$	Angular frequency, $\text{rad s}^{-1}$

**For model in Appendix:**

## List of symbols

$A$	Area of the electrode, $\text{m}^2$
$C_{dl}$	Double layer capacity, $\text{F m}^{-2}$
$D_{i,air}$	Diffusivity in the air, $\text{m}^2 \text{s}^{-1}$
$D_W$	Diffusivity of water in Nafion, $\text{m}^2 \text{s}^{-1}$
$F$	Faraday constant, $\text{C mol}^{-1}$
$F_\alpha$	Volumetric flow, $\text{m}^3 \text{s}^{-1}$
$J_\alpha$	Diffusive flux, $\text{mol m}^2 \text{s}^{-1}$
$K_M$	Electro-osmotic flow constant
$K_{H_2,ad}$	Hydrogen adsorption constant, $\text{Pa}^{-1/2}$
$K_{HOR}$	Hydrogen oxidation constant, $\text{mol m}^{-2} \text{s}^{-1}$
$i$	Current density, $\text{A m}^{-2}$
$i_0$	Exchange current density, $\text{A m}^{-2}$
$M_M$	Molecular weight of the membrane, $\text{Kg m}^{-3}$
$N_W$	Water flux through the membrane, $\text{mol m}^{-2} \text{s}^{-1}$
$P_\alpha$	Partial pressure, Pa
$r_{HOR}$	Reaction rate of hydrogen oxidation reaction, $\text{mol m}^{-2} \text{s}^{-1}$
$r_{ORR}$	Reaction rate of oxygen reduction reaction, $\text{mol m}^{-2} \text{s}^{-1}$
$R$	Universal gas constant, $\text{J mol}^{-1} \text{K}^{-1}$
$t_{ccl}$	Catalyst layer thickness, m
$V$	Volume of the channel, $\text{m}^3$
$U$	Potential, V

$x$	Sandwich coordinate, m
$y$	Axial coordinate, m
$\alpha$	Charge transfer coefficient
$\eta$	Over potential, V
$k_M$	Conductivity of the membrane, S m <sup>-1</sup>
$\lambda$	Water content
$\xi$	Electro-osmotic constant
$\rho_{H_2O}$	Water density, kg m <sup>-3</sup>

### Superscripts

$a$	Anode
$c$	Cathode
$CH$	Channel
$CL$	Catalyst layer
$eff$	Effective value
$GDL$	Gas diffusion layer

### Subscripts

$ccl$	Cathode catalyst layer
$dl$	Double layer
$HOR$	Hydrogen oxidation reaction
$in$	Incoming
$M$	Nafion membrane
$ORR$	Oxygen reduction reaction
$out$	Out coming
$W$	Water
$\alpha$	General component

## Abbreviations

PEMFC	Polymer Electrolyte Membrane Fuel Cell
EIS	Electrochemical Impedance Spectroscopy
FRA	Frequency Response Analysis
cFRA	Concentration- alternating Frequency Response Analysis
DCF	Distribution of the Characteristic Frequency
TF	Transfer Function
GDL	Gas Diffusion Layer
DRT	Distribution of the Relaxation Time
SVD	Singular Value Decomposition
FFT	Fast Fourier Transform
HOR	Hydrogen Oxidation Reaction
ORR	Oxygen Reduction Reaction
RMSE	Root Mean Square Error
DFT	Discrete Fourier Transform
CH	Channel

# 1 Introduction

Increasing environmental and resource concerns have inspired the development and commercialization of fuel cell technologies. The polymer electrolyte membrane fuel cell (PEMFC) is one of the most promising fuel cells to meet the power and energy needs of a wide variety of applications, from portable electronics to transportation, especially mobile applications. However, their commercialization has been constrained by their high cost and limited durability. PEMFCs also have many complex and strongly coupled processes that determine performance and durability. One way to improve the performance, reliability, and durability of PEMFCs for practical purposes is to prevent them from going into faulty modes [1]. It has been realized that effective modelling and fault diagnosis strategies are needed to develop a better understanding of the processes that occur in fuel cells and to identify improved operating conditions [2].

Electrochemical impedance spectroscopy (EIS) is a commonly used characterization technique to study the complex dynamics of PEMFC. It is based on the excitation of the cell at a certain steady-state by a periodic electrical input (current or cell potential) and the detection of the resulting electrical response at different frequencies. Using a linear frequency response analysis (FRA) the input /output correlation is analysed by formulating a transfer function in the frequency domain. Electrochemical systems involve various transient processes characterized by different time constants, i.e. mass transport of the reagents and products in the different domains of the system, chemical and electrochemical reactions at the electrode-electrolyte interface, and adsorption of the reacting species. Electrical stimulation can identify almost all of these dynamic processes with different time constants in the cell and facilitate the exploration in a wide frequency range ( $10^6$ - $10^{-4}$  Hz). EIS has been applied to all types of electrochemical systems, such as batteries, electrolyzers, and corrosion systems [2]–[4].

However, some of the phenomena involved are strongly coupled in the EIS spectra, so that they do not allow the de-convolution of all sub-processes that occur in the fuel cell. Therefore, the interpretation of the patterns observed in the impedance spectra is not always unambiguous, so a proper understanding of the dynamics is often not possible. For this reason, in addition to EIS, new FRA experimental techniques have been suggested to study system dynamics by applying non-electrical inputs and/or outputs [2]–[4]. For example, a concentration-alternating frequency response analysis (cFRA) is proposed to study the dynamics of the electrochemical systems. In cFRA, a periodic change of a reactant or even product concentration is applied as an input. The most suitable electrical variable (current or potential) depending on the conditions under which the experiment is carried out (voltastatic or galvanostatic control) was considered as the output [3], [4]. While the application of EIS and cFRA techniques in laboratory environments has been well developed, however, their commercialization is challenging due to the duration of the experiments and

the complexity of their results, which require the use of complicated models for interpreting their spectra.

Hence, the model reduction of the dynamic system has become essential in order to substitute complex models (which are described by a large number of internal variables and processes) with less complex models that are easier to handle and have almost the same response characteristics with acceptable approximation errors [5]. For linear systems, there are several approaches available for model reduction. Among them, data-driven approaches have gained in importance, as they are involved in numerous applications. The central approach to data-driven model reduction is the Loewner framework, the details of which can be found in the following works [6]–[8].

Its main characteristic is that it provides a trade-off between the accuracy of fit and model complexity. Also, the Loewner framework offers a natural and direct way to construct models from measured or computed input/output data (e.g. measurements of the frequency response of the system) [5]. Its application for the analysis of input and output data of a PEMFC system could allow a significant amount of time reduction of the frequency response experiments and facilitate the interpretation of the corresponding frequency domain spectra at the same time. In this way, the application of this methodology as an online diagnostics tool in mobile applications becomes feasible.

The purpose of this master thesis is to apply the Loewner framework to the data collected during cFRA experiments and verify whether the duration of the test can be reduced. Besides, the obtained EIS and cFRA transfer functions will be used to obtain parameters related to the dynamic processes and degradation mechanisms that occur in the fuel cell during operation.

For this reason, the following tasks are performed:

- Development of a new methodology to analysed EIS and cFRA spectra in terms of distribution of characteristics frequency (DCF) analysis by using the Loewner framework.
- Analysis of EIS and cFRA experimental as well as simulated spectra.
- Investigation of the feasibility to shorten the time of cFRA experiments.

### 1.1 Outline of the thesis

After the overview of the motivation and the aim of this thesis in Chapter 1 as an introduction, the rest of the report is organized as follows.

Chapter 2 presents the theoretical background and information on the fuel cell technology particularly on the PEMFC, then the dynamics of the PEMFC, and the diagnostic and characterization techniques especially EIS and cFRA.

Chapter 3 introduces the methodology, which includes an overview of the Loewner framework for linear systems, followed by the different algorithms such as calculation of cFRA transfer functions (TFs) from time-domain input/output signals, the Loewner framework for constructing state-space models and reduced state-space models, and partial



fraction expansion of the transfer function to obtain gains and time constants. This chapter also shows the validation of methodology to calculate the gains and time constants of the system with a simple RLC circuit.

Chapter 4 comprises the analysis of the EIS spectra of the PEMFC employing the novel methodology and discussed several cases to study different dynamical processes and degradation phenomena that occur in the cell during operation.

Chapter 5 includes the analysis of the cFRA spectra of the PEMFC, possibilities to shorten the time of cFRA experiments, and the discussion of the cFRA spectra of the experiments as well as a numerical model by means of the new methodology.

Chapter 6 is a summary of the thesis as a conclusion and includes recommendations regarding future work.

## 2 Theoretical Background

### 2.1 Fuel cell technologies

A fuel cell is an electrochemical device that converts the chemical energy from fuel (hydrogen is the most common fuel) and an oxidant (mostly oxygen) into electrical energy, heat, and other reaction products [9]. Fuel cells offer a wide range of benefits for the environment and the balance of the energy structure. Due to their high efficiency and emission-free in-situ operation, fuel cells have the potential to drastically reduce greenhouse gas emissions in many applications [10].

There are different types of fuel cells. A very commonly used classification is based on the electrolyte. Basic information on these fuel cell technologies is summarized in Table 2.1 [10]. Among these, the PEMFC is currently the more studied technology due to its simplicity, viability, quick start-up, and wide range of applications [11]. This thesis focuses on the PEMFC.

**Table 2.1: Different types of fuel cell [10].**

Fuel cell type	Mobile ion	Operating temperature	Applications and notes
Alkaline (AFC)	$\text{OH}^-$	50–200°C	Used in space vehicles, e.g. Apollo, Shuttle
Proton exchange membrane (PEMFC)	$\text{H}^+$	30–100°C	Vehicles and mobile applications, and for lower power CHP systems
Direct methanol (DMFC)	$\text{H}^+$	20–90°C	Suitable for portable electronic systems of low power, running for long times
Phosphoric acid (PAFC)	$\text{H}^+$	~220°C	Large numbers of 200-kW CHP systems in use
Molten carbonate (MCFC)	$\text{CO}_3^{2-}$	~650°C	Suitable for medium to large-scale CHP systems, up to MW capacity
Solid oxide (SOFC)	$\text{O}^{2-}$	500–1000°C	Suitable for all sizes of CHP systems, 2kW to multi-MW

### 2.2 Principle of PEMFC functioning

As Figure 2.1 shows, a typical PEMFC is constituted by different components [9]–[11]:

- **A porous anode:** This typically comprises catalyst particle layers and a gas diffusion layer (GDL). Where the gaseous fuel (hydrogen) diffuses through the anode pores to reach the polymer membrane interface. There, catalyst particles catalyse the oxidation of the fuel, electrons are conveyed by an external circuit from the anode to

the cathode, and the produced ions are transported to the cathode through the electrolyte.

- **A porous cathode:** Where oxidant diffuses through the cathode pores to reach the polymer membrane interface and catalyst particle catalyses its reduction reaction.
- **Polymer membrane:** Which is an electrolyte impermeable to gases but good conductor of protons.
- **The bipolar plates:** Which convey the reactants to the electrodes, evacuates the reactants in excess and the product of the reaction (water), and also act as the electrical conductors and heat conductors. Moreover, they provide structural support for fuel cells.
- **Silicon seals:** Which prevent leakage of gas and cooling fluid.

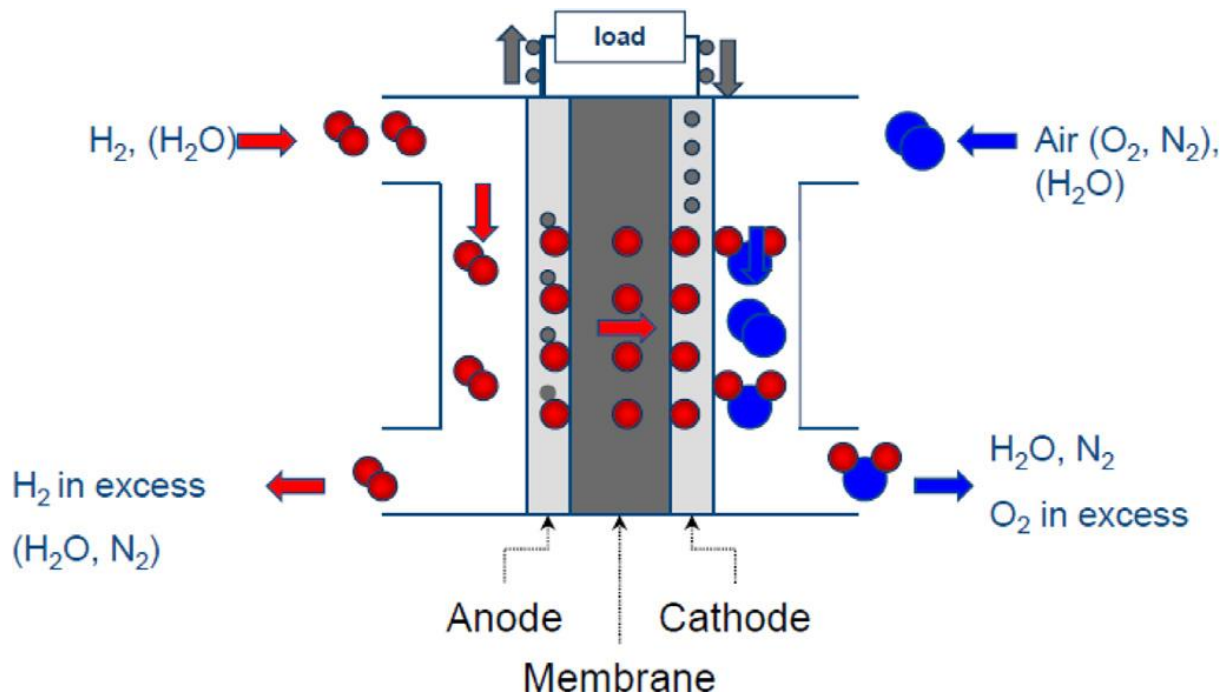
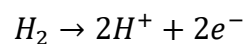
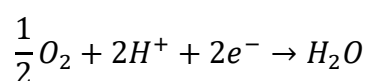


Figure 2.1: The schematic representation of a PEMFC operation [9].

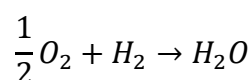
A running PEMFC is usually fed continuously on the anode side with hydrogen, and on the cathode side with air. Electrochemical reactions take place at the electrode-membrane interfaces. Hydrogen is oxidized on the anode side:



Protons transfer through the membrane, while the electrons flow through the external electric circuit where they perform electrical work and return to the cathode side, where oxygen is reduced:



Combined the reactions on the anode and cathode sides, the global reaction is



With the conversion of chemical energy to electrical energy and heat, the by-product water is generated and mostly evacuated with the unreacted air from the cathode side.

In general, there are three main contributors to voltage losses that determine the performance of the PEMFC. The first one is the activation losses, which are caused by the slow kinetics of the redox reactions. The main part of the kinetic activation losses in a PEMFC is due to the slow reduction of the oxygen at the cathode. The hydrogen oxidation at the anode is a fast reaction and only contributes very little to the voltage loss. However, these losses are dominant at low current density [12]. The second one is the Ohmic losses because of the resistance associated with the proton transport across the membrane and the electron transport through the electrodes, gas diffusion layers, bipolar plates, and the external circuit. This dominates at moderate current densities. The voltage drop due to this contribution is almost linear [9], [12]. Finally, concentration losses are a result of the drop in the concentration of the reactants at the electrodes, in the GDL, and along the gas channel, that dominates at high current density [9].

Figure 2.2 depicts an example of a polarization characteristic curve for a PEMFC with different voltage losses. The polarization characteristic curve indicates the internal voltage losses of the fuel cell at a specific current density. The effects of parameters such as feed compositions, flow rate, temperature, or the relative humidity of the feeds on the fuel cell performance can be investigated by measuring the polarisation characteristic curve at different operating conditions [13].

However, the voltage losses of the individual phenomena overlap at the respective operating point and the polarization characteristic curve can only represent the sum of these effects. Besides, the polarization characteristic curve reflects only the quasi-static behaviour of the PEMFC, which cannot give any information about the dynamic behaviour of the system [9].

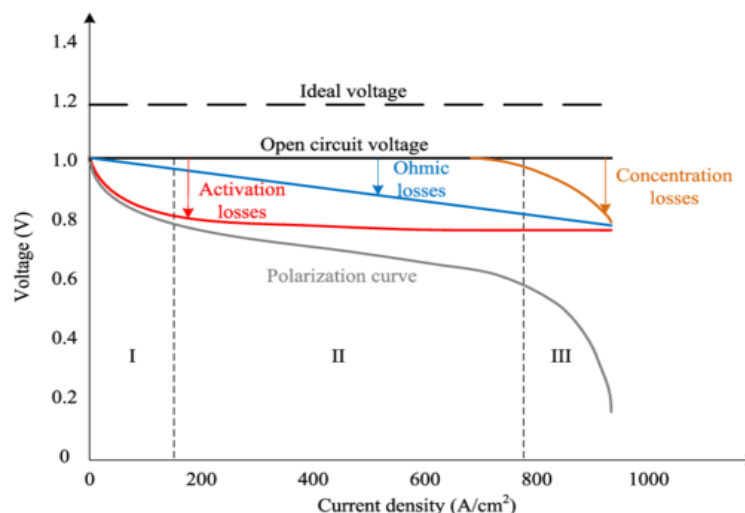


Figure 2.2: Polarization characteristic curve for a PEMFC with different voltage losses [14].

## 2.3 Dynamics of PEMFC

Different phenomena (electrical, electrochemical, mass transport, and thermal) occur that make a fuel cell a highly multi-physics object. Additionally, these phenomena have very different time response characteristics. The fastest concerns the electrochemical double-layer charging or discharging at the electrode-membrane interfaces. Depending on the capacity, the time constant is in the range of micro- or milliseconds. Then comes the charge transfer associated with the electrochemical reactions (oxidation and reduction), the gas transport through the electrodes (or the channel and the GDL), typically on a timescale of a few seconds, and the membrane hydration which occurs on a timescale of seconds or several minutes depending on the operating conditions of the fuel cell. Among the slowest processes, the electrodes poisoning by impurities in the reactants (usually carbon monoxide (ppm range)) or by an oxide layer formed on a time-scale of minutes to hours, and the thermal changes which can occur within minutes or hours and are determined by the thermal properties of the fuel cell materials, reactant gas flow rates, ambient temperature, etc. Finally, structural changes to the electrodes and electrolytes can occur during the long-term operation at certain operating conditions, leading to irreversible degradation of performance [9], [15].

Figure 2.3 describes the various dynamic processes in PEMFCs, as explained above, which cover the approximate time range from microseconds to years from  $10^{-6}$  s to  $10^8$  s. A fuel cell is not only multi-physics, but also a temporally and spatially multi-scale and coupled object. To sum up, in one word, a fuel cell is a complex system [9].

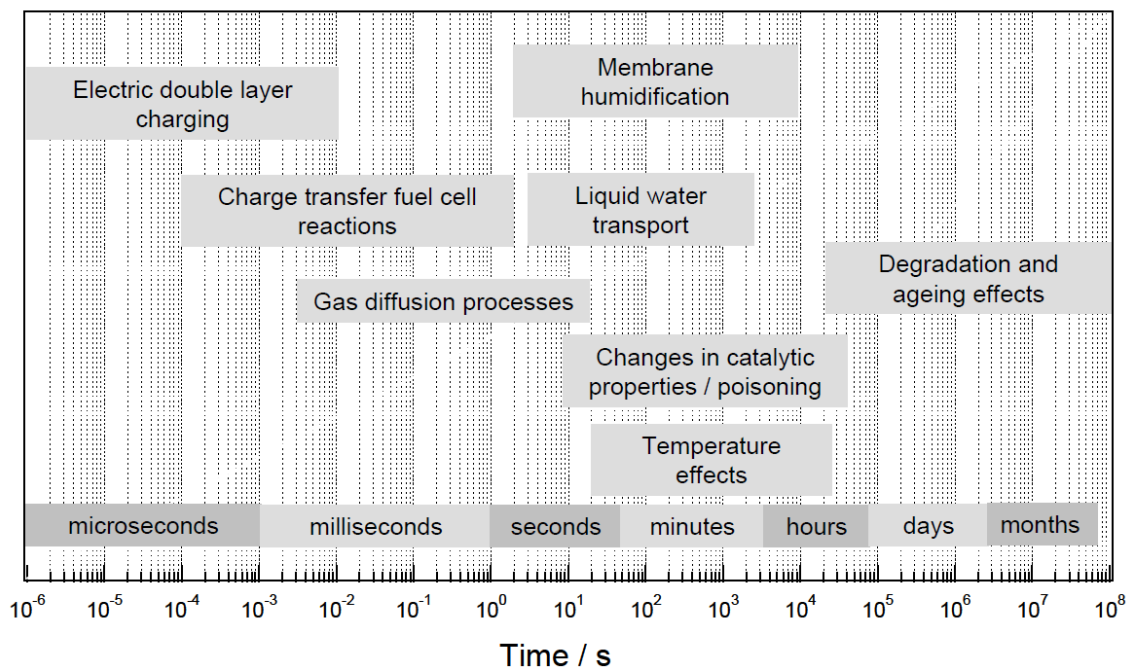


Figure 2.3: Overview of the wide range of dynamic processes in PEMFC [15].

## 2.4 Electrochemical impedance spectroscopy (EIS)

In principle, there are several diagnostic and characterization techniques available to study the complex behaviour of PEMFCs to improve performance and durability [15], [16]. Among them, the most popular and widely employed method is electrochemical impedance spectroscopy (EIS). EIS is based on the frequency response analysis (FRA) which provides detailed diagnostic information on a wide range of physicochemical phenomena, such as the charge transfer reaction at the electrode/electrolyte interface, reaction mechanisms, state of charge of batteries, electrode material properties and state of health of fuel cells, etc. [12], [17].

The principle of the EIS is displayed in Figure 2.4. In the EIS, an electrochemical system is excited using a sinusoidal electrical input (current or cell potential) over the frequency range of interest, usually from 1 mHz to 100 kHz, and the resulting electrical output is measured [17]. Thus, the corresponding transfer functions can be determined, commonly known as impedance/admittance. The analysis of the resulting EIS spectra reveals information on specific electrochemical phenomena that occur there. For a valid analysis, the amplitude of the electrical stimulation has to be sufficiently small to produce a linear response.

However, the EIS is often not able to distinguish the individual contribution of processes with similar time constants, thus it complicates the interpretation of the spectra and useful quantitative analysis. Because of this, other alternative approaches have been suggested, which are intended to decouple the individual contribution of the processes. For example, the distribution of the relaxation time (DRT) [18]–[22], the nonlinear EIS [23], [24], and total harmonic distortion analysis [25]. Among them, DRT has gained popularity in the past few years.

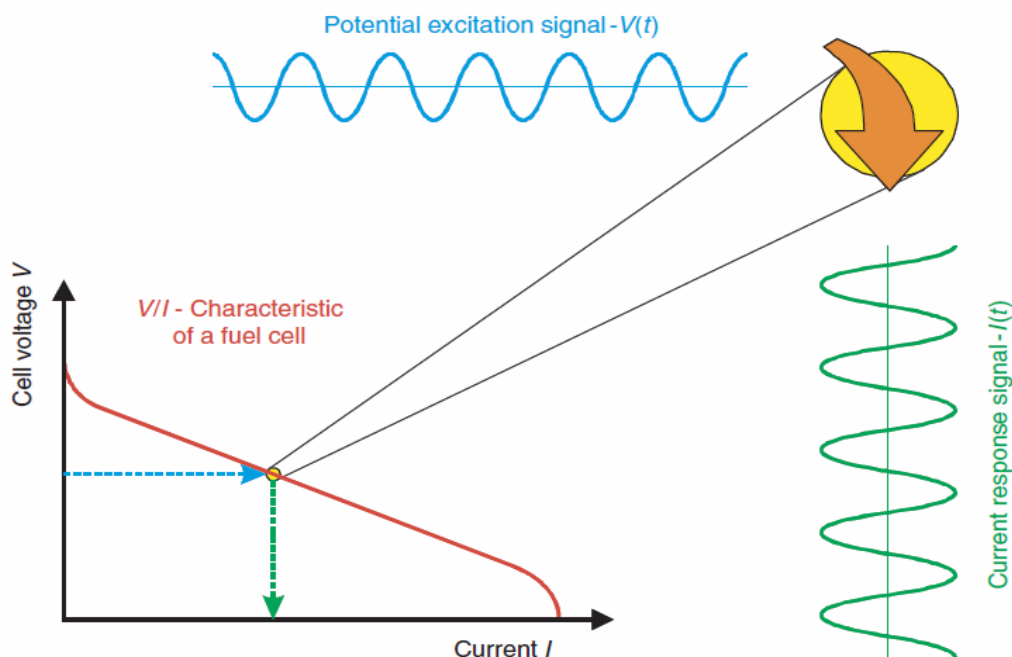


Figure 2.4: Principle of the EIS [15].

## 2.5 Concentration-alternating frequency response analysis (cFRA)

In recent years several groups have suggested FRA techniques based on non-electrical inputs and/or outputs to study the dynamics of the PEMFC system [2]–[4], [16], [26]. The use of back pressure as an input variable has recently been proposed to study the transport phenomena in the PEMFC [2], [26]. Among the others, the work of Engebretsen et al. [2] who suggested a transfer function involving perturbations of the cathode backpressure as input and the cell potential as output. It is shown that the technique can be used to distinguish the explicit effect of water management from reactant starvation when a PEMFC is operated at different reactant humidification conditions.

Recently, a new FRA technique named concentration-alternating frequency response analysis (cFRA) has proposed by Sorrentino et al. [3], [4], which is based on transfer functions depending on partial pressure perturbations of specific reactants. It was in their theoretical work shown that cFRA spectra could discriminate the different dynamic processes occurring in the cell, depending on the type of concentration perturbation (oxygen or water partial pressure), and electric control (voltastatic or galvanostatic) applied. In another communication by the same group [4], first experiments with the cFRA technique were reported with a laboratory-scale PEMFC. The analysis of the measured transfer functions unravels various aspects related to gas and water transport in the different layers of the cell. And it has also been shown that the cFRA method can be used to diagnose problems associated with cathode humidification state.

### 2.5.1 Theoretical background and data analysis of cFRA

The schematic diagram of the cFRA experimental setup including the cathode feed conditioning section is displayed in Figure 2.5. In addition, the periodic input signals (oxygen pressure) and electric output signals (cell potential or current) at two different frequencies are shown in the insets. Here all experimental tests were performed using a single PEMFC having an active area of 25.8 cm<sup>2</sup> and a detailed description about cFRA experimental setup can be found in Sorrentino et al. [4].

The correlation between pressure input and electric output at different frequencies is analysed through linear FRA by determining a proper transfer function. The cFRA transfer functions for the perturbation of a specific component  $\alpha$  under voltastatic or galvanostatic control read as follows:

$$\zeta_{\alpha}^V = \frac{\Delta I(j\omega)}{\Delta P_{\alpha}(j\omega)} \quad (2.1)$$

$$\zeta_{\alpha}^I = \frac{\Delta V(j\omega)}{\Delta P_{\alpha}(j\omega)} \quad (2.2)$$

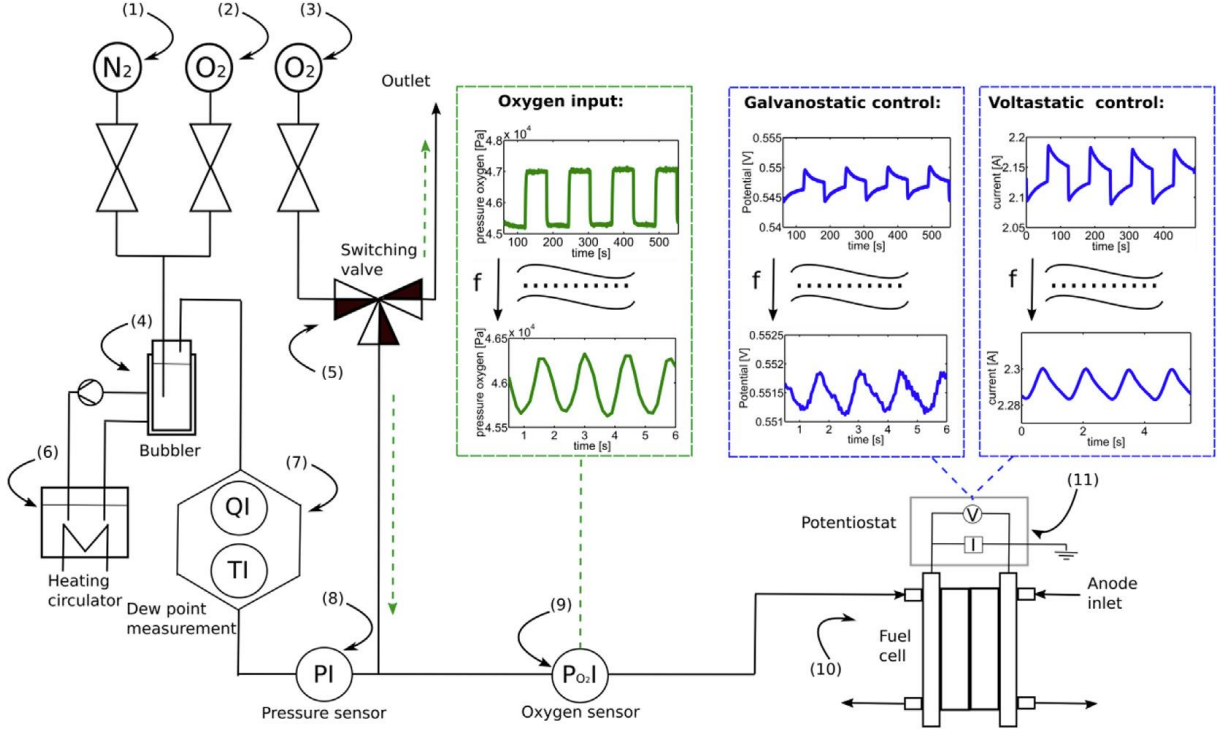


**Figure 2.5: Scheme of the cFRA experimental setup [4]**

When analysing the data, however, it must be taken into account that in the present experimental setup (see Figure 2.5) the periodic addition of the small oxygen flow after the bubble humidifier induces not only a change in the oxygen pressure but also a variation in the water vapour pressure. An increase in the oxygen partial pressure leads to a complementary decrease in the partial pressure of water and vice versa, which leads to a simultaneous periodic stimulation in which both concentration inputs ( $O_2$  and  $H_2O$ ) are in antiphase. This further shows that the experimentally obtained cFRA transfer functions are mixed transfer functions that contain contributions of the pure transfer functions of both  $O_2$  and  $H_2O$  [4].

By measuring the variation of the oxygen pressure and the electrical output at each frequency  $f$  according to the disclosed facts in place of the theoretical cFRA transfer functions (eqs. (2.1) and (2.2)), the following mixed oxygen cFRA transfer function  $\zeta_{O_2}^{V'}$  and  $\zeta_{O_2}^{I'}$  were calculated:

$$\zeta_{O_2}^{V'}(j\omega) = \frac{\Delta I(j\omega)}{\Delta P_{O_2}(j\omega)} = \zeta_{O_2}^V(j\omega) + \beta \zeta_{H_2O}^V(j\omega) \quad (2.3)$$

$$\zeta_{O_2}^{I'}(j\omega) = \frac{\Delta I(j\omega)}{\Delta P_{O_2}(j\omega)} = \zeta_{O_2}^I(j\omega) + \beta \zeta_{H_2O}^I(j\omega) \quad (2.4)$$

The variable  $\beta = \Delta P_{H_2O} / \Delta P_{O_2}$  quantifies the fraction of the water transfer function that overlaps with the oxygen transfer function. The value of  $\beta$  depends on the specifications of the main flow and it is assumed to be constant over all frequencies [4].



## 2.5.2 Strategy to decouple concentration inputs contribution

As mentioned before, the simultaneous excitation of the system by water and oxygen partial pressures does not enable to measure the pure transfer functions, but only coupled ones. Consequently, the possibility of selectively detecting the dynamics related to gas and water transport in a PEMFC as predicted by theoretical studies of Sorrentino et al. [3] cannot be fully verified by mixed transfer functions.

One method that is proposed by Sorrentino et al. [4] to decouple the contributions of the two concentration inputs and to get the pure transfer functions is to measure two linearly independent sets of cFRA data for the system. Considering the cell at the certain steady-state condition and fixed specifications of the inlet flow rate, two cFRA experiments can be performed using different flow variations characterized by two different oxygen-water ratios,  $\beta'$ , and  $\beta''$ . This gives two coupled transfer functions that are linear combinations of the pure ones:

$$\zeta_{O_2}^{V(I)'}(j\omega) = \frac{\Delta I(V)'(j\omega)}{\Delta P_{O_2}'(j\omega)} = \zeta_{O_2}^{V(I)}(j\omega) + \beta' \zeta_{H_2O}^{V(I)}(j\omega) \quad (2.5)$$

$$\zeta_{O_2}^{V(I)''}(j\omega) = \frac{\Delta I(V)''(j\omega)}{\Delta P_{O_2}''(j\omega)} = \zeta_{O_2}^{V(I)}(j\omega) + \beta'' \zeta_{H_2O}^{V(I)}(j\omega) \quad (2.6)$$

The mathematical system constituted by equations (2.5) and (2.6) can be solved for each frequency and thus the pure oxygen and water transfer function ( $\zeta_{O_2}^{V(I)}$  and  $\zeta_{H_2O}^{V(I)}$ ) are obtained:

$$\zeta_{O_2}^{V(I)}(j\omega) = \left( \frac{\beta''}{\beta'' - \beta'} \right) \zeta_{O_2}^{V(I)'}(j\omega) + \left( \frac{-\beta'}{\beta'' - \beta'} \right) \zeta_{O_2}^{V(I)''}(j\omega) \quad (2.7)$$

$$\zeta_{H_2O}^{V(I)}(j\omega) = \left( \frac{-1}{\beta'' - \beta'} \right) \zeta_{O_2}^{V(I)'}(j\omega) + \left( \frac{1}{\beta'' - \beta'} \right) \zeta_{O_2}^{V(I)''}(j\omega) \quad (2.8)$$

The main criterion for applying this calculation scheme to experimental data is the linear independence of equations (2.5) and (2.6). In this thesis, the spectra of the pure cFRA transfer functions will be analysed.

## 3 Methodology

### 3.1 The Loewner framework for linear systems

In some applications, input-output measurements are useful because they replace an explicit model of a dynamic system. In such cases, it is crucial to construct state-space models and reduced state-space models effectively from the available data. The approach being discussed here is data-driven. It consists of collecting input/output measurements (e.g. frequency response measurements) for a suitable frequency range. The method known as the Loewner framework will be used to construct models that fit (or approximately fit) the data and have a reduced dimension. The idea is that, unlike current interpolatory methods, greater quantities of data are collected than required, and the basic underlying system structure is extracted. Therefore, a fundamental advantage of this method is that it can offer the user a trade-off between the accuracy of the fit and the complexity of the model. The Loewner framework was developed in several articles. For details refer to this literatures [5]–[8], [27].

#### 3.1.1 Development of the Loewner interpolation framework:

The transfer function of linear systems is a rational function. With the help of the rational functions, it can be explained that it is possible to compute models that fit (interpolate) to the given measurement data sets. In the context of linear dynamic systems, the starting point is provided by data sets consisting of the frequency response measurements.

In order to find the rational function that fits these measurements, attention is currently directed to the so-called Lagrange rational interpolation method, it uses a Lagrange basis for the numerator and denominator polynomials and builds rational interpolant (function) that fit original interpolation conditions. In ([28]), it was shown that this basis choice leads to numerically robust algorithms.

##### 3.1.1.1 Polynomial interpolation:

Let us begin with a classical problem of fundamental mathematics, the so-called polynomial interpolation problem (mentioned in [27]).

Given pairs  $S = \{(x_i, f_i) | x_i, f_i \in \mathbb{R}, i = \{1, 2, \dots, n + 1\}\}$  of nodes, i.e.  $x_i$ 's, and points, i.e.  $f_i$ 's, we are looking for an  $n$  degree polynomial with real coefficients that interpolates this given set of data. Thus, one has to calculate the polynomial coefficients  $c_k, k \in \{0, 1, \dots, n\}$  to satisfy the following  $n + 1$  interpolation conditions

$$p(x_i) = f_i, i \in \{1, 2, \dots, n + 1\} \text{ where } p(x) = \sum_{k=0}^n c_k x^k \quad (3.1)$$

This task turns out to be more or less straightforward; by writing the  $n + 1$  interpolation conditions in a matrix format, note that the following linear equation needs to be solved to recover the polynomial coefficients  $c_k, k \in \{0, 1, \dots, n\}$

$$\underbrace{\begin{bmatrix} 1 & x_1 & \cdots & x_1^n \\ 1 & x_2 & \cdots & x_2^n \\ \vdots & \vdots & \ddots & \vdots \\ 1 & x_{n+1} & \cdots & x_{n+1}^n \end{bmatrix}}_{\mathcal{V}} \underbrace{\begin{bmatrix} c_0 \\ c_1 \\ \vdots \\ c_n \end{bmatrix}}_c = \underbrace{\begin{bmatrix} f_1 \\ f_2 \\ \vdots \\ f_{n+1} \end{bmatrix}}_f$$

or in short  $\mathcal{V}c = f$  where  $\mathcal{V} \in \mathbb{R}^{(n+1) \times (n+1)}$  is a Vandermonde matrix (each of its rows contains the monomial basis  $\{1, x, \dots, x^n\}$  evaluated at one of the node  $x_i$  corresponding to the index of the row, i.e.,  $\mathcal{V}(\ell, h) = x_\ell^{h-1}, \forall \ell, h \in \{1, 2, \dots, n+1\}$ ). Then, obtain the vector of polynomial coefficients as  $c = \mathcal{V}^{-1}f$ .

Note that, one should usually avoid inverting a Vandermonde matrix since the condition number of such matrix increases exponentially, causing extreme ill-conditioning problems. Solving this linear system needs specialized algorithms that try to fix this issue.

An alternative way to solve the problem in (3.1) is to avoid the use of the monomial basis  $m_i(x) = x^i$  and thus inverting the Vandermonde matrix  $\mathcal{V}$ . Then, the so-called Lagrange polynomials  $\mathcal{L}_i(x)$  can be used to determine the same polynomial interpolant  $p$  as before. These polynomials are of degree  $n$  and they form a Lagrange basis

$$\begin{aligned} \mathcal{L}_1(x) &= (x - x_2)(x - x_3) \cdots (x - x_{n+1}) = \prod_{k=1, k \neq 1}^{n+1} (x - x_k) \\ \mathcal{L}_2(x) &= (x - x_1)(x - x_3) \cdots (x - x_{n+1}) = \prod_{k=1, k \neq 2}^{n+1} (x - x_k) \\ \mathcal{L}_{n+1}(x) &= (x - x_1)(x - x_2) \cdots (x - x_n) = \prod_{k=1, k \neq n+1}^{n+1} (x - x_k) \end{aligned}$$

Note that  $\mathcal{L}_i(x_k) = 0, \forall k \neq i, k, i \in \{1, 2, \dots, n+1\}$ . Based on this basis, directly construct a polynomial  $p$  that meets the requirements set out in (3.1)

$$p(x) = \sum_{i=1}^{n+1} \frac{f_i}{\underbrace{\mathcal{L}_i(x_i)}_{b_i}} \mathcal{L}_i(x) = \sum_{i=1}^{n+1} b_i \mathcal{L}_i(x) \quad (3.2)$$

Consider that the same polynomial  $p(x)$  can be written differently, either as  $\sum_{i=1}^{n+1} c_i m_i(x)$  or  $\sum_{i=1}^{n+1} b_i \mathcal{L}_i(x)$ , depending on the basis we work on. The reason for using the Lagrange basis instead of the monomial basis is that solving a large (in general) possibly ill-

conditioned linear system is avoided. In addition, the coefficients  $b_i = \frac{f_i}{\mathcal{L}_i(x_i)}$  are determined directly from a given data set  $\mathcal{D}$ .

Using the Lagrange polynomials, define the  $n$  degree polynomial

$$g(x) = \sum_{i=1}^{n+1} \frac{1}{\mathcal{L}_i(x_i)} \mathcal{L}_i(x) \quad (3.3)$$

Note that  $g(x_i) = 1 \forall i \in \{1, 2, \dots, n+1\}$  and let  $\hat{g}(x) = g(x) - 1$ . Therefore, the  $\hat{g}(x) = 0 \forall x \in \{x_1, x_2, \dots, x_{n+1}\}$ . Since  $\hat{g}(x)$  is a degree at most  $n$  polynomial with at least  $n+1$  roots, it follows that  $\hat{g}(x) = 0 \forall x \in \mathbb{R}$ . Then, conclude that  $g(x) = 1 \forall x \in \mathbb{R}$  and hence  $p(x) = \frac{p(x)}{g(x)} \forall x \in \mathbb{R}$ .

We derive the so-called barycentric formula by adding together (3.2) and (3.3):

$$p(x) = \frac{\sum_{i=1}^{n+1} \frac{f_i}{\mathcal{L}_i(x_i)} \mathcal{L}_i(x)}{\sum_{i=1}^{n+1} \frac{1}{\mathcal{L}_i(x_i)} \mathcal{L}_i(x)} \quad (3.4)$$

### 3.1.1.2 Rational interpolation:

In this section, the rational Lagrangian interpolation is discussed, which has proven to be a strong alternative to classic polynomial interpolation. For more information on this section, see [27], [28] and the references contained within.

A rational function  $r(x) = \frac{\mathcal{N}(x)}{\mathcal{D}(x)}$  is defined as the ratio between two polynomials, namely as the ratio between the numerator polynomial  $\mathcal{N}(x)$  and the denominator polynomial  $\mathcal{D}(x)$ . It is said that  $r$  is in the order  $n$  since  $\deg(\mathcal{N}) = \deg(\mathcal{D}) = n$  (and it is assumed that the two polynomials have no common roots). Generally, write

$$r(x) = \frac{\beta_n x^n + \beta_{n-1} x^{n-1} + \dots + \beta_1 x + \beta_0}{\alpha_n x^n + \alpha_{n-1} x^{n-1} + \dots + \alpha_1 x + \alpha_0} = \frac{\mathcal{N}(x)}{\mathcal{D}(x)}$$

Where  $\beta_k, \alpha_k \in \mathbb{R}, k \in \{0, 1 \dots n\}$  and  $\beta_k, \alpha_k \neq 0$ .

Consider that a rational function is usually more effective than a polynomial, because it has both poles (roots of the denominator) and zeros (roots of the numerator). Therefore, a rational function can model functions with singularities and strongly oscillating behaviour quite effectively than polynomials. Besides, rational functions have a strong theoretical importance because they represent a natural way for modelling linear dynamic systems in the frequency domain.

In the case of polynomial interpolation,  $n+1$  pairs of sampling nodes / points are required to recover a  $n^{\text{th}}$  degree polynomial  $p(x)$  (because a polynomial  $p(x)$  of degree  $n$  is represented by  $n+1$  coefficients  $c_k, k \in \{0, 1 \dots n\}$ ). Based on this consideration, it would be assumed that in order to recover a rational  $n^{\text{th}}$ -order function  $r(x)$ ,  $2(n+1)$  pairs of sampling

nodes / points are required (because  $r(x)$  is represented by  $2(n + 1)$  coefficients  $\alpha_k, \beta_k, k \in \{0, 1 \dots n\}$ ).

However, one degree of freedom is redundant because one of these coefficients can be set to 1. Dividing the numerator and the denominator by  $\alpha_n$ , get a new set of normalized coefficients  $\hat{\alpha} = \alpha_k/\alpha_n, \hat{\beta} = \beta_k/\alpha_n$  (hence  $\hat{\alpha} = \alpha_k/\alpha_n = 1$ ).

To be able to calculate a rational interpolant of order  $n$ , it is necessary to determine  $2n+1$  coefficients such that the following  $2n+1$  interpolation conditions are satisfied.

$$r(x_h) = f_h, h \in \{1, 2, \dots, 2n + 1\} \text{ Where } r(x) = \frac{\sum_{k=0}^n \hat{\beta}_k x^k}{\sum_{k=0}^n \hat{\alpha}_k x^k} \quad (3.5)$$

Therefore, the data set must include (at least)  $2n + 1$  pairs. Firstly, partition the set of interpolation nodes  $\{x_h | 1 \leq h \leq 2n + 1\}$  in two disjoint sets.

$$\{x_1, x_2, \dots, x_{2n+1}\} = \{\mu_1, \mu_2, \dots, \mu_n\} \cup \{\lambda_1, \lambda_2, \dots, \lambda_{n+1}\}$$

Secondly, partition the set of interpolation points  $\{f_h | 1 \leq h \leq 2n + 1\}$  in two disjoint sets (similar to nodes partitioning).

$$\{f_1, f_2, \dots, f_{2n+1}\} = \{v_1, v_2, \dots, v_n\} \cup \{w_1, w_2, \dots, w_{n+1}\}$$

Alternatively, use the Lagrangian basis instead of the monomial basis used in (3.5) and rewrite the rational interpolation problem using the barycentric formula in (3.4).

$$r(x_h) = f_h, h \in \{1, 2, \dots, 2n + 1\} \text{ Where } r(x) = \frac{\sum_{i=1}^{n+1} b_i \mathcal{L}_i(x)}{\sum_{i=1}^{n+1} a_i \mathcal{L}_i(x)} \quad (3.6)$$

Where the Lagrange polynomials are given  $\mathcal{L}_i(x) = \prod_{k=1, k \neq i}^{n+1} (x - \lambda_k), i \in \{1, 2, \dots, 2n + 1\}$ .

Therefore, one need to find the coefficients  $a_i$  and  $b_i$  to restore the function  $r(x)$ , so that  $r(\mu_j) = v_j, j \in \{1, 2, \dots, n\}$  and  $r(\lambda_i) = w_i, i \in \{1, 2, \dots, 2n + 1\}$ .

Since,  $\mathcal{L}_j(\lambda_i) = 0, \forall j \neq i$ , by evaluating  $r(x)$  as defined in (3.6) at the nodes  $\lambda_i$ , it follows that  $r(\lambda_i) = b_i/a_i \Rightarrow w_i = b_i/a_i \Rightarrow b_i = w_i a_i, \forall i \in \{1, 2, \dots, n + 1\}$ .

By dividing both of the numerator and denominator of  $r(x)$  from (3.6) with the polynomial  $\mathcal{L}(x) = \prod_{k=1}^{n+1} (x - \lambda_k)$ . The barycentric formula is then rewritten as

$$r(x) = \frac{\sum_{i=1}^{n+1} \frac{b_i}{x - \lambda_i}}{\sum_{i=1}^{n+1} \frac{a_i}{x - \lambda_i}} \quad (3.7)$$

Therefore, by selecting the numerator coefficients  $b_i$  to meet the condition  $b_i = w_i a_i$ , it turns out that the function  $r(x)$  automatically matches the values at the Lagrangian nodes  $\lambda_i$ , i.e., by construction. By eliminating the  $b_i$ 's, rewrite the formula in (3.7) as follows

$$r(x) = \frac{\sum_{i=1}^{n+1} \frac{w_i a_i}{x - \lambda_i}}{\sum_{i=1}^{n+1} \frac{a_i}{x - \lambda_i}} \quad (3.8)$$

### 3.1.1.3 The Loewner matrix

As mentioned in the previous section, the problem of rational interpolation was simplified to calculate the remaining  $n + 1$  denominator coefficients  $\{a_1, a_2, \dots, a_{n+1}\}$  such that  $r(\mu_j) = v_j$  for all  $j \in \{1, 2, \dots, n\}$ . By evaluating the function  $r(x)$  (as defined in (3.7)) at the remaining nodes  $\mu_j$ , we write

$$r(\mu_i) = v_j \Leftrightarrow \frac{\sum_{i=1}^{n+1} \frac{w_i a_i}{\mu_j - \lambda_i}}{\sum_{i=1}^{n+1} \frac{a_i}{\mu_j - \lambda_i}} = v_j, \forall 1 \leq j \leq n \Leftrightarrow \sum_{j=1}^n \sum_{i=1}^{n+1} \frac{v_j - w_i}{\mu_j - \lambda_i} a_i = 0 \Leftrightarrow \mathbb{L}a = 0,$$

where the Loewner matrix is defined as

$$\mathbb{L} = \begin{bmatrix} \frac{v_1 - w_1}{\mu_1 - \lambda_1} & \frac{v_1 - w_2}{\mu_1 - \lambda_2} & \dots & \frac{v_1 - w_{n+1}}{\mu_1 - \lambda_{n+1}} \\ \frac{v_2 - w_1}{\mu_2 - \lambda_1} & \frac{v_2 - w_2}{\mu_2 - \lambda_2} & \dots & \frac{v_2 - w_{n+1}}{\mu_2 - \lambda_{n+1}} \\ \vdots & \vdots & \ddots & \vdots \\ \frac{v_n - w_1}{\mu_n - \lambda_1} & \frac{v_n - w_2}{\mu_n - \lambda_2} & \dots & \frac{v_n - w_{n+1}}{\mu_n - \lambda_{n+1}} \end{bmatrix} \in \mathbb{R}^{n \times (n+1)}, \quad (3.9)$$

and the coefficients  $a_i$  are collected in the vector  $a = [a_1, a_2, \dots, a_{n+1}]^T$ . Therefore, one can effectively obtain the  $a_i$  coefficients by determining the null space of the Loewner matrix. The next step is then to calculate the  $b_i$  coefficients (using the relationship  $b_i = w_i a_i, \forall i \in \{1, 2, \dots, n + 1\}$ ). In this way, the rational function  $r(x)$  can be estimated uniquely [6], [27].

### 3.1.2 The Loewner pencil

Consider a full-order linear system defined by  $E \in \mathbb{R}^{n \times n}, A \in \mathbb{R}^{n \times n}, B \in \mathbb{R}^{n \times 1}, C \in \mathbb{R}^{1 \times n}$ , and its transfer function  $H(s) = C(sE - A)^{-1}B$ . Here the input / output data is provided, which is either measured or generated through numerical simulation. Given a set of input-output measurements specified by frequencies ( $\omega \in \mathbb{C}^n$ ) and corresponding responses ( $\mathcal{H} \in \mathbb{C}^n$ ). The aim is to find system matrices with lower order  $k$ , which are described by  $E_k \in \mathbb{R}^{k \times k}, A_k \in \mathbb{R}^{k \times k}, B_k \in \mathbb{R}^{k \times 1}, C_k \in \mathbb{R}^{1 \times k}$ , so that the resulting transfer function  $H_k(s) = C_k(sE_k - A_k)^{-1}B_k$  interpolates the given measurements.

The data can be organized into any two disjoint sets as follows:

$$\{(\omega_i, \mathcal{H}_i)\} = \{(\lambda_j, W_j)\} \cup \{(\mu_k, V_k)\},$$

Where  $j = 1, \dots, m$  and  $k = 1, \dots, n - m$ . For simplicity, take and define the partitioning

$$\begin{aligned} \lambda &= \omega(1:2:n), & W &= \mathcal{H}(1:2:n), \\ \mu &= \omega(2:2:n), & V &= \mathcal{H}(2:2:n), \end{aligned}$$

Then, the associated Loewner pencil, consists of the Loewner and shifted Loewner matrices (mentioned in [6], [27]). The Loewner matrix  $\mathbb{L}$  is defined as:

$$\mathbb{L} = \begin{bmatrix} \frac{v_1 - w_1}{\mu_1 - \lambda_1} & \dots & \frac{v_1 - w_k}{\mu_1 - \lambda_k} \\ \vdots & \ddots & \vdots \\ \frac{v_q - w_1}{\mu_q - \lambda_1} & \dots & \frac{v_q - w_k}{\mu_q - \lambda_k} \end{bmatrix} \quad (3.10)$$

And the shifted Loewner matrix  $\mathbb{L}_s$  is defined as:

$$\mathbb{L}_s = \begin{bmatrix} \frac{\mu_1 v_1 - \lambda_1 w_1}{\mu_1 - \lambda_1} & \dots & \frac{\mu_1 v_1 - \lambda_k w_k}{\mu_1 - \lambda_k} \\ \vdots & \ddots & \vdots \\ \frac{\mu_q v_q - \lambda_1 w_1}{\mu_q - \lambda_1} & \dots & \frac{\mu_q v_q - \lambda_k w_k}{\mu_q - \lambda_k} \end{bmatrix} \quad (3.11)$$

### 3.1.3 Construction of reduced order models

Two cases are differentiated here, namely, the right amount of data and the more practical redundant amount of data. For more details on this section, (see in [5], [6], [27]).

#### 3.1.3.1 The first case

Assume that  $(\mathbb{L}_s, \mathbb{L})$ , be a regular pencil, so that none of the interpolation points  $\lambda_i, \mu_j$  are its eigenvalues. Then  $E = -\mathbb{L}, A = -\mathbb{L}_s, B = V, C = W$ , is a minimal realization of an interpolant of the data, i.e., the rational function  $H(s) = W(\mathbb{L}_s - s\mathbb{L})^{-1}V$ , interpolates the data.

#### 3.1.3.2 The second case

If the pencil  $(\mathbb{L}_s, \mathbb{L})$  is singular, it is the case of redundant data. In this case, the following assumption is made.

$$\text{rank}(x\mathbb{L} - \mathbb{L}_s) = \text{rank} \begin{bmatrix} \mathbb{L} \\ \mathbb{L}_s \end{bmatrix} = \text{rank}[\mathbb{L} \quad \mathbb{L}_s] = k \leq n, \quad (3.12)$$

for all  $x \in \{\lambda_i\} \cup \{\mu_j\}$ , we consider the following SVD factorizations:

$$[\mathbb{L} \quad \mathbb{L}_s] = Y_1 S_1 X_1^T, \quad \begin{bmatrix} \mathbb{L} \\ \mathbb{L}_s \end{bmatrix} = Y_2 S_2 X_2^T, \quad (3.13)$$

where  $Y_1, X_2 \in \mathbb{C}^{n \times n}$ . By selecting the first  $k$  columns of the matrices  $Y_1$  and  $X_2$ , one can get projection matrices  $Y, X \in \mathbb{C}^{n \times k}$ . The following result is used in practical applications.

A realization  $(E_k, A_k, B_k, C_k)$  of an approximate interpolant is given by the system matrices

$$E_k = -Y_k^* \mathbb{L} X_k, \quad A_k = -Y_k^* \mathbb{L}_s X_k, \quad B_k = Y_k^* V, \quad C_k = W^T X_k \quad (3.14)$$

Hence, the rational function  $H(s) = WX(Y^T \mathbb{L}_s X - sY^T \mathbb{L} X)^{-1} Y^T V$  approximately matches the data. So if there is more data than required, one can consider  $(\mathbb{L}_s, \mathbb{L}, V, W)$  as a singular model of the data. A suitable projection then leads to a reduced system of order  $k$ . A significant outcome is that the Loewner framework provides a compromise between accuracy and complexity of the reduced-order system using the singular values of  $\mathbb{L}$ .

### 3.2 Algorithm

This section is discussed the systematic approach in terms of algorithms that can be used for analysing EIS and cFRA experimental data. All algorithms described in this section are implemented in the MATLAB environment.

---

#### Algorithm 1: Calculation of Transfer function (in frequency domain) from time domain data/signals

---

**Input:** Experimentally measured data sets in the time domain. Each data set consists of the perturbation of the input (oxygen and/or water partial pressure) at different frequencies and the corresponding output response (electrical potential or current) as signals.

**Output:** Transfer functions (frequency response measurements).

---

1. Apply Fast Fourier Transform (FFT) to the inputs and output signals for 1<sup>st</sup> data set (see section 8.1.2 in the Appendix).
  2. Calculate frequency domain by using length of the signal and sampling frequency for all signals (as described in section 8.1.3 in the Appendix).
  3. Calculate amplitude spectrum from FFT spectrum for all (see section 8.1.3.1 in the Appendix).
  4. Collect the dominant harmonics and the corresponding FFT spectrum of input and output.
  5. Calculate the spectrum ratio (transfer function) between output and input (as mentioned in eqs. (2.1) and (2.2)) at the frequency of collected harmonics.
  6. Repeat above steps for all the data sets.
- 

After obtaining frequency response measurements at frequencies of interest, an appropriate state-space model is determined for further analysis. In order to construct a descriptor-state-space model that interpolates these frequency response measurements, here the Loewner framework has been employed.

---

#### Algorithm 2: Loewner framework for constructing state-space models and reduced state-space models

---

**Input:** The vector  $\omega \in \mathbb{C}^N$  contains  $N$  points on the  $j\omega$  axis,  $\omega(i) \in [0, \infty)$ , and the entries of  $H \in \mathbb{C}^N$  are frequency response measurements computed as

---



$$H(i) = C(\omega(i)E - A)^{-1}B$$

for an unknown system  $E, A \in \mathbb{R}^{n \times n}, B \in \mathbb{R}^{n \times 1}, C \in \mathbb{R}^{1 \times n}$ , of unknown order  $n$ .

**Output:** To construct a reduced model of order  $k$ , given by  $E_k, A_k \in \mathbb{R}^{k \times k}, B_k \in \mathbb{R}^{k \times 1}, C_k \in \mathbb{R}^{1 \times k}$ , that interpolates the given measurements

$$H_k(\omega(i)) = H(i)$$

$$\text{With } H_k(s) = C_k(sE_k - A_k)^{-1}B_k.$$

1. Partition the given measurements into any two disjoint sets

$$\{(\omega_i, H_i)\} = \{(\lambda_j, W_j)\} \cup \{(\mu_k, V_k)\},$$

For  $j = 1, \dots, M$  and  $k = 1, \dots, N - M$ . for simplicity, take  $M = N/2$ , and define the partitioning

$$\begin{aligned} \lambda &= \omega(1:2:n), & W &= H(1:2:n), \\ \mu &= \omega(2:2:n), & V &= H(2:2:n), \end{aligned}$$

2. Next, to ensure that our reduced models are real, i.e. matrices  $E_k, A_k, B_k, C_k$  have real entries, we also need to use the complex conjugate values of the measurements. Thus, define vectors

$$\begin{aligned} \lambda &\leftarrow [\lambda_1, \bar{\lambda}_1, \lambda_2, \bar{\lambda}_2, \dots], & W &\leftarrow [W_1, \bar{W}_1, W_2, \bar{W}_2, \dots], \\ \mu &\leftarrow [\mu_1, \bar{\mu}_1, \mu_2, \bar{\mu}_2, \dots], & V &\leftarrow [V_1, \bar{V}_1, V_2, \bar{V}_2, \dots], \end{aligned}$$

From these measurements, form the Loewner matrix  $\mathbb{L}$  and shifted-Loewner matrix  $\mathbb{L}_s$  defined as

$$\mathbb{L}(i, j) = \frac{V_i - W_j}{\mu_i - \lambda_j}, \quad \mathbb{L}_s(i, j) = \frac{\mu_i V_i - \lambda_j W_j}{\mu_i - \lambda_j}.$$

Notice that the Loewner matrices still have complex entries.

3. To obtain matrices with real entries, apply the following transformation

$$\mathbb{L} \leftarrow P^* \mathbb{L} P, \quad \mathbb{L}_s \leftarrow P^* \mathbb{L}_s P, \quad W \leftarrow (W^T P)^T, \quad V \leftarrow P^* V,$$

Where  $P$  is a block-diagonal matrix, with each diagonal block given by the matrix

$$\frac{1}{\sqrt{2}} \begin{bmatrix} 1 & j \\ 1 & -j \end{bmatrix}.$$

4. Then, the order  $k$  of the reduced order interpolant  $H_k$  is given by the rank of  $\mathbb{L}$ . Let  $\mathbb{L} = Y S X^*$  be the singular value decomposition (SVD) of the Loewner matrix  $\mathbb{L}$ . Define

$$\begin{aligned} Y_k &= Y(:, 1:k), \\ X_k &= X(:, 1:k), \end{aligned}$$

Note that, here, the projection matrices are chosen differently than in (3.13), by employing only one SVD, i.e., of the Loewner matrix  $\mathbb{L}$ .

5. Then the reduced order model  $H_k$  is given by

$$E_k = -Y_k^* \mathbb{L} X_k, \quad A_k = -Y_k^* \mathbb{L}_s X_k, \quad B_k = Y_k^* V, \quad C_k = W^T X_k.$$

Now, we have a state-space model (where  $E_k, A_k, B_k, C_k$  are the system matrices). In order to determine poles and residuals of the system, one needs to perform a partial fraction expansion of the associated transfer function, for details refer to [29], [30].

---

**Algorithm 3: Partial fraction expansion of the associated transfer function**

---

**Input:** System  $[E_k, A_k \in R^{k \times k}, B_k \in R^{k \times 1}, C_k \in R^{1 \times k}]$  with transfer function  $H_k(s) = C_k(sE_k - A_k)^{-1}B_k$ , where  $s = j\omega$ .

**Output:** Residues ( $R_i$ ) and Poles ( $\lambda_i$ )

---

1. The eigenvalue decomposition (EVD) of the matrix pencil  $(A_k, E_k)$ , or equivalently of  $E_k^{-1}A_k$ ; let

$$E_k^{-1}A_k = V_k \Lambda_k V_k^{-1},$$

Where the columns of  $V_k = [v_1, \dots, v_k]$  are the eigenvectors,  $\Lambda_k = \text{diag}[\lambda_1, \dots, \lambda_k]$  are the eigenvalues of the reduced system (poles of  $H_k(s)$ ), and  $[\tilde{v}_1; \dots; \tilde{v}_k]$  are the rows of  $V_k^{-1}$ .

2. Residues of  $H_k(s)$

$$R_i = [C_k v_i][\tilde{v}_i(E_k^{-1}B_k)],$$

Where  $i = 1 : k$ .

3. The new representation of Transfer function can be represented as:

$$H(s) = \sum_{i=1}^k \frac{R_i}{s - \lambda_i} \quad (3.15)$$


---

Since the aim is to understand and decouple the various dynamics of a complex system (here a PEMFC), it becomes important to identify the gains and time constants that are related to the different phenomena of the system from the poles and the residues. Alternatively, the transfer function can be expressed in terms of gains ( $G$ ) and time constants ( $\tau$ ), as shown in eq. (3.16).

$$H(s) = \sum_{i=1}^k \frac{G_i}{1 + \tau_i s} \quad (3.16)$$

By comparing these two equations ((3.15) and (3.16)) one can get,

$$G_i = -\frac{R_i}{\lambda_i}$$

And

$$\tau_i = -\frac{1}{\lambda_i}$$

Since residues ( $R_i$ ) and poles ( $\lambda_i$ ) have a complex values, the absolute values of Gains ( $G_i$ ) and time constants ( $\tau_i$ ) will be used for the later representation.

Here, pole ( $\lambda_i$ ) =  $\sigma_i + j\omega_i$  where  $\sigma_i$  is the decay (or growth) rate and  $\omega_i$  is the frequency of the  $i^{th}$  oscillation. Thus, one can also get the time constant from the real part of the pole ( $\tau_i = \left| \frac{1}{\sigma_i} \right|$ ). Besides, the characteristic (or break point) angular frequency  $\omega_c = \sqrt{\sigma^2 + \omega^2}$  or  $\omega_c = |\lambda|$ . So, the time constant  $\tau = \frac{1}{\omega_c}$ .

### 3.3 Method validation with simple RLC circuit

In this section, the novel approach to obtain gain and time-constant distribution of the system from its state-space model is validated by means of a simple RLC circuit.

Consider a simple RLC circuit containing four different resistors ( $R_1=200 \Omega$ ,  $R_2=100 \Omega$ ,  $R_3=50 \Omega$ ,  $R_0=70 \Omega$ ), two capacitors ( $C_1=2.5 \times 10^{-3} \text{ F}$ ,  $C_2=10^{-4} \text{ F}$ ) and one inductor ( $L_1=3 \times 10^2 \text{ H}$ ) as shown in Figure 3.1. Moreover, time constants for this specific RLC circuit are  $\tau_1 = R_1 \times C_1 = 0.5 \text{ s}$ ,  $\tau_2=R_2 \times C_2 = 0.01 \text{ s}$  and  $\tau_3=L_1/R_3 = 6 \text{ s}$ .

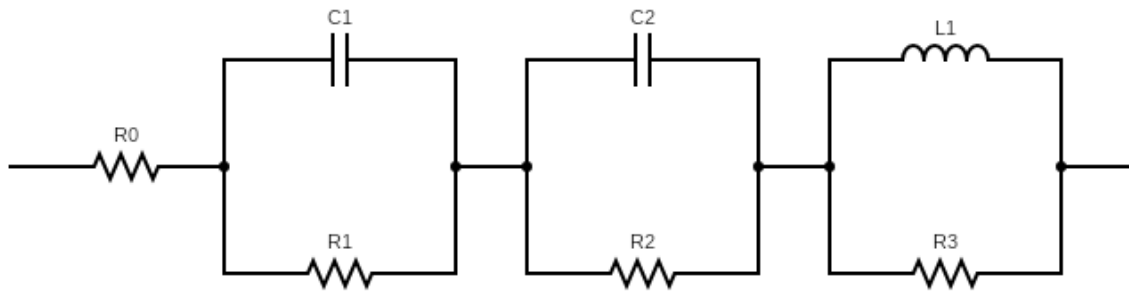


Figure 3.1: RLC circuit

The circuit is excited at a certain steady state by a periodic electrical current as input between frequency range 0.01 Hz and 100 Hz. The resulting voltage response is calculated in MATLAB environment. After applying FFT to the input and output signals, a transfer function is determined. The Bode and Nyquist plots of the RLC circuit are shown in the Figure 3.2 (a-b). The plot in Figure 3.2 (c) shows the decay of the singular values of the Loewner matrix. This representation is a very useful way to specify the order of the model  $k$  (by observing the decay of the singular values) so that one can make a trade-off between model accuracy and complexity. Note that, by truncating at the order  $k = 4$ , one can achieve an accuracy of about  $10^{-11}$ . The response is well approximated by a reduced state-space model of order 4 as shown in Figure 3.2 (d).

In addition, to verify the accuracy of the fitted model with the measured or simulated spectra, the corresponding deviation of the fitted model  $H_k$  from the measured spectra is calculated as relative residuals with equations (3.17) and (3.18), and the corresponding relative residuals are plotted in Figure 3.2 (e), which is below 1 % for the whole frequency range. Thus, further analysis is justified [20], [31].

$$\Delta_{Re}(j\omega) = \frac{Z_{Re}(j\omega) - H_{Re}(j\omega)}{|Z(j\omega)|} \times 100\% \quad (3.17)$$

$$\Delta_{Im}(j\omega) = \frac{Z_{Im}(j\omega) - H_{Im}(j\omega)}{|Z(j\omega)|} \times 100\% \quad (3.18)$$

Where  $|Z(j\omega)|$  refers to the absolute value of the measured or simulated impedance and  $H(j\omega)$  represents the model impedance.

Applying methodology as describe in section 3.2 the gain and time constant distribution of this RLC circuit is calculated. The obtained time constant spectrum is shown in Figure 3.2 (f). In this figure, amplitude of peaks (y-axis values) corresponds to the resistances chosen, and the locations of the peaks (x-axis values) are the associated time constants, i.e.  $\tau = R \times C$ . Moreover, the magnitude of peak at very low time constant corresponds to total resistance of circuit, which is detected at the high frequency region of the spectra. Real part of gains is plotted on right y-axis of the same plot, positive values of it indicate capacitive behaviour and negative values indicate inductive behaviour.

This is a well-known system, and it was used as a test. We knew which time constants should have been expected, and we verified if the Loewner framework would have been detected the same. In the next chapter, the case of a complex system (here PEMFC) where multiple phenomena occur with closer time constants is discussed. Notice that for later analysis of EIS and cFRA spectra in this work, the distribution of the characteristics frequency (DCF) is preferred over the time constant spectra, since  $f_c = \frac{1}{2 \times \pi \times \tau}$  is valid.

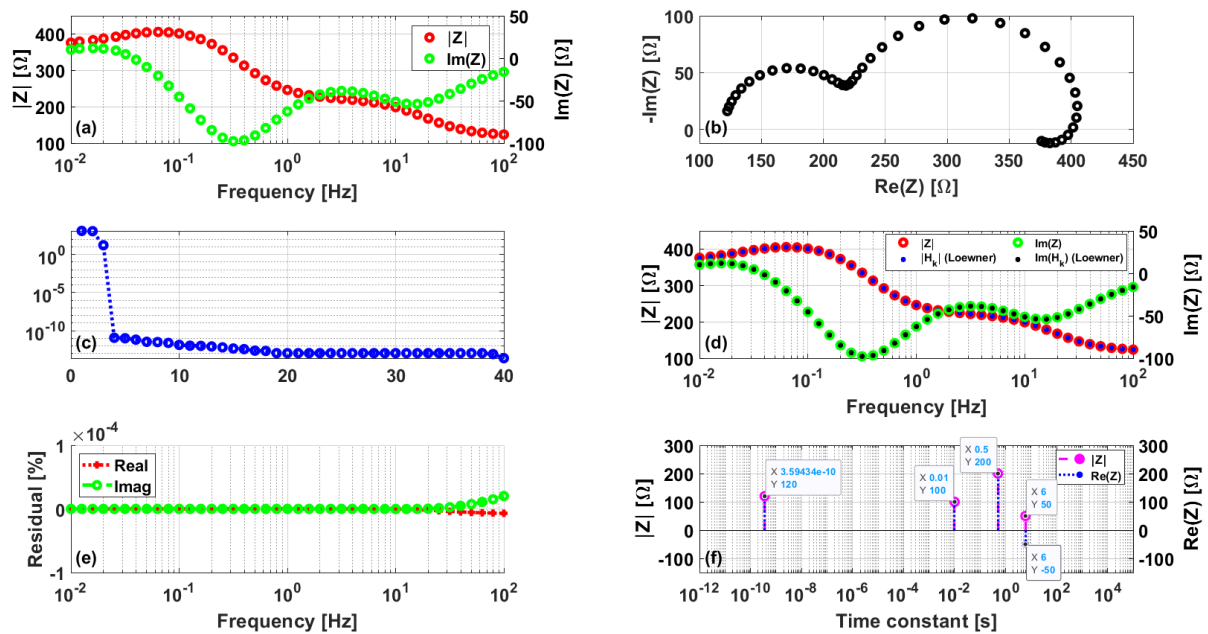


Figure 3.2: (a) Bode plot of RLC circuit, (b) Nyquist plot of RLC circuit, (c) Singular value decay of the Loewner matrix, (d) Frequency response comparison – state space model, (e) Model residuals, (f) Corresponding time constant spectrum.

## 4 EIS

### 4.1 Analysis of impedance spectra of PEMFC

In this section, EIS data of a PEMFC are analysed across a wide range of frequencies by the novel method. The spectra are recorded in a frequency range from 0.01 Hz to 1 kHz at five measurement points per decade. Figure 4.1(a-b) shows an example of a typical PEMFC impedance spectrum (cell operated at  $T=80\text{ }^{\circ}\text{C}$ , 55% R.H. ( $\text{H}_2/\text{air}$ ) and  $j=300\text{ mA cm}^{-2}$ ). In this case, normal operating conditions are applied over the whole cell area (see section 8.2.1 in the Appendix).

The Nyquist plot (Figure 4.1 (b)) directly illustrates Ohmic losses,  $R_0$ , and polarization losses,  $R_p$ .  $R_0$  is specified as the high frequency intercept ( $\omega \rightarrow \infty$ ) with the real axis, while  $R_p$  as the subtraction of low frequency ( $\omega \rightarrow 0$ ) and high frequency intercept ( $\omega \rightarrow \infty$ ) with the real axis. Besides,  $R_0$  can decompose into ionic and electronic resistance. The electronic resistance due to electrons transport in electrodes, gas diffusion layers (GDL), and flow fields, whereas the proton transport process in the polymer electrolyte membrane causes the ionic resistance. Since the electronic conductivity is significantly higher than the ionic conductivity, thus the main contribution to the Ohmic losses is because of the membrane conductivity [20].

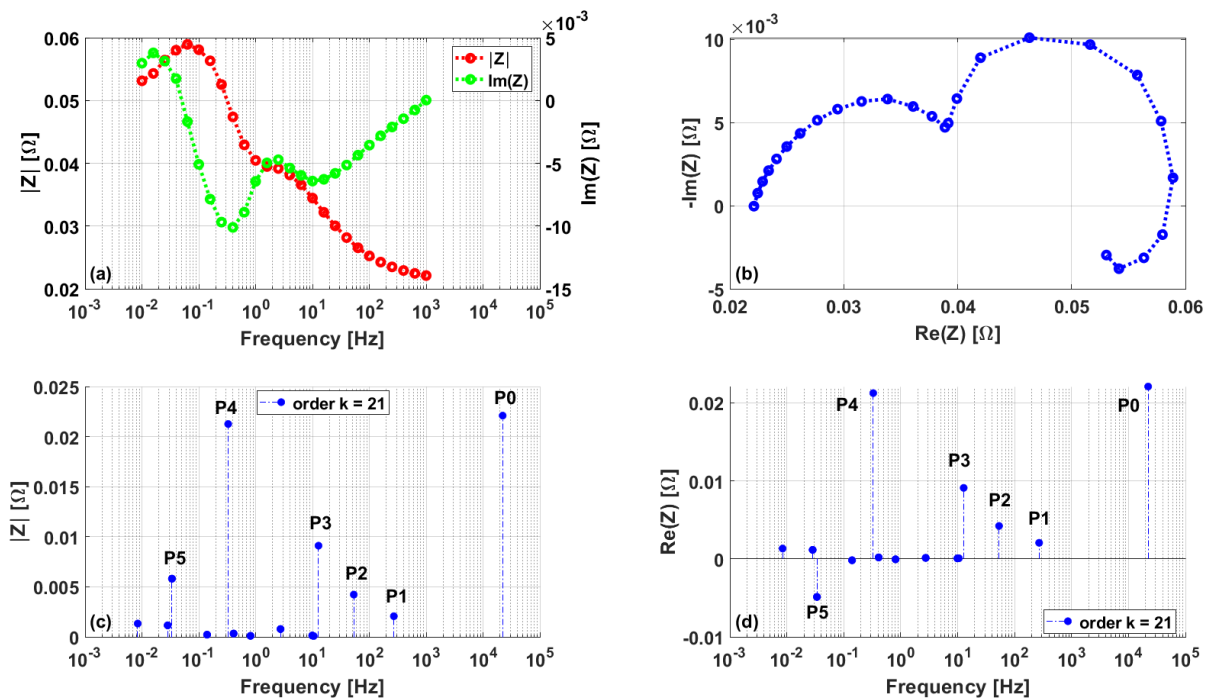


**Figure 4.1: Impedance spectra of PEMFC operated with Air and  $T = 80\text{ }^{\circ}\text{C}$ ,  $\text{RH}=33\%$  and  $j=300\text{ mA cm}^{-2}$ . (a) Bode plot, (b) Nyquist plot, (c) The DCF spectra, and (d) Real part of the DCF spectra.**

See, Figure 4.1 (c-d) for a detailed view of the polarization processes, which shows the distribution of the characteristic frequency (DCF) spectra corresponding to the impedance spectra. The DCF spectra allow the de-convolution of up to six separable peaks (P0-P5) with different characteristic frequencies (22.1 kHz, 270 Hz, 53 Hz, 13 Hz, 0.33 Hz, 0.034 Hz). Each peak (from P1-P5) that characteristic frequencies are related to time constants of different polarization processes and the peak (P0) at a very high frequency indicates an Ohmic resistance ( $R_0$ ). Whereas in the Bode plot (magnitude spectra and imaginary part spectra), only three dynamics are visible. Correspondingly, only three clear loops (representing different phenomena) are seen in the Nyquist plot.

Besides the characteristic frequency, the associated resistance of each process is illustrated by the magnitude (y-axis value) of the peak. As can easily be noticed, this new approach facilitates a better separation and identification of the individual dynamics and allows to evaluate the resistances related to different physical processes. Here the total resistance ( $R_T = 0.0530 \Omega$ ) is the sum of the real part value of all the gains (peak values). So one can also calculate the polarization resistance ( $R_P = 0.0309 \Omega$ ) by subtracting the Ohmic (membrane) resistance ( $R_0 = 0.0221 \Omega$ ) from the total resistance. These resistances can also confirm by examination of the Nyquist Plot.

However, the number and location of the visible peaks depend strongly on the order of the state-space model  $k$ . Hence, the selection of  $k$  must be carefully pre-evaluated to obtain a meaningful distribution of gains (polarization contributions) with different characteristic frequencies (time constants) for the provided impedance data. In Figure 4.2 (a1-a4) the distribution of the characteristic frequency (DCF) spectra are determined for different values of order  $k$ , starting from 17 to 23 (note that one can select maximum order  $k$  up to the rank of Loewner matrix, here 26).

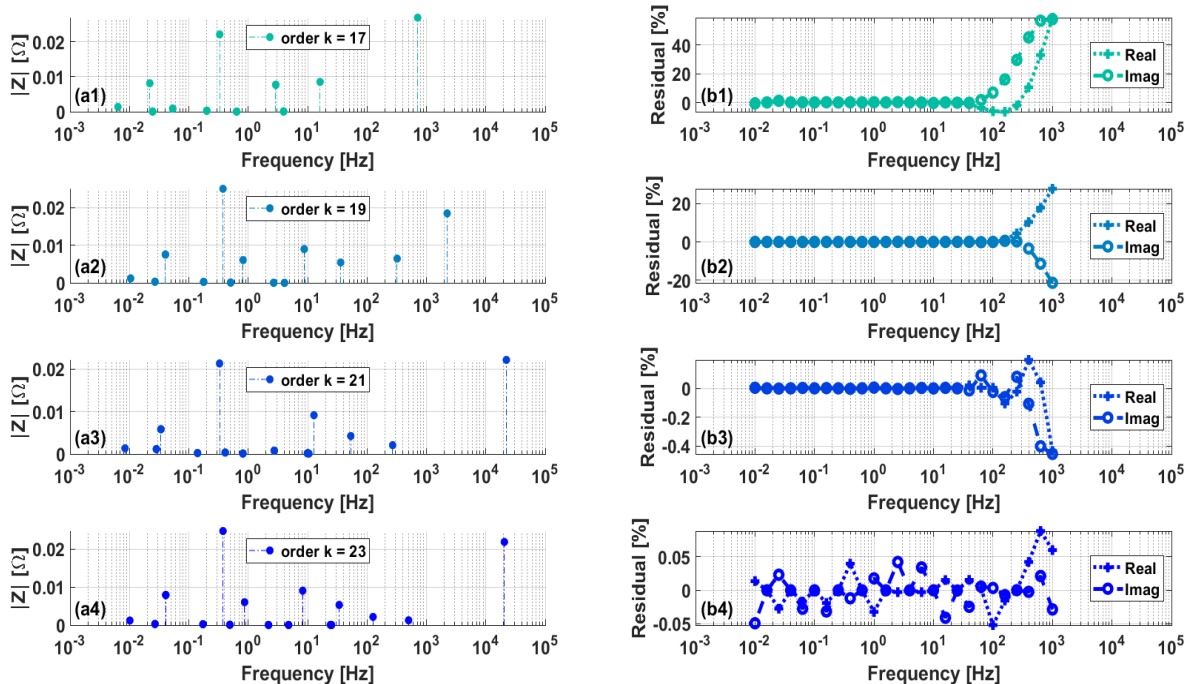
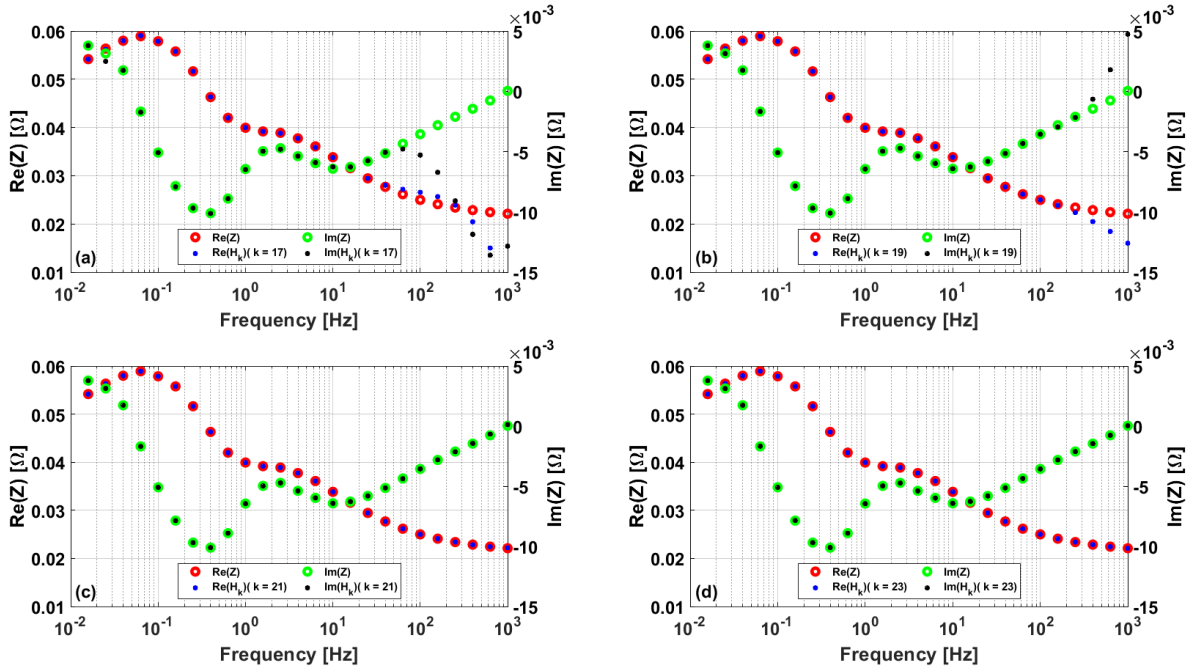


Figure 4.2: (a1-a4) The DCF spectra for different values of order  $k$ , (b1-b4) respective residual.

It can be noticed that different values of  $k$  lead to a varying number of peaks (as well as the magnitude and location of the peaks). For an ideal spectrum,  $k$  can be set to any large value to decompose all phenomena. However, for a measured spectrum too large values of  $k$  lead to erroneous results due to the noise superimposed on the measurement, which can lead to physical misinterpretations. This problem may arise at values of  $k=23$  (see Figure 4.2 (a4)). On the other hand, lower values of  $k$  (17, 19) cannot reproduce the measured spectrum over the whole frequency range (see Figure 4.3 (a-b)).



**Figure 4.3: Frequency response comparisons with the state space model of different model order  $k$  (a-d).**

For verifying the accuracy of the fitted model to the measured spectrum, the respective error of the model is determined in terms of relative residuals (Figure 4.2 (b1-b4)) by using equations (3.17) and (3.18). It is obvious that the residuals decrease with higher values of  $k$ , but do not become better for  $k$  values above 21 (see Figure 4.2 and Figure 4.3). Thus, in this case,  $k$  was chosen to 21 for the analysis of the DCF spectra, in order to achieve a trade-off between low residuals and possible avoidance of noise. In the next few sections, the experimental parameters are varied such that it becomes easier to understand dynamics related to each of the peaks and allocate them to the different physicochemical phenomena that take place in the PEMFC.

## 4.2 Allocating the distribution of characteristic frequency peaks

The impedance spectrum obtained during a PEMFC operation in  $H_2$ /air flows ( $T = 80\text{ }^\circ\text{C}$ ,  $F_{H_2} = 850\text{ ml/min}$ ,  $F_{air} = 600\text{ ml/min}$ ,  $j = 300\text{ mA cm}^{-2}$ ,  $RH = 33\%$  for both inputs) is presented in Figure 4.4 (a-c). As mentioned previously, the impedance spectrum shows only three main characteristics or visible arcs at high (5 - 1 kHz), medium (0.1 - 5 Hz) and low frequencies ( $< 0.1\text{ Hz}$ ). Figure 4.4 (d) displays the relative residuals of the respective fitted state-space model to the measured data. The residuals are less than 0.5% for the entire frequency range. Thus, relatively small residuals confirm reproducibility and allow further processing.

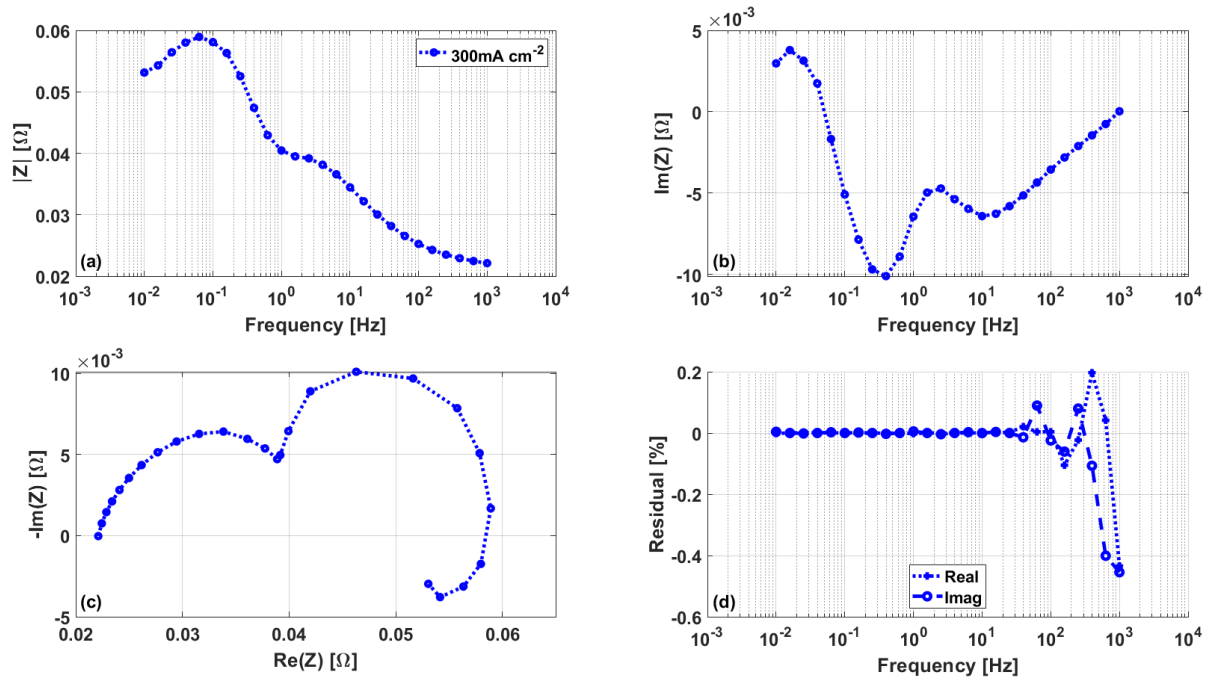


Figure 4.4: Impedance spectra of PEMFC operated with Air and  $T = 80^{\circ}\text{C}$ ,  $\text{RH}=33\%$  and  $j=300\text{ mA cm}^{-2}$ . (a) Magnitude spectra, (b) Imaginary part of spectra, (c) Nyquist plot, and (d) Relative residuals.

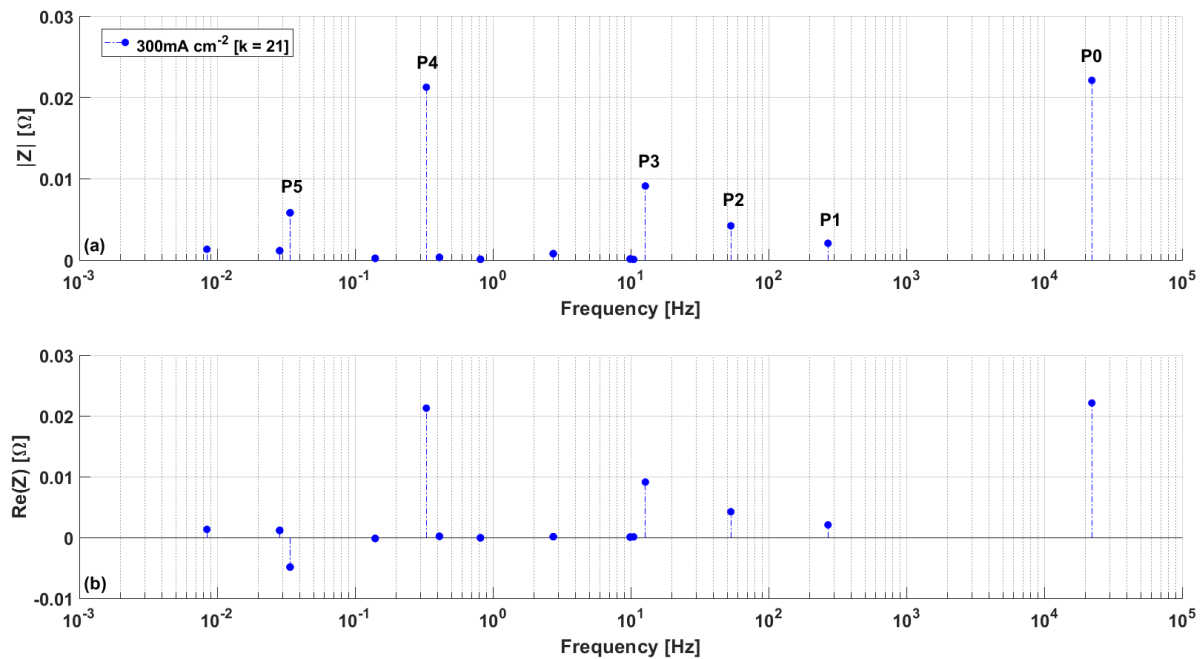


Figure 4.5: (a) The DCF spectra correspond to Impedance spectra in Figure 4.4, (b) Real part of the DCF spectra.

The DCF spectrum resulting from the analysis of the EIS data is illustrated in Figure 4.5 (a-b). It is obvious that this approach identifies six different peaks: One peak at very high frequency ( $P_0 > 10\text{ kHz}$ ), three different contributions in the high-frequency range ( $P_1 - P_3$ ), followed by one in mid-frequency ( $P_4$ ) and another peak in the low-frequency region ( $P_5$ ).



Note that there are also very small but distinct peaks in the mid to low frequency range. However, these peaks are not assigned because their contribution is very small and, at present, it cannot be evaluated if they are due to some physical phenomena or noise.

Then, the main advantage of this methodology of analysis of the FRA spectra is the decoupling of several different dynamics with similar time constants, which is not possible with the conventional representation in the form of Bode and Nyquist plots. In this way, the impedance values related to different physical processes are easily and directly determined.

The contribution of the Ohmic resistance  $R_0$  is found at the high-frequency end of the impedance spectrum ( $>10^4$  Hz) [15], [32]. This Ohmic resistance mainly corresponds to the ionic resistance of the polymer electrolyte membrane [20].

The kinetics of the charge transfer reactions occurring simultaneously with the double-layer charging is in the high-frequency range of 100 Hz [3], [32]. There are two charge transfer resistances as a consequence of the kinetic hindrance of the electrode reactions, which are the hydrogen oxidation reaction (HOR) and the oxygen reduction reaction (ORR). The contribution to the kinetic activation losses of the HOR is usually significantly lower than the one of the ORR [33]. Hence, it is feasible to hypothesize that P1 and P2 are correlated to the dynamics of HOR and ORR, respectively.

The oxygen diffusion to the electrode through the GDL is usually founded with a characteristic frequency around 10 Hz. Thus, phenomena with identical characteristic frequency could describe the mass transport resistance of GDL [13]. In the experimental work of Weiss et al. [21], two phenomena that occur at around 10 Hz and 50 Hz, respectively, are successfully assigned to oxygen reduction reaction-related processes. Thus, one can also hypothesize that peak P2 and P3 are related to the dynamics of ORR. So, one cannot allocate P3 to only one of the both processes (ORR and oxygen mass transport in the GDL) in the case of a fuel cell operated with air. Due to the overlap of the phenomena (P1-P3) in the impedance spectra, only one curve is appeared in the Bode and Nyquist plots (see Figure 4.4 (a-c)).

At a frequency around 0.7 Hz, the dynamics with respect to the oxygen mass transport in the channel on the cathode side are observed. This mass transport effect is explained by the decrease in oxygen concentration along the cathode flow channel [3], [34].

At low humidification, the dehydration phenomenon due to an electro-osmotic drag is observed with a characteristic frequency of around 0.1 Hz [32]. The strength of the electro-osmotic effect depends strongly on the current. Thus, the flux of water from the dry anode to the wetter cathode is enhanced as the current increases. Consequently, the water content of the membrane drops near the anode, the membrane becomes locally dehydrated, and the Ohmic resistance increase [35]. This effect has similar time constants as the mass transport phenomena in the channel and appears in the Nyquist diagram as a second loop. Therefore, these two effects often overlap in the impedance spectra, so that an exact differentiation is not possible. Due to this fact, one cannot assign the peak P4 individually to one of these both processes.

Finally, the back diffusion of water from the cathode to the anode via the membrane is observed at a low characteristic frequency around 0.01 Hz [3], [32], [36]. In contrast to the other phenomena, however, this causes a reduction in impedance. The increased current generates additional water at the cathode, which needs a certain time to diffuse through the membrane from cathode to anode. The increased water content reduces the membrane's proton resistance, especially in locally very dry regions [35]. In the Nyquist plot (Figure 4.4 (c)) this phenomenon appears as an inverted loop. The negative value of gain (resistance) at a frequency of about 0.03 Hz in the DCF spectra (Figure 4.5 (b)) confirms that this phenomenon has occurred. Thus, one can certainly assign the peak P5 to the dynamics of water transport in the membrane by back diffusion. This phenomenon is more pronounced in dry operating conditions (low relative humidity) [37].

After the phenomenon of back diffusion (P5) the total resistance  $R_T$  can be obtained by a very low-frequency intercept ( $\sim 10^{-3}$  Hz) of the real axis in the Nyquist diagram (see Figure 4.4 (c)). This total resistance is also determined by summing the real part of the gain over the whole frequency range in DCF spectra (see Figure 4.5 (b)). Thus, the polarization resistance  $R_p$  is the difference between  $R_T$  and  $R_o$  [20]. This polarization resistance is the resistance or slope of the polarization curve at the operating point where the EIS measurement is performed.

Furthermore, note that the explanation of the impedance spectra and the assignment of the peaks in the DCF spectrum to the various physicochemical phenomena are based only on a general understanding of the EIS and the literature review of the related research in this field. For this reason, the interpretation becomes relatively clear. However, verification is still required by performing further experiments at different operating conditions.

### 4.3 Variation of the operating conditions

In this section, the operating conditions of the experiments are changed systematically in order to monitor the variation of the individual peaks and identify the specific phenomenon related to them. To eliminate mass transport losses in GDL and channel, the PEMFC is operated with pure oxygen rather than air (all other parameters are unchanged). Moreover, in order to identify the losses associated with water transport in the membrane, the cell is operated with an increased relative humidity of the feeds.

As shown in the Bode and Nyquist plots, the overall impedance decreased when pure oxygen is used as cathode feed instead of air. Especially the middle and the beginning of the high-frequency part of the impedance spectrum (0.1 to  $\sim 30$  Hz) reduced (compare blue and black lines in Figure 4.6 (a, c)).

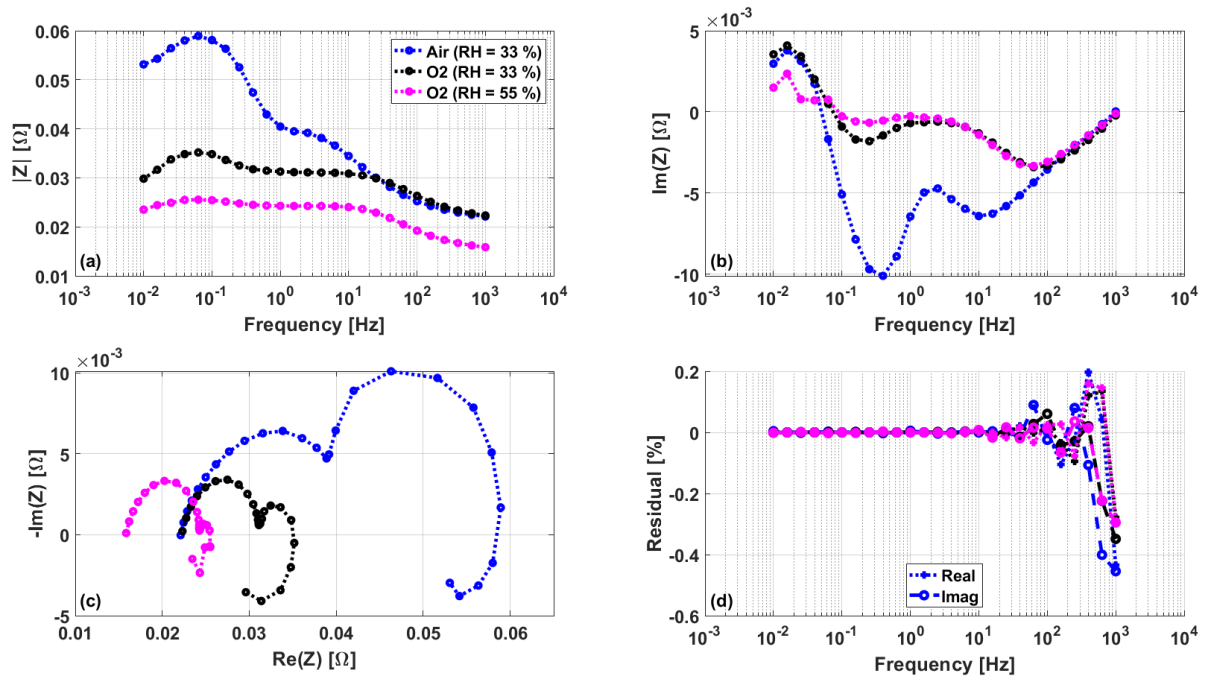


**Figure 4.6: (a) Magnitude spectra, (b) Imaginary part of spectra, (c) Nyquist plot, and (d) Relative residuals. Impedance spectra of PEMFC operated with air and  $T = 80^\circ\text{C}$ ,  $\text{RH} = 33\%$ , and  $j=300 \text{ mA cm}^{-2}$  are shown as blue data; impedance spectra of PEMFC operated with pure O<sub>2</sub> and  $T = 80^\circ\text{C}$ ,  $\text{RH} = 33\%$ , and  $j=300 \text{ mA cm}^{-2}$  are displayed as black data; impedance spectra of PEMFCs operated at pure O<sub>2</sub> and  $T = 80^\circ\text{C}$ ,  $\text{RH} = 55\%$ , and  $j=300 \text{ mA cm}^{-2}$  are represented as pink data.**

In addition, the membrane resistance (high-frequency intercept of the real axis in the Nyquist plot) dropped significantly as the humidification of pure oxygen and H<sub>2</sub> increased from 33% to 55%. The mid to low frequency part of the spectra (0.01 to 1 Hz) is also significantly influenced (see black and pink lines in Figure 4.6 (a, c)).

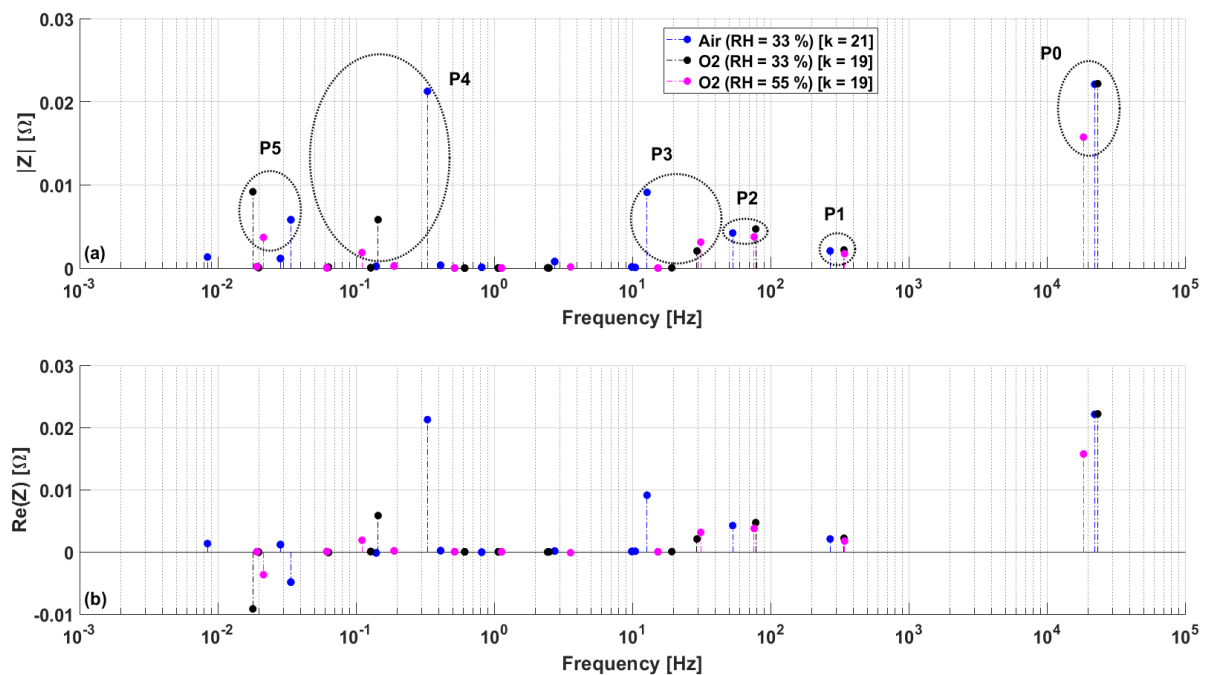


**Figure 4.7: (a) The DCF spectra correspond to Impedance spectra in Figure 4.6, (b) Real part of the DCF spectra.**

The corresponding DCF spectra are obtained in the Figure 4.7 for all the three cases (blue points for the base case ( $\text{H}_2/\text{air}$ ,  $\text{RH}=33\%$ ), black points for case 1 ( $\text{H}_2/\text{pure O}_2$ ,  $\text{RH}=33\%$ ) and pink points for case 2 ( $\text{H}_2/\text{pure O}_2$ ,  $\text{RH}=55\%$ )).

Note that the peaks (P3 - P5) are significantly affected when pure  $\text{O}_2$  is used in place of air, while the other peaks are only negligibly affected. As it was expected, the peaks P3 and P4 significantly decrease, since they lie in the same frequency range in which the mass transport of oxygen in GDL (10 Hz) and channel (0.7 Hz) are observed. For this reason, they can be attributed to these phenomena. The fact that they do not disappear completely using pure oxygen is due to the accumulation of water in the GDL, which obstructs the oxygen diffusion. Moreover, the peak P3 is affected by the charge transfer resistance of the ORR [21], [35]. These hypotheses are further demonstrated in the next sections.

With pure oxygen as input, the peak P2 attributed to the ORR charge transfer is shifted to the right in the spectra (see Figure 4.7). It is acceptable due to the faster kinetics of ORR as a result of the locally increased oxygen concentration and effective diffusivity. However, the magnitude of P2 remains constant due to the constant current density.

The P5 peak can be correlated to a low-frequency induction loop in the Nyquist diagram. Since the inductive behaviour of the cell is also shown in DCF spectra, by representing the spectra as a real part of the gain (Figure 4.7 (b)). However, the negative value of the gain (resistance) is not related to the physical inductive phenomena, but it is interpreted by the dynamics of the decrease in its resistance and has a lower characteristic frequency [38].

In Figure 4.7, it is also clear that the peaks P0, P4, and P5 are strongly influenced by the humidification of the gases (compare black and pink peaks). In this case, it is noticeable that both the Ohmic and polarization resistances decrease as the moisture content of the gases ( $\text{H}_2$  and  $\text{O}_2$ ) increases. The strong reduction of P0 (from 33% RH to 55% RH at constant current density) is explained by the dependence of proton conductivity on the water content of the membrane. Reactive gases with higher relative humidity cause a stronger absorption of water into the membrane, which results in a higher proton conductivity [20].

The change in relative humidity from 33% to 55% may not influence the dynamics of the charge transport. It also does not affect mass transport in the experiment due to the higher impact of liquid water produced by the ORR rather than the relative humidity of the feeds. Additionally, no influence of relative humidity of the feeds is observed on the kinetics (peaks P2 and P1).

The DCF spectra reveal the reduction in the dynamics of the membrane (P4 and P5) as humidity increases because the membrane is more sensitive to changes in the water balance under dry conditions [37]. That is because of P4 is related to membrane dehydration caused by electro-osmotic drag, whereas P5 is associated with the rehydration of the membrane by back diffusion.

### 4.3.1 Variation of current density in the case of H<sub>2</sub> and air as inputs:

To study the impact of the current change at low relative humidity (RH=33%) during H<sub>2</sub>/Air operation by means of DCF spectra, the impedance was recorded at different current densities ( $j = 100, 200, \text{ and } 300 \text{ mA cm}^{-2}$ ) while other parameters were kept constant (see Figure 4.8 and Figure 4.9).

As current increases, the high-frequency arc in the Nyquist diagram (Figure 4.8 (c)) reduced, while the medium-frequency loop expanded. However, the contributions of kinetics and mass transport are not separable. The DCF spectra (Figure 4.9) illustrate these changes more clearly. Here all peaks are directly or indirectly influenced by the current variation. As already discussed, P1 and P2 can be attributed to the hydrogen oxidation reaction (HOR) and ORR, respectively. Both these peaks are reduced as current increases, which points to a reduction in kinetic (activation) losses with increasing current density due to a larger over-potential [21].

Furthermore, P3 shows a significant decrease with increasing current density at a characteristic frequency of about 10-20 Hz. The strong current dependence of P3 indicates a relationship with the charge transfer kinetics of the oxygen reduction reaction (ORR) [12]. However, as already mentioned in section 4.2, P3 is also correlated with the diffusion of oxygen in GDL, since air is used as a cathode feed. Due to the strong coupling of these two phenomena, one cannot only assign P3 to the charge transfer kinetics of the ORR in H<sub>2</sub>/air mode, but one can allocate it to the kinetics of the ORR in the case of a very high oxygen flow at the inlet [20], [21].

As already discussed, a characteristic frequency of the peak P4 is within the frequency range of the mass transport phenomena in the channel as well as the dehydration phenomena induced by the electro osmotic effect. At higher currents, both the mass transport and the electro osmotic effects become stronger. Therefore, the amplitude of the peak P4 is more pronounced, and the characteristic frequency is shifted to the right in the spectra, indicating a faster dynamic [20], [32], [35].

The peak P0 refers to the Ohmic Resistance, which is lowered with increasing current because of increased hydration of the membrane due to water formation at the cathode [22], [39]. However, the peak P5 associated with membrane hydration, caused by back diffusion of water, has remained nearly constant in magnitude but shifted towards the higher frequency, indicating a faster dynamics of it with an increased current.

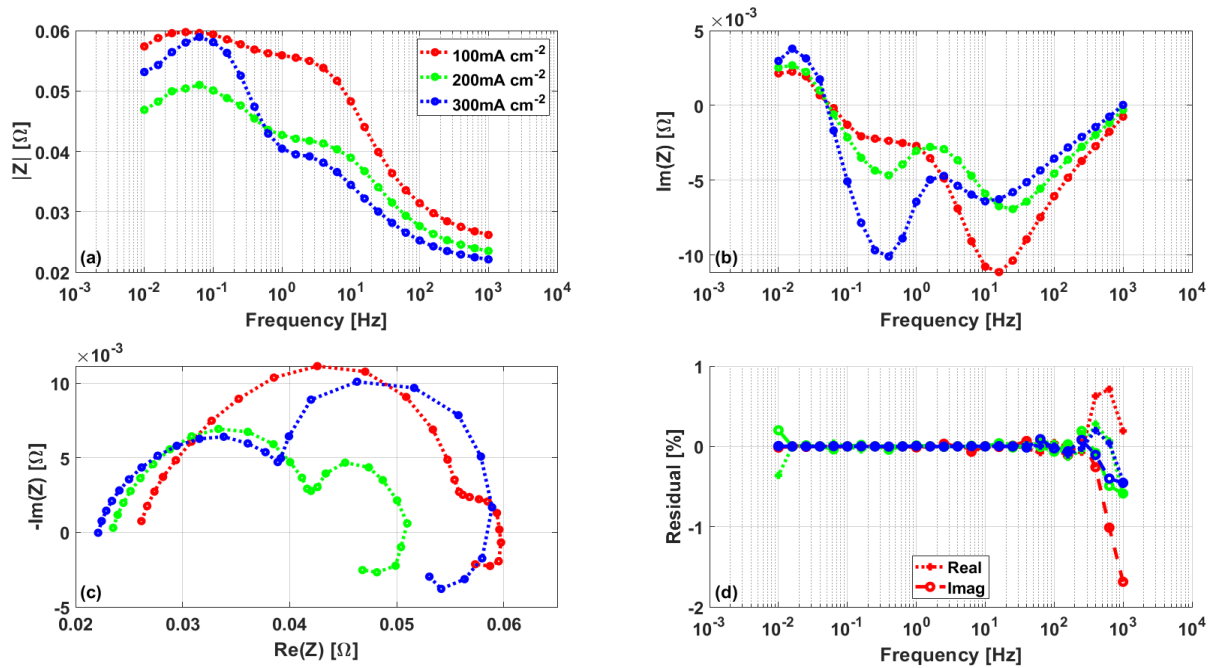


Figure 4.8: Variation of the current density (100 to 300 mA cm<sup>-2</sup>) of PEMFC operated with air and T = 80°C, RH=33 %. (a) Magnitude spectra, (b) Imaginary part of spectra, (c) Nyquist plot, and (d) Relative residuals.

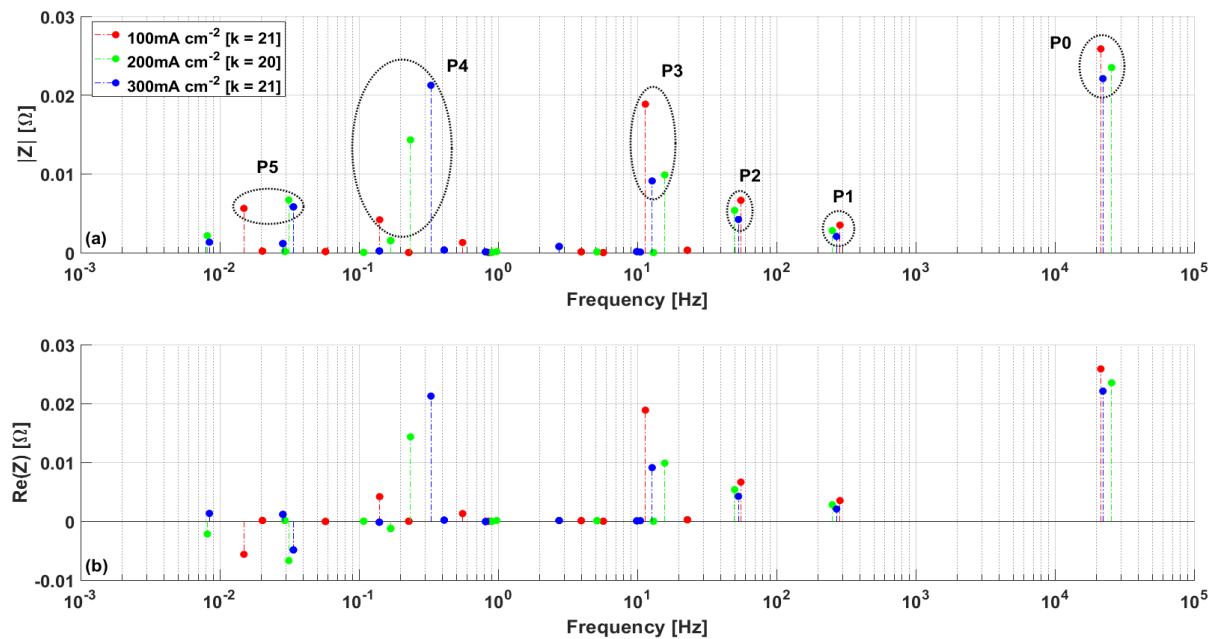
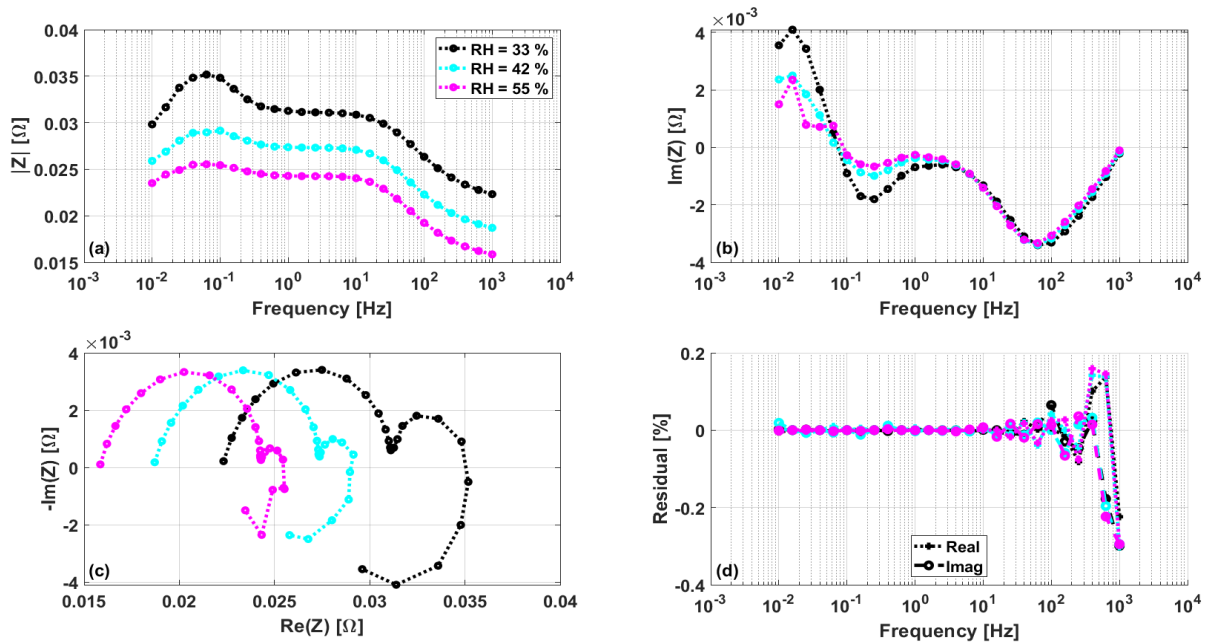


Figure 4.9: (a) The DCF spectra correspond to Impedance spectra in Figure 4.8, (b) Real part of the DCF spectra.

#### 4.3.2 Variation of humidity in the case of H<sub>2</sub> and O<sub>2</sub> as inputs:

To investigate how humidification of gases affects water transport phenomena in the membrane, the relative humidity was varied from 33% RH to 55% RH at constant current density ( $j = 300 \text{ mA cm}^{-2}$ ). Moreover, pure oxygen used as a cathode feed to minimize the impact of processes related to the mass transport. Figure 4.10 and Figure 4.11 show the impedance spectra and the equivalent the DCF spectra, respectively.



**Figure 4.10: Variation of the relative humidity (33 to 55 %) of PEMFC operated with pure  $\text{O}_2$  and  $T = 80^\circ\text{C}$ ,  $j=300 \text{ mA cm}^{-2}$ . (a) Magnitude spectra, (b) Imaginary part of spectra, (c) Nyquist plot, and (d) Relative residuals.**

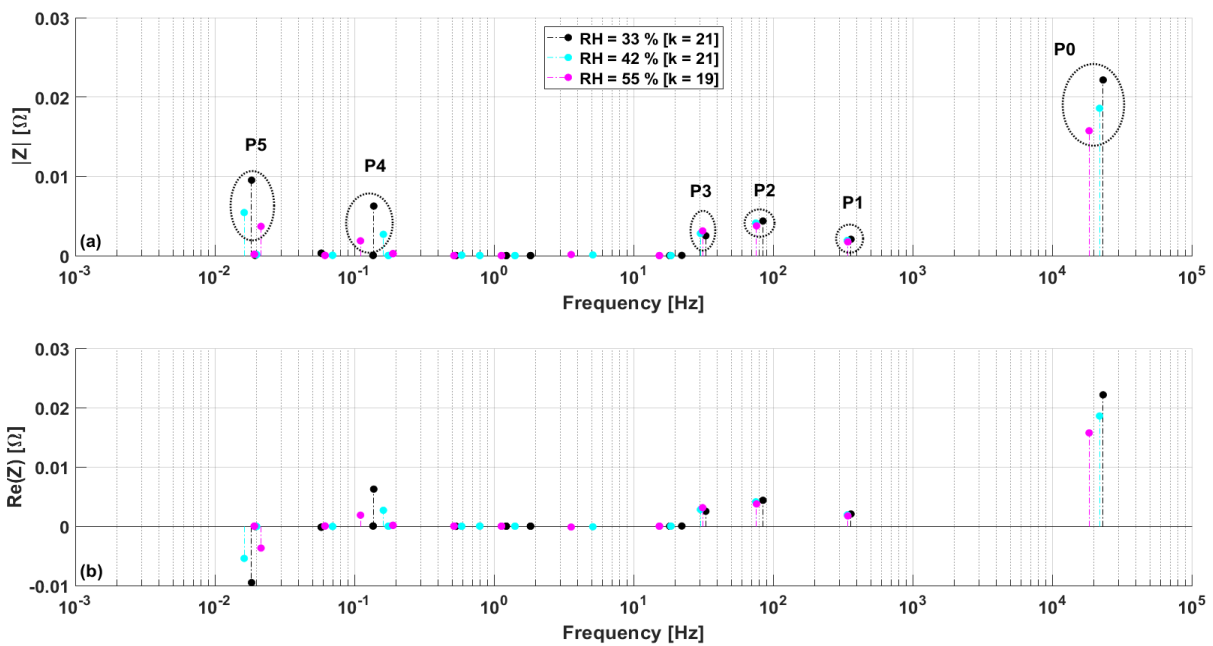


**Figure 4.11: (a) The DCF spectra correspond to Impedance spectra in Figure 4.10, (b) Real part of the DCF spectra.**

The DCF spectra show that the location of the peaks (P1, P2, and P3), which are attributed to kinetic charge transfer and mass transport in the GDL, remains steady when the relative humidity is changed. In addition, the magnitude of these peaks indicates only very little deviation, which suggests that the nature of these processes remains almost constant.

The peak P4 previously attributed to the dynamics of gas transport in the channel changes both location and magnitude along with the relative humidity of the feeds. This is

probably due to two reasons: (i) the decreased total flow rate going to lower humidity, which affects the time constant of this phenomenon, (ii) the decrement of the water mass transport in the GDL, which affects the magnitude.

Then, the peak P5 at low frequency is significantly influenced by humidification. This confirms the earlier assignment of this to the dynamics of water transport in the membrane. The DCF spectra indicate indeed the reduction of the impact of the membrane hydration with increasing moisture, since the membrane reacts more sensitively to changes in the water balance under dry conditions [37].

Moreover, as expected, the peak P0 associated with membrane resistance decreases with an increased relative humidity of the inflows because of the higher water content of the membrane [20].

#### 4.4 Analysis of simulated EIS spectra

In this section, simulated EIS spectra are examined by means of the DCF analysis. The impedance spectra are generated using a validated 1D mathematical model under the same operating conditions as previously considered for the experimental spectra in section 4.3.1. The experimental conditions and the values of the parameters used in the model are specified in section 8.2 in the Appendix. The model comprises gas transport in the channel and the GDL, water transport in the Nafion membrane and double-layer charging and discharging at the catalyst surface. The catalyst layer was considered as an interface, although the effect of liquid water formation in the cell was neglected. For details regarding the model, refer to the paper by Sorrentino et al. [3] and section 8.2 in the Appendix.

For comparison, the experimental spectra are also shown in Figure 4.12 (a, c, e) together with the simulated one (b, d, f) obtained at three different working points (100, 200, and 300 mA cm<sup>-2</sup>). The corresponding the DCF spectra are displayed in Figure 4.13. In addition, the relative residuals are shown in Figure 8.5 in the Appendix. As shown in Figure 4.12, the simulated spectra are qualitatively well matched to the experimental ones across the entire frequency range, although the DCF spectra of the model show most of the peaks.

The Peak associated with Ohmic resistance P0 has almost the same magnitude range in the experiment and simulation. Moreover, its value decreases with increased current density because of the water content in the membrane increased by the additional water production at the cathode.

The peak P1 related to the HOR is negligible and basically has no impact on the performance losses. The peak P2 associated with the oxygen reduction reaction (ORR) is shifted to a higher characteristic frequency, which indicates the faster kinetics of the ORR due to a larger overpotential with the increased current in the simulation.



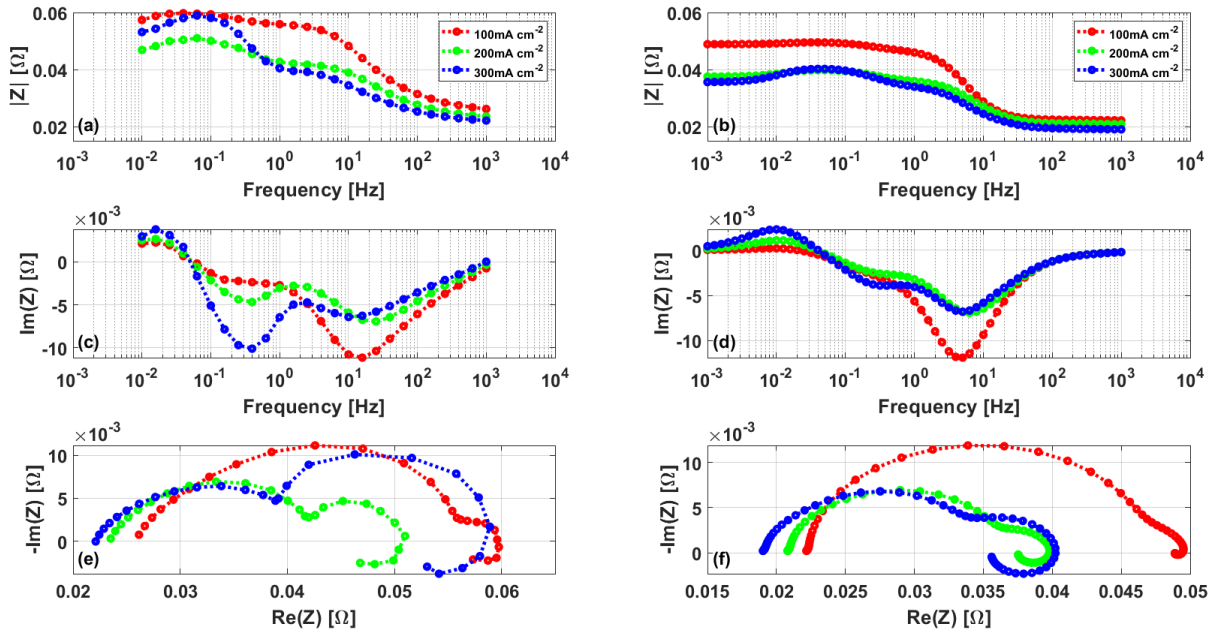


Figure 4.12: Experimental (a, c, e) and simulated (b, d, f) EIS spectra of PEMFC operated with air and  $T = 80^{\circ}\text{C}$ ,  $\text{RH}=33\%$  for 100, 200, and 300  $\text{mA cm}^{-2}$ . Magnitude spectra (a, b), Imaginary part of spectra (c, d), and Nyquist plot (e, f).

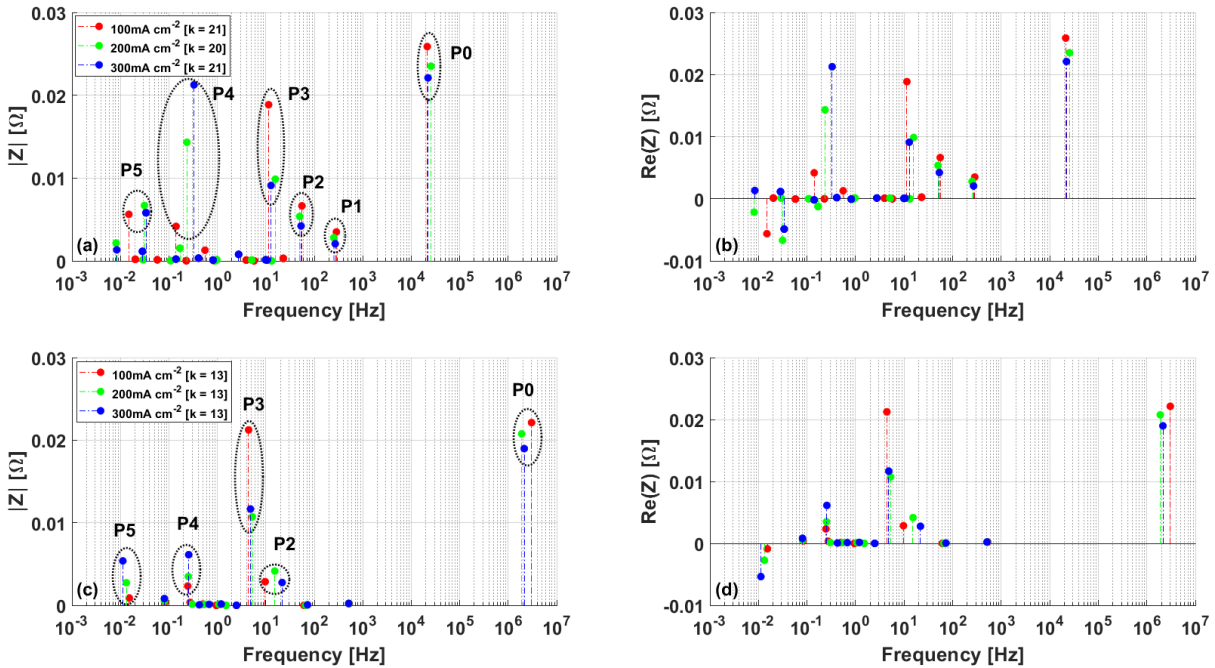


Figure 4.13: The DCF spectra correspond to EIS spectra in Figure 4.12 (a, c), a Real part of the DCF spectra (b, d). The experimental (a, b) and simulated (c, d) spectra.

As already described, the peak P3 is related to both the ORR and the mass transport resistance of the GDL when air is used as cathode feed because of the interconnection of these two processes. This is also visible in the case of the simulated spectra in Figure 4.13(c-d).

Furthermore, the characteristic frequencies of peak P4 and P5 are almost the same as the experimental ones. Besides, the peak P4 is more pronounced in the experiment than in the simulation, as the current density increased. This is because peak P4 is correlated with

the mass transport effect along the channel, and this phenomenon is highly dependent on the current.

Whereas the peak P5 is concerned with the hydration of the membrane resulting from the back diffusion, the dependence of this phenomenon on the current density is visible in the simulation. Its magnitude increases with the current density because the water production on the cathode side increases. Thus, the proton conductivity of the membrane is enhanced. Consequently, the peak P5, which corresponds to the negative resistance in the spectra, is also amplified.

## 5 cFRA

### 5.1 Analysis of cFRA experimental data

In this section, analysis of cFRA experimental data of a PEMFC is discussed. First, the results of the spectral analysis performed on the data in the time domain are shown. According to this, indications on the reduction of the time required for the experiments are given. Then, the determined cFRA spectra under different operating conditions are analysed and discussed.

For each specific operating condition, there are 17 experimental data sets in the time domain. Each data set consists of the perturbation of the input (oxygen and/or water partial pressure) and the corresponding output response (voltage or current) as periodic signals at different frequencies. The signals are restricted in a frequency range between 0.01 Hz and 1 Hz due to the limitations of the setup, which is not capable to produce periodic inputs at higher frequencies.

In this section, the focus is only on the analysis of cFRA data, so only one input (oxygen partial pressure) and one output (voltage) is considered as an example. As shown in Figure 5.1 (a-c), the frequencies of the signals are lower as one passes through data sets No. 1 to 17. Additionally, the signals are turned from sine waves (for data set No. 1) into nearly square waves (for data set No. 17). Because of this, the frequency spectra derived from the Fourier transform of these signals contained different harmonics beside the fundamental frequency, especially for low-frequency signals, as shown in Figure 5.2 (a-c).

Therefore, instead of taking only the harmonic at the highest frequency (the fundamental one), one should also consider all the other dominant frequencies. Thus, all dominant frequencies and the corresponding spectrum of input and output for all data sets are collected for further analysis.

Figure 5.3 shows all dominant frequencies collected from all 17 data sets. Note that both odd and even harmonics are taken from data sets no. 1 to 6, while only odd harmonics are collected from data sets no. 7 to 17, because in the latter case the signals are almost square waves. In general, only odd harmonics contain the most information about the square wave.

After obtaining all the dominant frequencies and the respective FFT spectra of input and output, the spectrum ratio (transfer function) between output (voltage) and input (oxygen partial pressure) at all the dominant frequencies can easily be determined (as shown in equation (2.2)).

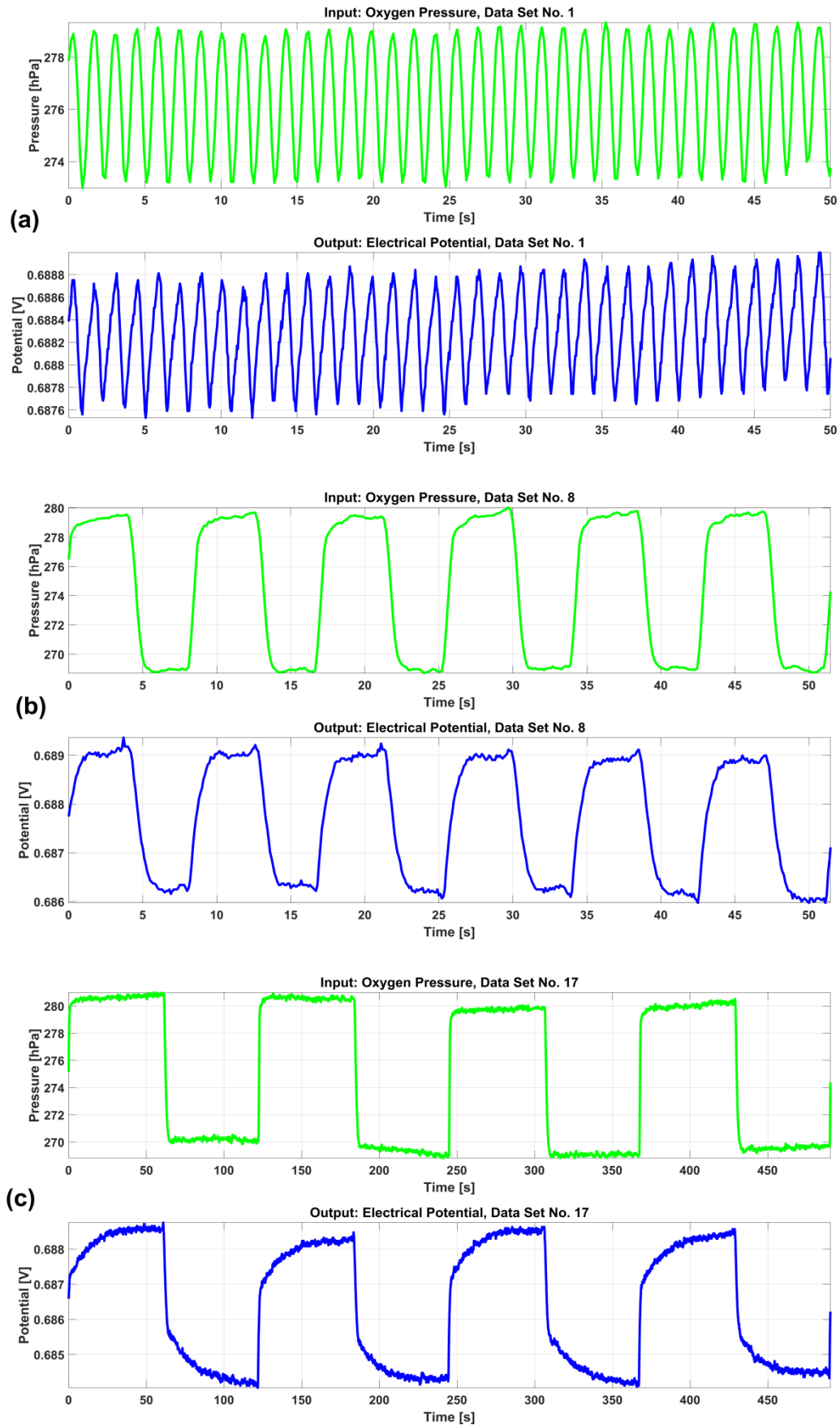


Figure 5.1: The perturbation of the input (oxygen partial pressure) and the corresponding output response (electrical potential) as periodic signals for data set no. 1, 8, and 17 (a-c).

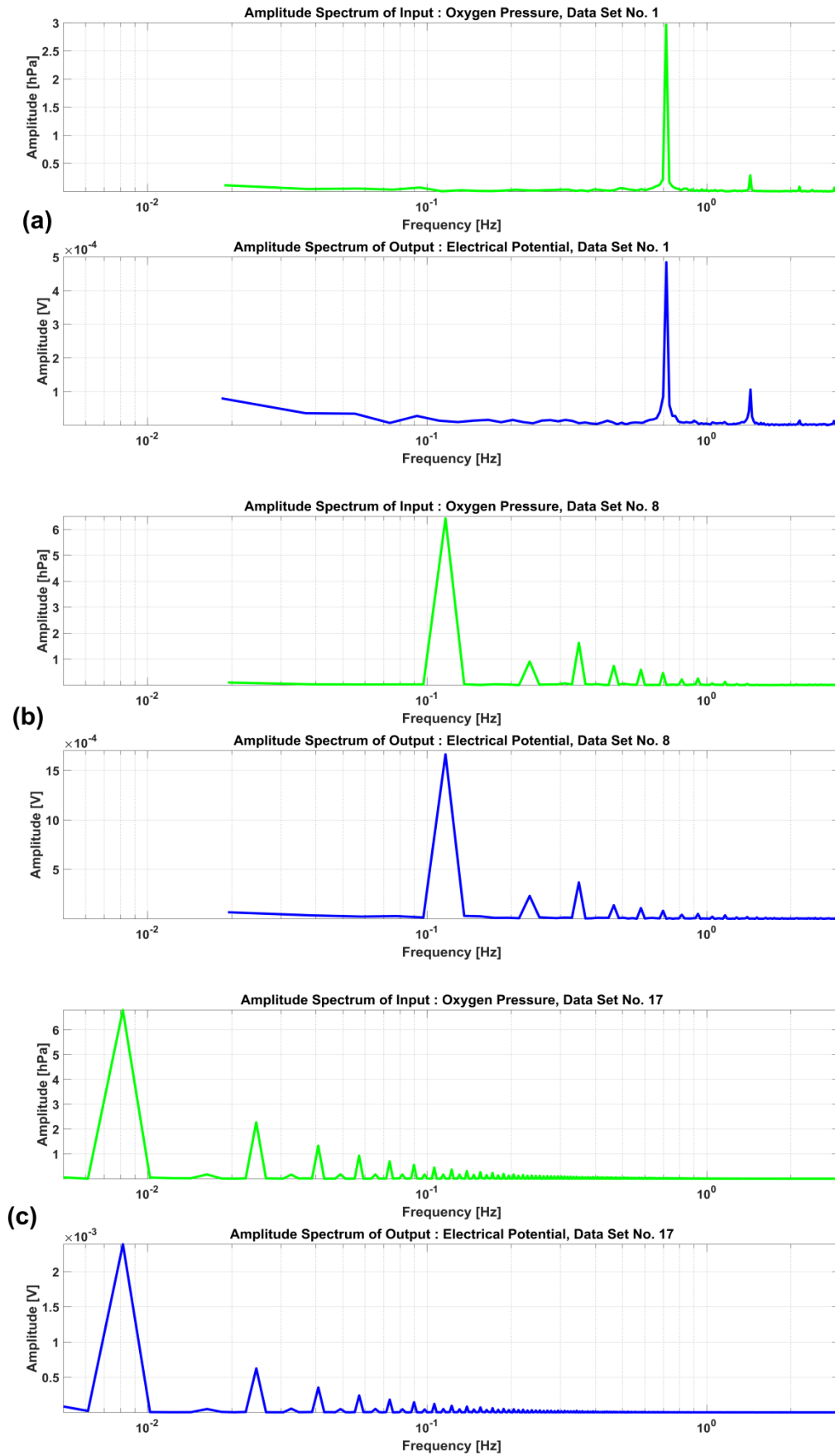
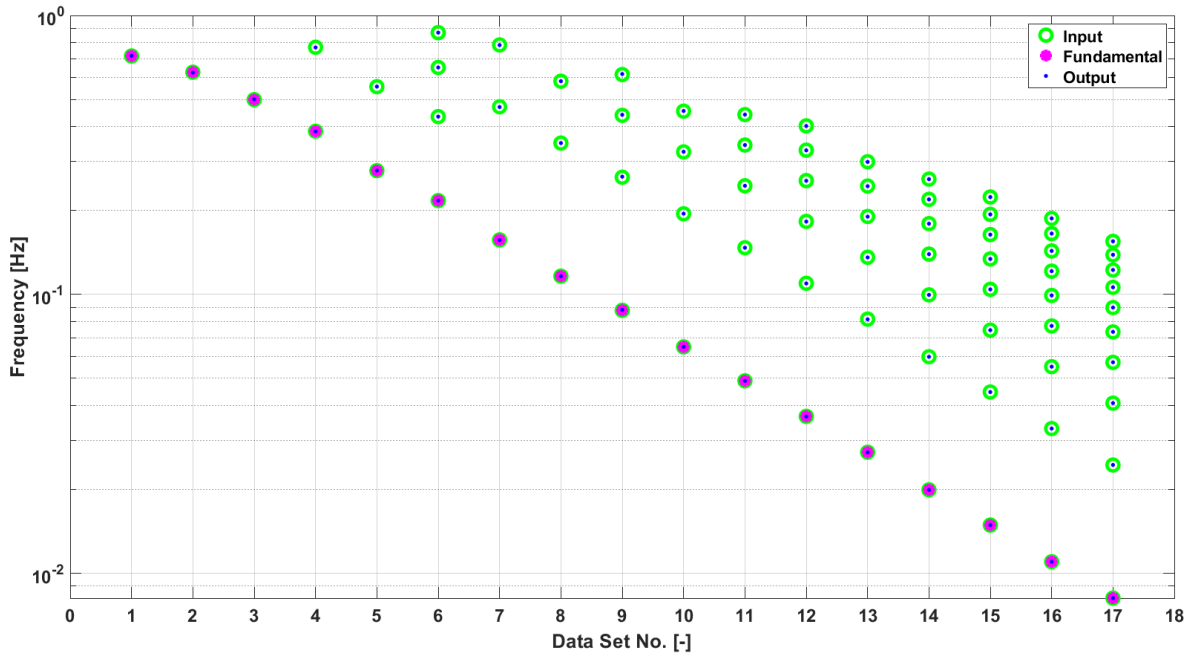
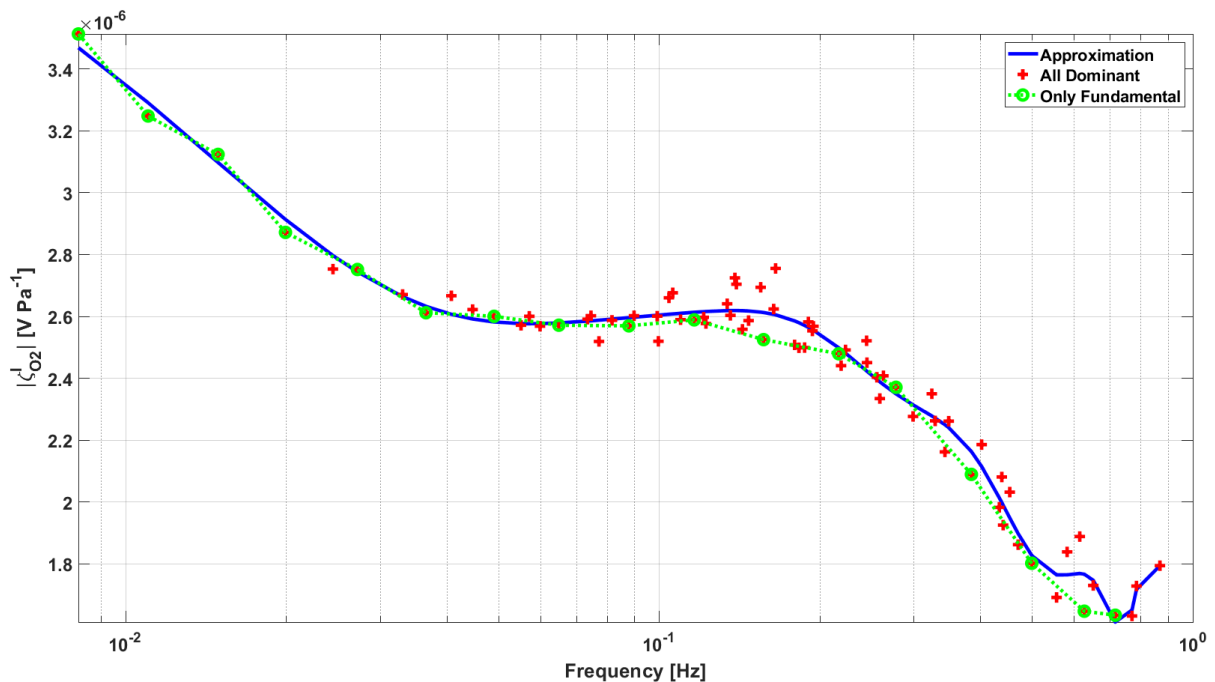


Figure 5.2: Fourier transform amplitude spectra correspond to the periodic signals in Figure 5.1 (a-c).



**Figure 5.3: Dominant Frequencies of the Input and Output signals for all data sets.**

Figure 5.4 displays the magnitude spectra at all dominant frequencies (red crosses). For comparison, the cFRA spectra, which correspond to the most fundamental frequencies, is also shown in the same figure (green circles).



**Figure 5.4: Magnitude spectra of galvanostatic cFRA O<sub>2</sub>.**

Experimental data have a bit scattering behaviour, so it is useful to approximate them for better interpretation and understanding. There are many approaches and tools are available for the data approximation (or smoothing), such as Polynomial interpolation, Moving average filtering, Gaussian-weighted moving average, Linear and Quadratic regression, Savitzky-Golay filter, and so on [40]–[42].

In this thesis, polynomial interpolation is employed for fitting the curve to the cFRA data because of its simplicity. However, there are many limitations of the polynomial fitting, but here it is used only to follow the overall behaviour of the spectra for better visualization and understanding. As shown in Figure 5.4, the blue curve describes an approximation of the data (red crosses) with a polynomial of degree 12.

From Figure 5.4 it becomes obvious that this approach can capture more dynamics (especially in the mid to high-frequency range) compared to the earlier one, where only the harmonics of the most important frequency are taken into account (green circles). Hence, this new strategy offers a better resolution and tries to avoid uncertainties in the spectra due to measurement errors.

Besides this, there is also the possibility to shorten the experiment time by reducing the number of data sets, if one can identify sub-datasets (five or six) instead of 17 that contain the frequencies, which associated spectra are close to the trajectory of the data (curve) and cover the frequency range of interest. In the following section, the feasibility to reduce the time for cFRA experiments by using the Loewner framework is discussed.

## 5.2 cFRA experimental time reduction

As discussed in the previous section, a group of six sub data sets out of a total of 17 data sets is the most suitable, since contains the frequencies which corresponding spectra near the trajectory of the data of all 17 data sets (curve) and cover the frequency range of interest. However, 12376 different groups are possible for six sub-datasets out of 17 data sets according to  ${}^nC_6$ . Thus, one should try every possible combination to get the most appropriate one. The approach to get this is explained in the form of a flowchart (see Figure 5.5).

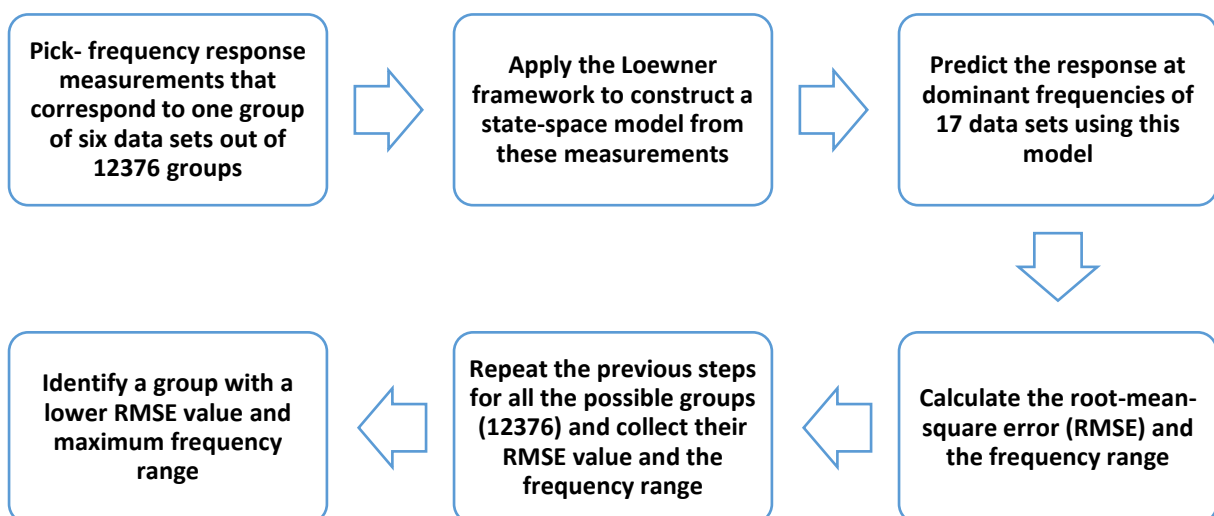


Figure 5.5: Procedure for identifying the best group of six data sets among 12376 possible groups that approximate the response of all 17 data sets.

By applying this methodology, a group of the data sets (1, 6, 7, 12, 14, and 17) is identified here as the most favourable group, and its corresponding root-mean-square error (RMSE) and frequency range is shown in Figure 5.6 (marked as a light blue circle), which displays the RMSE and frequency range of all groups. In this figure, one can observe that this group has a lower RMSE, and it is covering the maximum frequency range.

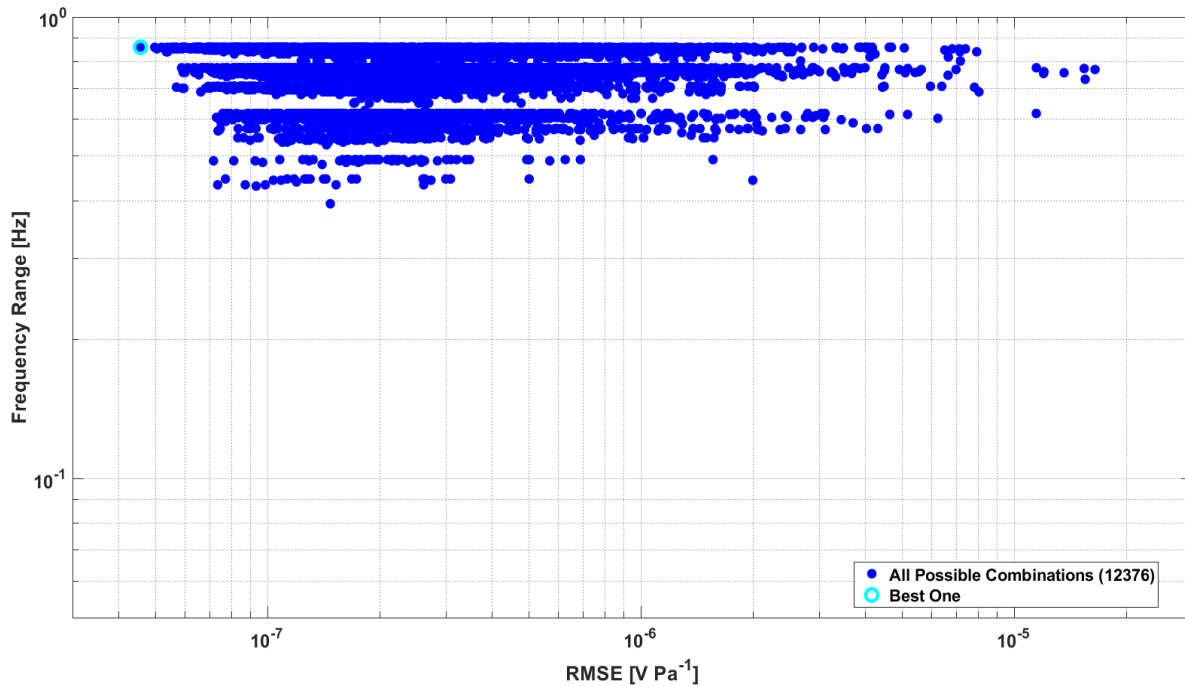


Figure 5.6: Frequency range vs root-mean-square error.

### 5.2.1 Confirmation with similar cFRA experimental data

In this section, the magnitude spectra of the previously obtained best six data sets is plotted together with the magnitude spectra of all 17 data sets, making it clear that these sub-data sets are capable to follow the nearly identical path of all 17 data sets across the entire frequency range. Figure 5.7 shows the dominant frequencies of six data sets (green circles). In Figure 5.8, the blue curve and the black curve represent an approximation of the spectra of 17 data sets (red crosses) and six data sets (light blue circles), respectively, both having the polynomial degree 12. It is remarkable from the figures that these six data sets can substitute the 17 data sets and reduce a significant amount of the measurement time. In this case, the total measurement time for the 17 data sets is 40.6 minutes, whereas the duration of these six data sets is around 16.4 minutes. In this way, about 60 % of the overall time can be shortened ( $= \frac{40.6-16.4}{40.6} \times 100 \approx 60 \%$ ).

It must be remarked that the polynomial fitting in this chapter is only used for better visualization and understanding of the cFRA spectra.



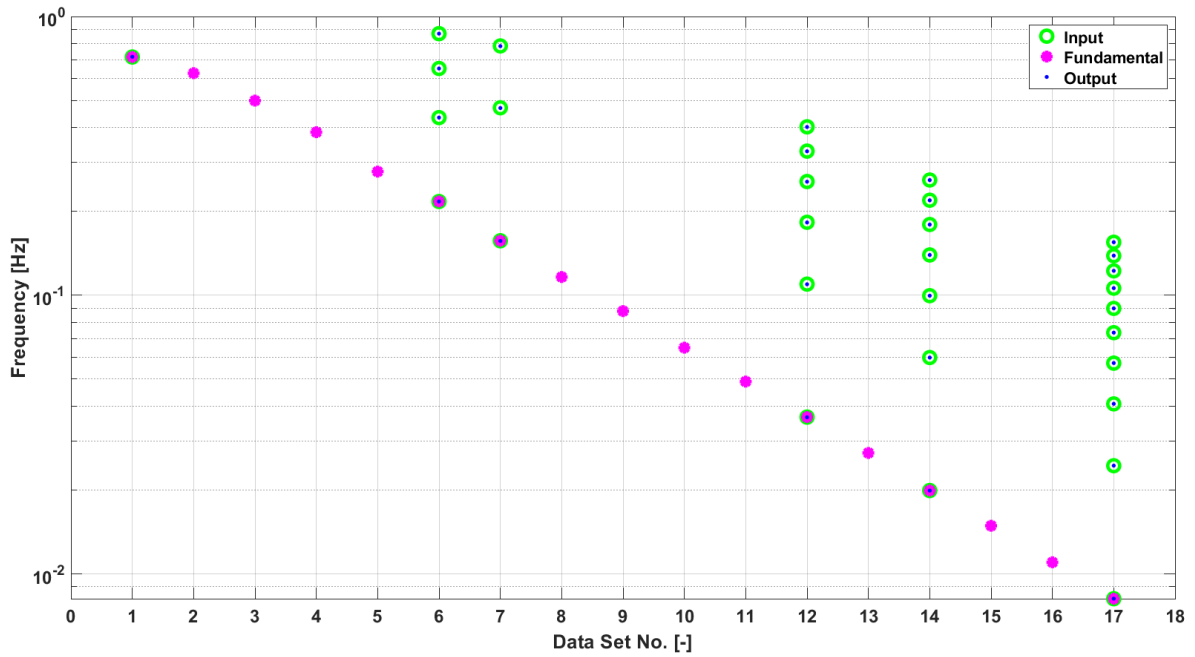


Figure 5.7: Dominant frequencies of the input and output signals for six data sets.

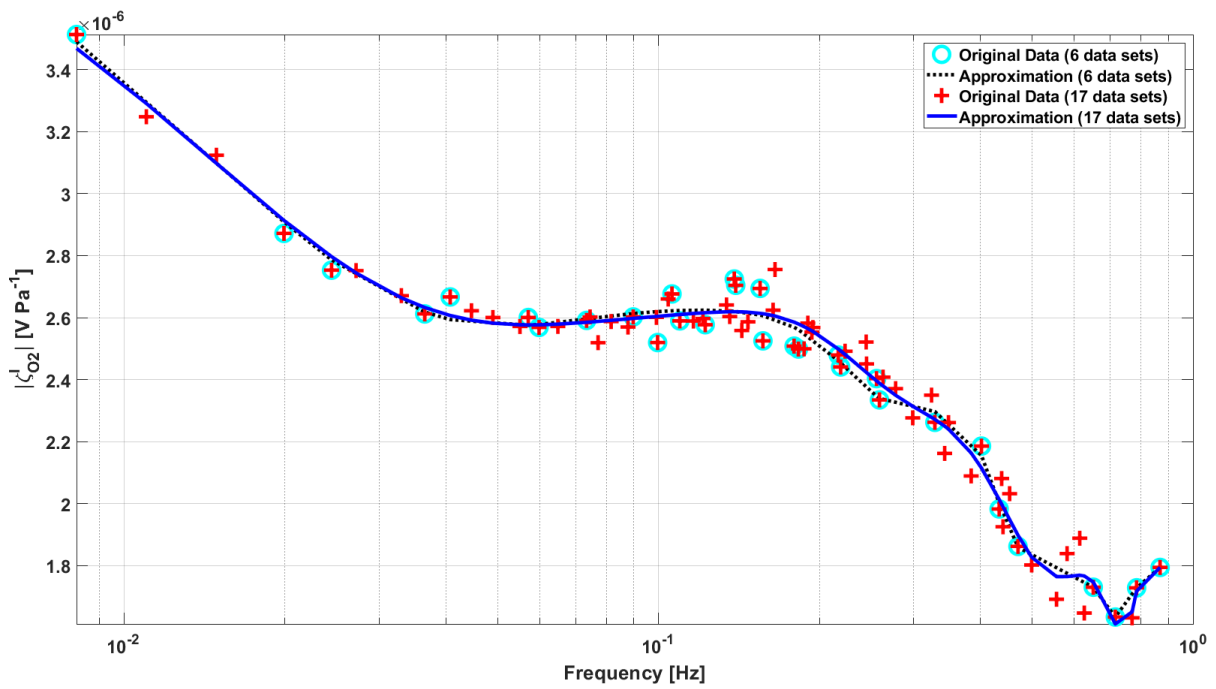


Figure 5.8: Magnitude spectra of galvanostatic cFRA  $O_2$  for both all-17 data sets and six data sets.

### 5.3 cFRA O<sub>2</sub>

In order to study the dynamics of the PEMFC associated with mass transport by DCF analysis, the cFRA spectra are measured by oxygen partial pressure perturbations under different operating modes (voltastatic and galvanostatic), see eqs. (2.1) and (2.2). Figure 5.9 shows the experimental spectra obtained at three different working points (100, 200, and 300 mA cm<sup>-2</sup>) in galvanostatic (a-b) and voltastatic (c-d) mode, and the respective DCF spectra are also displayed in Figure 5.10.

Notice that the experimental spectra shown in Figure 5.9 are an approximation of the actual data for a better interpretation and understanding (see Figure 8.7 for galvanostatic and Figure 8.8 for voltastatic in section 8.3 in Appendix). However, the actual data were used to obtain the respective DCF spectra as displayed in Figure 5.10. That is also valid for all the cases. As the focus is on the study of the main dynamics in the cFRA spectra, the rank of the Loewner matrix is selected as the order of the model  $k$  in all cases. Thus, the relative residuals are very small (less than 0.1%) over the whole frequency range, which confirms the reproducibility (see Figure 8.10 (a, c) in section 8.3 in Appendix).

As discussed in the chapter 4 in the study of EIS spectra, generally three dynamics are observed in the frequency range of 0.01 - 1 Hz. First one is mass transport of oxygen in the GDL, second one is the transport of oxygen along the channel, and last one is hydration of membrane because of back diffusion of water.

There is only one clear dynamics is observed in the galvanostatic as well as in the voltastatic mode. The associated characteristic frequencies can be identified by an inflection point in the magnitude spectra or by the turning point in the imaginary part of the spectra [3]. Even in the DCF spectra around 0.1 Hz a clear peak (denoted as 1) can be seen. This phenomenon (1) is caused by the mass transport of oxygen along the channel and also by oxygen transport through the GDL to the electrode surface.

Besides, a small but visible peak (marked as 3) can be observed in voltastatic mode at 0.03 Hz only at a 300mA cm<sup>-2</sup> current density (see Figure 5.10 (c-d)). It is mostly because of water transport in the membrane caused by back diffusion. However, it was only seen at higher current density due to the higher water production at the cathode side. It does not appear in the galvanostatic spectra because there is a constant water production by the ORR at the cathode and consequently uniform hydration of the membrane, which is not a dynamic element under this operating condition [3].

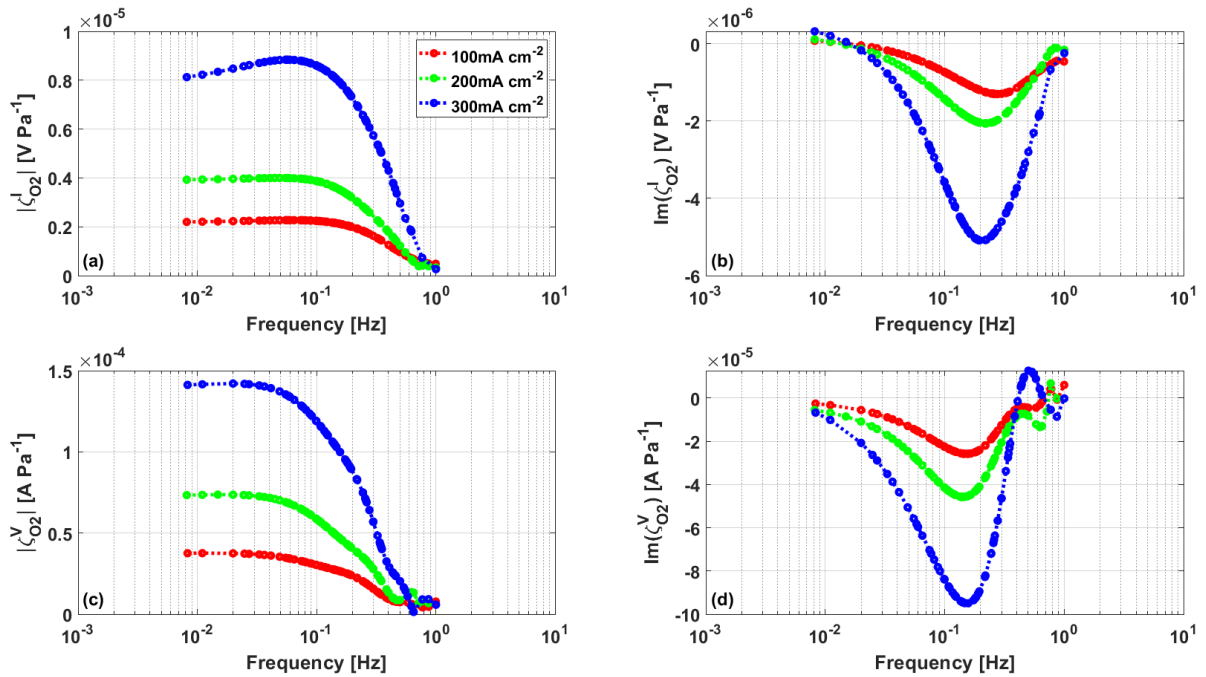


Figure 5.9: Experimental cFRA  $O_2$  spectra under galvanostatic (a-b) and voltastatic (c-d) control for 100, 200, and 300  $mA\ cm^{-2}$ .

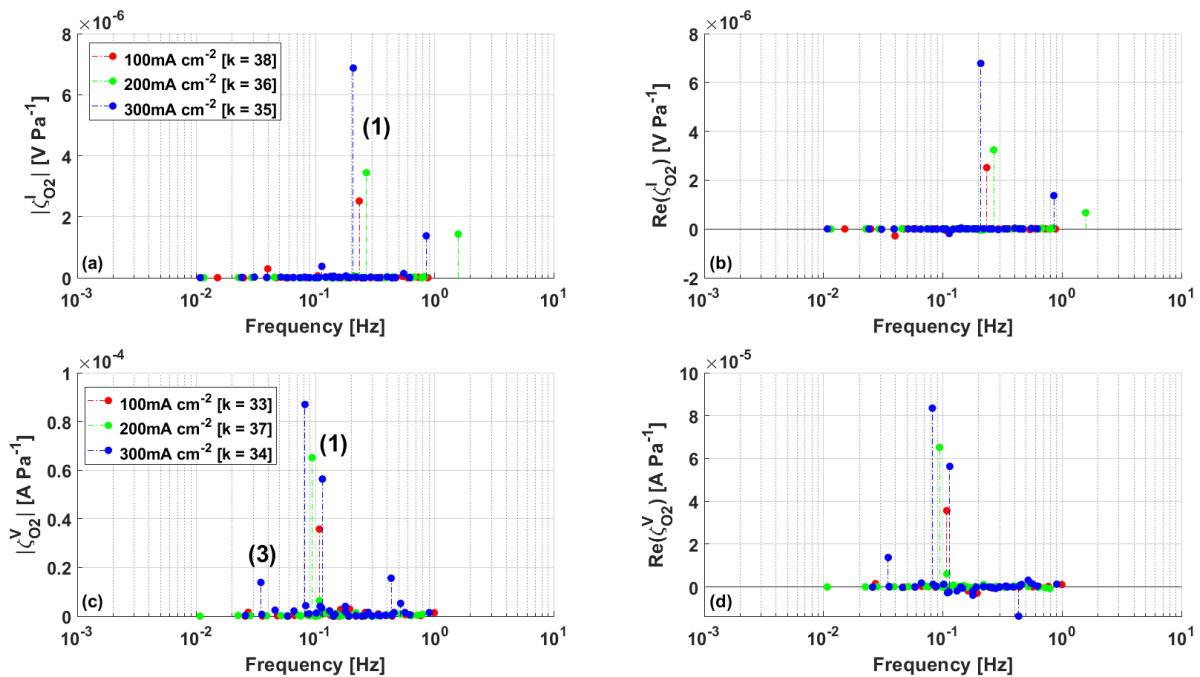


Figure 5.10: The DCF spectra correspond to cFRA  $O_2$  spectra in Figure 5.9 (a, c), Real part of the DCF spectra (b, d).

To make comparisons, the cFRA spectra are simulated by a validated numerical 1D model at the same operating conditions that have been previously considered for the experiment. The details about the model and the parameter values taken in the model are described in section 8.2 in Appendix. The results are displayed in Figure 5.11 and the corresponding DCF spectra are provided in Figure 5.12. Also, relative residuals are shown in Figure 8.10 (b, d) in the Appendix.

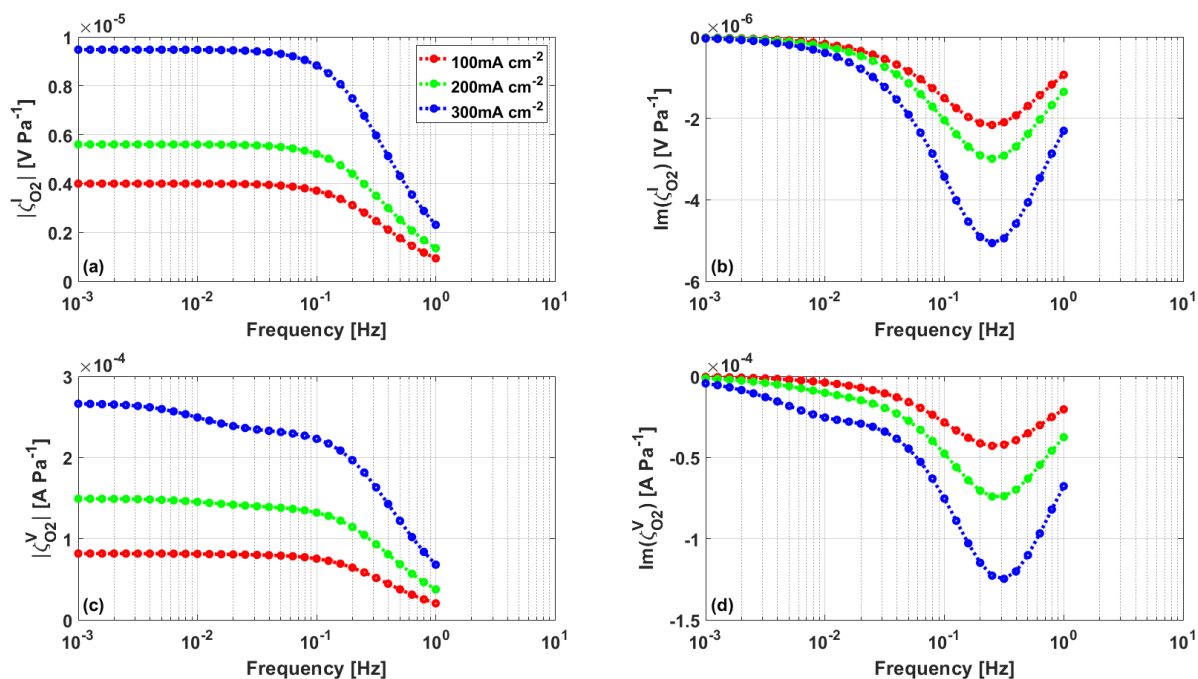


Figure 5.11: Simulated cFRA  $O_2$  spectra under galvanostatic (a-b) and voltastatic (c-d) control for 100, 200, and 300  $\text{mA cm}^{-2}$ .

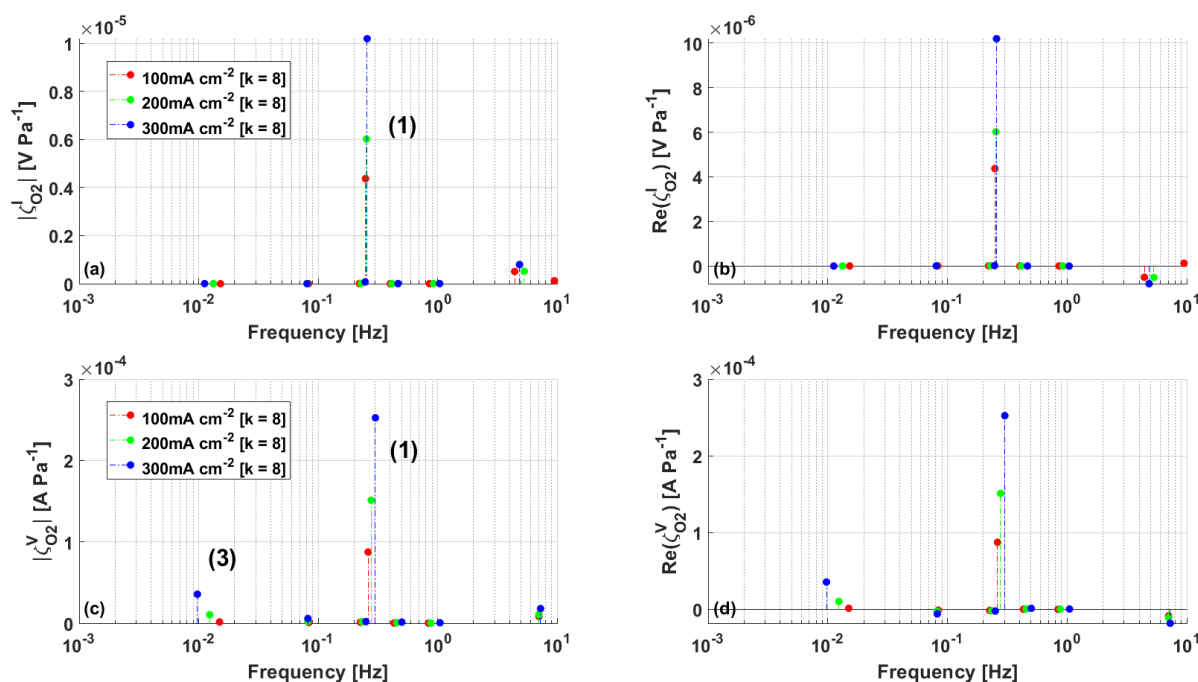


Figure 5.12: Simulated DCF spectra correspond to cFRA  $O_2$  spectra in Figure 5.11 (a, c), Real part of the DCF spectra (b, d).

As can be seen, the theoretically calculated cFRA spectra are qualitatively well matched to the experimental oxygen cFRA spectra with a Frequency range lower than 0.5 Hz. In the simulations (see Figure 5.11 & Figure 5.12), phenomena (1) in the galvanostatic mode (a-b) and phenomena (1) and (3) in the voltastatic mode (c-d) appear in almost the same frequency range to the respective experimental spectra. These phenomena are related to gas transport in the channel (1) and water transport in the membrane (3), respectively, as discussed previously.

## 5.4 cFRA H<sub>2</sub>O

To understand the water transport phenomena in the membrane of the PEMFC through DCF analysis, the cFRA spectra obtained by water partial pressure perturbations at three different working points (100, 200, and 300 mA cm<sup>-2</sup>) in the galvanostatic mode (see, eq. (2.2)) are illustrated in Figure 5.13 (a-b), and simulated spectra of cFRA-H<sub>2</sub>O generated by the theoretical model under the same condition are also displayed in Figure 5.13 (c-d) for comparison. The respective DCF spectra can be seen in Figure 5.14 and relative residuals displayed in Figure 8.10 (e-f) in the Appendix. Remember that the experimental spectra depicted in Figure 5.13 (a-b) are an approximation of the real data to allow clear interpretation (see Figure 8.9 in Appendix). Nevertheless, the original data were employed for determining the DCF spectra.

There are three distinct dynamics visible in the magnitude and imaginary part of the experimental spectra in Figure 5.13 (a-b), whereas in the case of the simulated spectra in Figure 5.13 (c-d) only two phenomena are visible. Interestingly, three clear peaks can be seen in the DCF spectra related to simulated ones (see Figure 5.14 (c-d)), thus the DCF analysis facilitates a better decoupling of the phenomena.

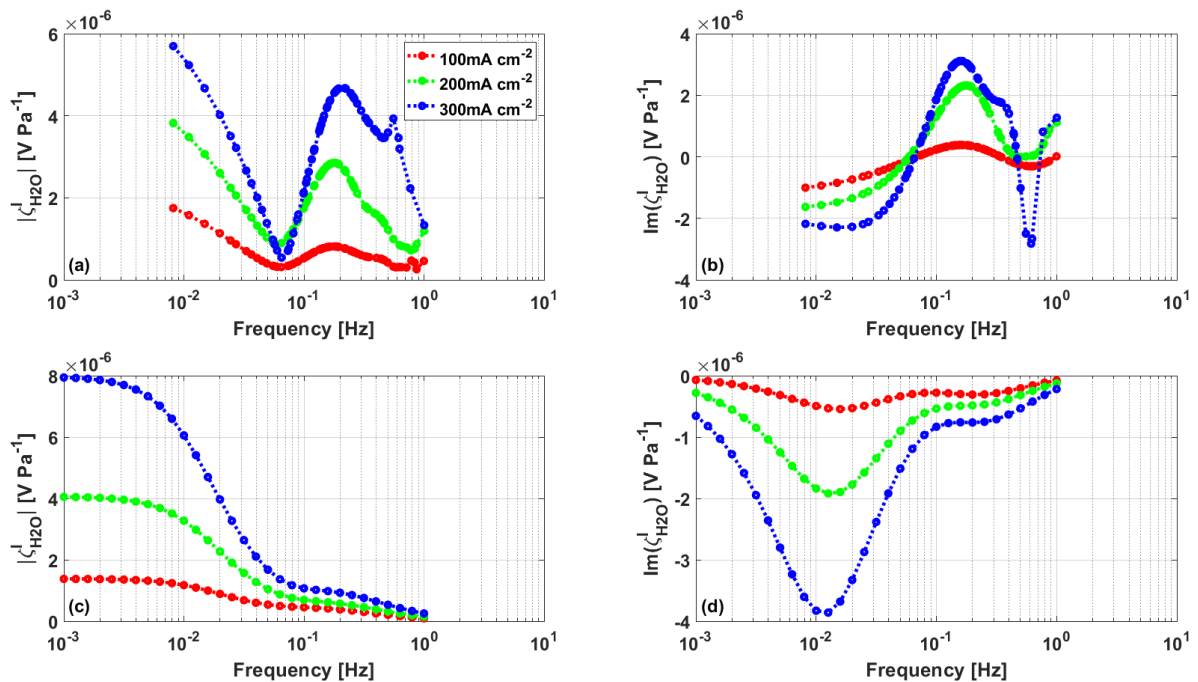
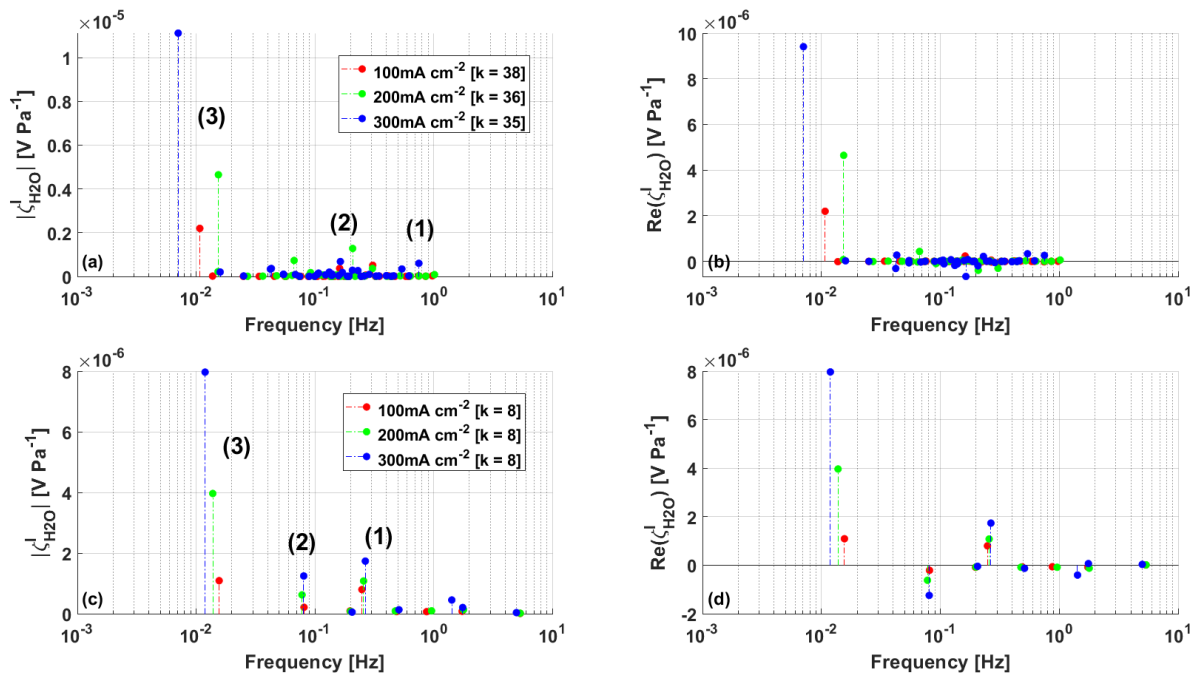


Figure 5.13: Experimental (a-b) and simulated (c-d) cFRA H<sub>2</sub>O spectra under galvanostatic control for 100, 200, and 300 mA cm<sup>-2</sup>.



**Figure 5.14: The DCF spectra correspond to cFRA H<sub>2</sub>O spectra in Figure 5.13 (a, c), Real part of the DCF spectra (b, d). The experimental (a, b) and simulated (c, d) spectra.**

Figure 5.14 displays a very distinct peak (denoted by 3) for both the experimental and the simulated spectra in the low-frequency range around 0.01 Hz. This characteristic frequency refers to the water transport phenomena in the membrane, which are caused by the slow diffusion of the water in the membrane. Only at very low frequencies, the water partial pressure signal has sufficient time to diffuse through the whole membrane. As a result, the water content of the membrane changes and affects the membrane resistance. Consequently, the voltage increases when the water partial pressure is increased, and vice versa.

Furthermore, at the higher current density, this phenomenon (3) is more pronounced due to the electro osmotic effect that dries out the membrane strongly. As drier the membrane becomes, the stronger the effect of changes in the water balance on the membrane resistance and so on the voltage [37].

Indeed, the dynamics associated with gas transport in the channel (around 0.1 Hz) can be recognized in the DCF spectra (Figure 5.14). However, it is very noticeable in the simulated spectra, but partly visible in the experimental spectra.

## 6 Conclusion and Future Suggestions

### 6.1 Conclusion

A data-driven approach to study the different dynamics of a PEMFC is developed in this thesis. To accomplish this, the Loewner framework is employed as a data-driven approach. Subsequently, this novel method named the distribution of the characteristic frequency (DCF) was successfully applied for analysing the EIS and the cFRA experimental spectra of a PEMFC as well as simulated spectra of a validated 1D numerical PEMFC model. The DCF analysis of the EIS experimental spectra revealed five distinct peaks that correspond to the polarization processes and one peak representing the Ohmic. On the other hand, only three different dynamics could be distinguished through the patterns of the Bode and the Nyquist plots, which pointed to a de-coupling of the phenomena having comparable time constants.

In order to assign each of these peaks to the various internal phenomena of the PEMFC, specific experimental conditions (feed composition and current density) were applied. As a result, all the peaks were successfully allocated. For example, a peak above 100 Hz is attributed to the HOR, a peak around 50 Hz is contributed to the ORR, while peaks around 10 Hz are the result of both the ORR and the mass transport of the oxygen in the GDL, a peak around 0.1 Hz is caused by the mass transport losses along the channel, whereas a peak around 0.01 Hz is related to the membrane hydration due to back diffusion. Finally, a peak of over 10 kHz represents the Ohmic resistance. Additionally, the DCF analysis of the simulated EIS spectra has detected most of the peaks apart from a peak that corresponds to (HOR). Nevertheless, the other peaks are qualitatively well matched to the experimental ones.

The DCF analysis of the experimental and simulated cFRA spectra of O<sub>2</sub> has effectively identified the peaks that are associated with oxygen mass transport phenomena in the GDL and/or the channel as well as water transport phenomena within the membrane, depending on the operating modes (galvanostatic and voltastatic) confirming the hypothesis of previous studies. In addition, the DCF analysis of the cFRA spectra of H<sub>2</sub>O also revealed peaks with respect to these dynamics.

This work confirms that clear identification of the polarization losses based on their characteristic frequencies (time constants) is feasible and this leads to a detailed understanding of the electrochemical phenomena occurring in the PEMFC. This method has considerable benefits in terms of high resolution, allows easy reading of impedance values, and determines the distribution of characteristic frequencies directly from frequency response measurement.

In addition, the cFRA experimental spectra were analysed considering all the dominant harmonics in addition to the fundamental frequency, which allowed minimizing the number of data sets (or measurement points) that are required in order to obtain the

frequency range of interest, instead of 17 to only six. As a result, the present duration of measurement for each experiment under specific operating conditions can be shortened by up to 60 %.

### 6.2 Future suggestions

The previous discussion reveals that this novel approach is a very powerful way of studying EIS and cFRA spectra. The only constraint that prevents it from being a black-box approach is the selection of an order of the state-space model  $k$ . The model order  $k$  is a very crucial parameter that determines the quality of the DCF spectra. In the case of excellent data quality or ideal data, it is possible to take a higher value of  $k$  (the rank of the Loewner matrix), but for experimental or real data, it is necessary to choose an appropriate value. An improper value of  $k$  leads to incorrect peaks as well as a shift in the frequency and magnitude of the peaks in the DCF spectra due to an over-fitting of the model to the noise. Thus, in order to deal with noisy data, prior knowledge of the system is required for a proper selection of this parameter. Hence, one needs to define some criteria in order to choose the order of the state-space model, which can automate this approach.

The presented analysis offers an excellent foundation for improving the performance of the mathematical model, as this approach allows clear identification of the contribution of the individual loss mechanisms occurring in the PEMFC, quantitatively. Thus, accurate insights of each of the phenomena are possible by comparing the DCF spectra for both experiment and simulation. Hence, the improvement in the performance of the numerical model can be achieved by modifying associated model parameters in the simulation.



## 7 References

- [1] A. M. Niroumand, W. Mérida, and M. Saif, “PEM fuel cell low flow FDI,” *J. Process Control*, vol. 21, no. 4, pp. 602–612, 2011, doi: 10.1016/j.jprocont.2010.12.013.
- [2] E. Engebretsen, T. J. Mason, P. R. Shearing, G. Hinds, and D. J. L. Brett, “Electrochemical pressure impedance spectroscopy applied to the study of polymer electrolyte fuel cells,” *Electrochem. commun.*, vol. 75, pp. 60–63, 2017, doi: 10.1016/j.elecom.2016.12.014.
- [3] A. Sorrentino, T. Vidakovic-Koch, R. Hanke-Rauschenbach, and K. Sundmacher, “Concentration-alternating frequency response: A new method for studying polymer electrolyte membrane fuel cell dynamics,” *Electrochim. Acta*, vol. 243, pp. 53–64, 2017, doi: 10.1016/j.electacta.2017.04.150.
- [4] A. Sorrentino, T. Vidakovic-Koch, and K. Sundmacher, “Studying mass transport dynamics in polymer electrolyte membrane fuel cells using concentration-alternating frequency response analysis,” *J. Power Sources*, vol. 412, no. September 2018, pp. 331–335, 2019, doi: 10.1016/j.jpowsour.2018.11.065.
- [5] A. C. Antoulas, “The Loewner framework and transfer functions of singular/rectangular systems,” *Appl. Math. Lett.*, vol. 54, pp. 36–47, 2016, doi: 10.1016/j.aml.2015.10.011.
- [6] A. C. Antoulas, S. Lefteriu, and A. C. Ionita, “Chapter 8: A Tutorial Introduction to the Loewner Framework for Model Reduction,” *Model Reduct. Approx.*, pp. 335–376, 2017, doi: 10.1137/1.9781611974829.ch8.
- [7] I. V. Gosea and A. C. Antoulas, “Model reduction of linear and nonlinear systems in the Loewner framework: A summary,” *2015 Eur. Control Conf. ECC 2015*, pp. 345–349, 2015, doi: 10.1109/ECC.2015.7330568.
- [8] D. S. Karachalios, I. V. Gosea, and A. C. Antoulas, “The Loewner Framework for System Identification and Reduction,” in *Model Reduction Handbook: Volume I: System- and Data-Driven Methods and Algorithms* (Eds. Benner, P.; Schilders, W.; Grivet-Talocia, S.; Quarteroni, A.; Rozza, G. et al.). De Gruyter (accepted), 2021.
- [9] D. Hissel and M. C. Pera, “Diagnostic & health management of fuel cell systems: Issues and solutions,” *Annu. Rev. Control*, vol. 42, pp. 201–211, 2016, doi: 10.1016/j.arcontrol.2016.09.005.
- [10] J. Larminie and A. Dicks, *Fuel Cell Systems Explained*. 2003.
- [11] J. Melorose, R. Perroy, and S. Careas, *Fuel Cell Technology Reaching Towards Commercialization*, vol. 1. 2015.
- [12] J. Wu, X. Z. Yuan, H. Wang, M. Blanco, J. J. Martin, and J. Zhang, “Diagnostic tools in PEM fuel cell research: Part I Electrochemical techniques,” *Int. J. Hydrogen Energy*, vol. 33, no. 6, pp. 1735–1746, 2008, doi: 10.1016/j.ijhydene.2008.01.013.

- [13] T. Franz, "Effekt von periodischen Konzentrationsschwingungen entlang der Strömungskanäle auf die Dynamik von Polymerelektrolytmembran-Brennstoffzellen," Otto-von-Guericke-Universität Magdeburg, 2020, Master Thesis.
- [14] Z. Li, "Data-driven fault diagnosis for PEMFC systems," UNIVERSITÉ AIX-MARSEILLE, 2014, Ph.D. Thesis.
- [15] N. Wagner and K. A. Friedrich, "Dynamic Operational Conditions," in *Encyclopedia of Electrochemical Power Sources*, 2009, pp. 912–930.
- [16] A. Sorrentino, K. Sundmacher, and T. Vidakovic-Koch, "Polymer Electrolyte Fuel Cell Degradation Mechanisms and Their Diagnosis by Frequency Response Analysis Methods: A Review," *Energies*, vol. 13, no. 21, p. 5825, 2020, doi: 10.3390/en13215825.
- [17] N. Wagner, "Electrochemical Impedance Spectroscopy," in *PEM Fuel Cell Diagnostic Tools*, no. 59602, CRC Press, 2011, pp. 37–70.
- [18] S. S. Araya, F. Zhou, S. L. Sahlin, S. Thomas, C. Jeppesen, and S. K. Kær, "Fault characterization of a proton exchange membrane fuel cell stack," *Energies*, vol. 12, no. 1, 2019, doi: 10.3390/en12010152.
- [19] E. Ivers-Tiffée and A. Weber, "Evaluation of electrochemical impedance spectra by the distribution of relaxation times," *J. Ceram. Soc. Japan*, vol. 125, no. 4, pp. 193–201, 2017, doi: 10.2109/jcersj2.16267.
- [20] M. Heinzmann, A. Weber, and E. Ivers-Tiffée, "Advanced impedance study of polymer electrolyte membrane single cells by means of distribution of relaxation times," *J. Power Sources*, vol. 402, no. July, pp. 24–33, 2018, doi: 10.1016/j.jpowsour.2018.09.004.
- [21] A. Weiß, S. Schindler, S. Galbiati, M. A. Danzer, and R. Zeis, "Distribution of Relaxation Times Analysis of High-Temperature PEM Fuel Cell Impedance Spectra," *Electrochim. Acta*, vol. 230, pp. 391–398, 2017, doi: 10.1016/j.electacta.2017.02.011.
- [22] V. V. Lopes, R. A. Silva, A. Q. Novais, and C. M. Rangel, "Relaxation time distribution analysis of a polymer electrolyte fuel cell stack from its impedance response," *Cienc. e Tecnol. dos Mater.*, vol. 24, no. 3–4, pp. 193–196, 2012.
- [23] F. Fasmin and R. Srinivasan, "Review—Nonlinear Electrochemical Impedance Spectroscopy," *J. Electrochem. Soc.*, vol. 164, no. 7, pp. H443–H455, 2017, doi: 10.1149/2.0391707jes.
- [24] T. Kadyk, R. Hanke-rauschenbach, and K. Sundmacher, "Nonlinear frequency response analysis of PEM fuel cells for diagnosis of dehydration, flooding and CO-poisoning," *J. Electroanal. Chem.*, vol. 630, no. 1–2, pp. 19–27, 2009, doi: 10.1016/j.jelechem.2009.02.001.
- [25] Q. Mao, U. Krewer, and R. Hanke-rauschenbach, "Electrochemistry Communications Total harmonic distortion analysis for direct methanol fuel cell anode," *Electrochem. commun.*, vol. 12, no. 11, pp. 1517–1519, 2010, doi: 10.1016/j.elecom.2010.08.022.
- [26] A. M. Niroumand, W. Mérida, M. Eikerling, and M. Saif, "Pressure-voltage oscillations as a diagnostic tool for PEFC cathodes," *Electrochem. commun.*, vol. 12, no. 1, pp.





- 122–124, 2010, doi: 10.1016/j.elecom.2009.11.003.
- [27] I. V. Gosea, “Model order reduction of linear and nonlinear systems in the Loewner framework,” Jacobs University Bremen, January 2017, Ph.D. Thesis.
- [28] Antonio Cosmin Ionita, “Lagrange rational interpolation and its applications to approximation of large-scale dynamical systems,” Rice University, Houston, Texas, 2013, Ph.D. Thesis.
- [29] A. C. Antoulas, B. Zhu, Q. Zhang, B. York, B. W. O’Malley, and C. C. Dacso, “A novel mathematical method for disclosing oscillations in gene transcription: A comparative study,” *bioRxiv*, pp. 1–20, 2017, doi: 10.1101/151720.
- [30] M. Voigt, “Model Reduction Course,” 2019, available online at <https://www.math.uni-hamburg.de/home/voigt/modellreduktion.html>.
- [31] J. Illig, M. Ender, T. Chrobak, J. P. Schmidt, D. Klotz, and E. Ivers-Tiffée, “Separation of Charge Transfer and Contact Resistance in LiFePO<sub>4</sub> -Cathodes by Impedance Modeling,” *J. Electrochem. Soc.*, vol. 159, no. 7, pp. A952–A960, 2012, doi: 10.1149/2.030207jes.
- [32] B. Andreaus and G. G. Scherer, “Proton-conducting polymer membranes in fuel cells - Humidification aspects,” *Solid State Ionics*, vol. 168, no. 3–4, pp. 311–320, 2004, doi: 10.1016/j.ssi.2003.01.001.
- [33] A. Z. Weber *et al.*, “A Critical Review of Modeling Transport Phenomena in Polymer-Electrolyte Fuel Cells,” *J. Electrochem. Soc.*, vol. 161, no. 12, pp. F1254–F1299, 2014, doi: 10.1149/2.0751412jes.
- [34] S. Keller *et al.*, “Characteristic Time Constants Derived from the Low-Frequency Arc of Impedance Spectra of Fuel Cell Stacks,” *J. Electrochem. Energy Convers. Storage*, vol. 15, no. 2, pp. 1–10, 2018, doi: 10.1115/1.4038632.
- [35] E. Kumbur and M. Mench, “Water Management,” in *Encyclopedia of Electrochemical Power Sources*, 2009, pp. 828–847.
- [36] S. M. Rezaei Niya and M. Hoorfar, “Study of proton exchange membrane fuel cells using electrochemical impedance spectroscopy technique - A review,” *J. Power Sources*, vol. 240, pp. 281–293, 2013, doi: 10.1016/j.jpowsour.2013.04.011.
- [37] K. Wiezell, N. Holmström, and G. Lindbergh, “Studying Low-Humidity Effects in PEMFCs Using EIS II. Modeling,” *J. Electrochem. Soc.*, vol. 159, no. 8, pp. F379–F392, 2012, doi: 10.1149/2.006208jes.
- [38] A. Schiefer, M. Heinzmann, and A. Weber, “Inductive Low-Frequency Processes in PEMFC-Impedance Spectra,” *Fuel Cells*, vol. 20, no. 4, pp. 499–506, 2020, doi: 10.1002/fuce.201900212.
- [39] V. V Lopes, C. M. Rangel, and A. Q. Novais, “Electrochemical impedance spectroscopy modeling using the distribution of relaxation times and error analysis for fuel cells,” *HYCELTECH - IV Iber. Symp. Hydrog. Fuel Cells Adv. Batter.*, pp. 1–4, 2013.
- [40] “Polynomial curve fitting - MATLAB polyfit - MathWorks India.” <https://in.mathworks.com/help/matlab/ref/polyfit.html> (accessed Dec. 07, 2020).

- 
- [41] "Filtering and Smoothing Data - MATLAB & Simulink - MathWorks India." [https://in.mathworks.com/help/curvefit/smoothing-data.html?searchHighlight=data smooth&s\\_tid=srchtitle](https://in.mathworks.com/help/curvefit/smoothing-data.html?searchHighlight=data%20smooth&s_tid=srchtitle) (accessed Dec. 07, 2020).
- [42] "Smooth response data - MATLAB smooth - MathWorks India." <https://in.mathworks.com/help/curvefit/smooth.html> (accessed Dec. 07, 2020).
- [43] S. W. Smith, *The Scientist and Engineer's Guide to Digital Signal Processing*. California Technical Publishing All, 2000.
- [44] Mathuranathan, "How to Interpret FFT results - complex DFT, frequency bins and FFTShift - GaussianWaves." <https://www.gaussianwaves.com/2015/11/interpreting-fft-results-complex-dft-frequency-bins-and-fftshift/#fft> (accessed Aug. 19, 2020).
- [45] "Fast Fourier transform - MATLAB fft - MathWorks India." [https://in.mathworks.com/help/matlab/ref/fft.html?s\\_tid=srchtitle](https://in.mathworks.com/help/matlab/ref/fft.html?s_tid=srchtitle) (accessed Dec. 07, 2020).
- [46] M. Lindstrom and B. Wetton, "A comparison of Fick and Maxwell–Stefan diffusion formulations in PEMFC gas diffusion layers," *Heat Mass Transf. und Stoffuebertragung*, vol. 53, no. 1, pp. 205–212, 2017, doi: 10.1007/s00231-016-1812-7.
- [47] T. F. Fuller, "Solid - Polymer-Electrolyte Fuel Cells," University of California, 1992, Ph.D. Thesis.
- [48] T. E. Springer, T. A. Zawodzinski, and S. Gottesfeld, "Polymer Electrolyte Fuel Cell Model," *J. Electrochem. Soc.*, vol. 138, no. 8, pp. 2334–2342, 1991, doi: 10.1149/1.2085971.
- [49] J. Zhang and R. Datta, "Sustained Potential Oscillations in Proton Exchange Membrane Fuel Cells with PtRu as Anode Catalyst," *J. Electrochem. Soc.*, vol. 149, no. 11, pp. A1423–A1431, 2002, doi: 10.1149/1.1511752.
- [50] R. Hanke-Rauschenbach, M. Mangold, and K. Sundmacher, "Bistable Current-Voltage Characteristics of PEM Fuel Cells Operated with Reduced Feed Stream Humidification," *J. Electrochem. Soc.*, vol. 155, no. 2, pp. B97–B107, 2008, doi: 10.1149/1.2806064.

## 8 Appendix

### 8.1 Fourier transform (FT)

One often experiences the difficulty of transforming a time-domain signal to the frequency domain and vice versa. Fourier transform is a powerful tool for achieving this conversion and is used in many applications so many times. A time-domain signal may be continuous or discrete in signal processing and may be aperiodic or periodic. This leads to four types of Fourier transforms, which are shown in Figure 8.1 [43].

Type of Transform	Example Signal
Fourier Transform <i>signals that are continuous and aperiodic</i>	
Fourier Series <i>signals that are continuous and periodic</i>	
Discrete Time Fourier Transform <i>signals that are discrete and aperiodic</i>	
Discrete Fourier Transform <i>signals that are discrete and periodic</i>	

**Figure 8.1: Four types of Fourier transforms [43].**

For convenience, explanation here will be limited to Discrete Fourier Transform (DFT), which is widely available as part of software packages such as MATLAB, Scipy(python), etc., but one can approximate other transforms using DFT.

#### 8.1.1 Real and complex versions of transforms

There is a real version and a complex version of each of the transforms listed above. The real transform version takes in real numbers and gives two sets of real frequency domain points – one set representing coefficients over cosine basis function and the other set representing the coefficient over sine basis function. The complex version of the transforms represents positive and negative frequencies in a single array. The complex versions are flexible,

allowing it to process complex-valued signals as well as real-valued signals. The Figure 8.2 below captures the difference between real DFT and complex DFT [44].

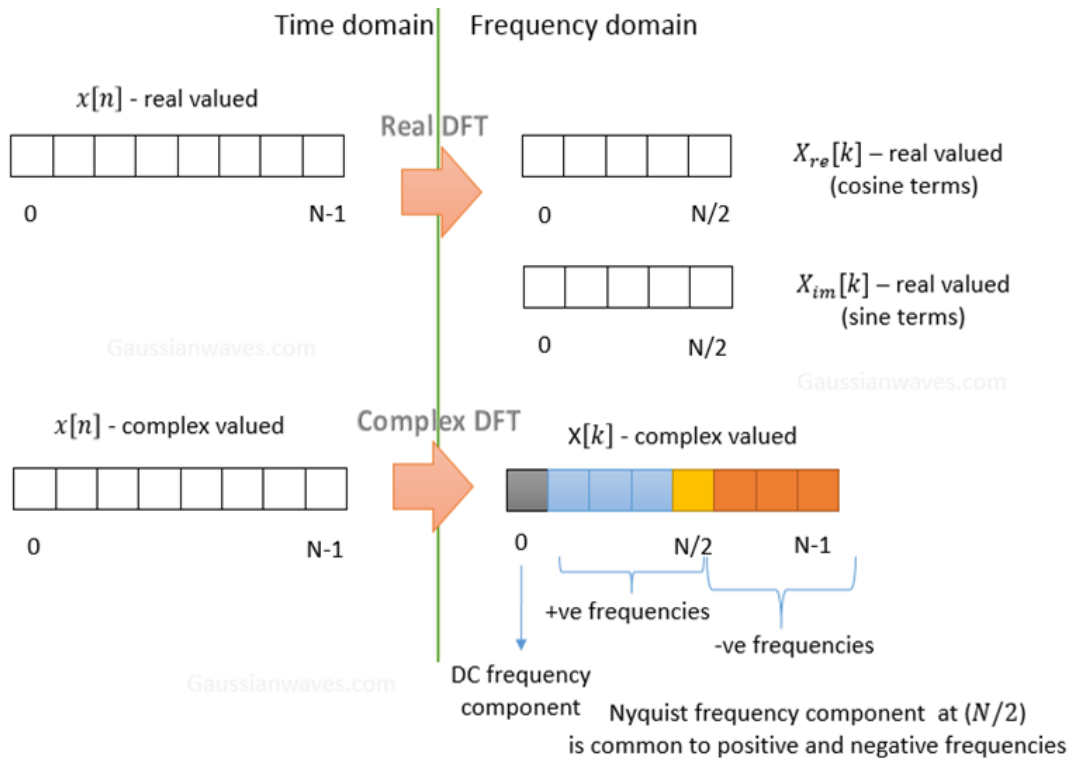


Figure 8.2: Real and complex DFT [44].

### 8.1.1.1 Real DFT

Consider the case of N-point real DFT, it takes in N samples of (real-valued) time-domain waveform  $x[n]$  and gives two arrays of length  $N/2 + 1$  each set projected on cosine and sine functions respectively.

$$X_{re}[k] = \frac{2}{N} \sum_{n=0}^{N-1} x[n] \cos\left(\frac{2\pi kn}{N}\right) \quad (8.1)$$

$$X_{im}[k] = -\frac{2}{N} \sum_{n=0}^{N-1} x[n] \sin\left(\frac{2\pi kn}{N}\right) \quad (8.2)$$

The time domain index  $n$  runs from 0 to  $N$ , the frequency domain index  $k$  runs from 0 to  $N/2$ .

### 8.1.1.2 Complex DFT

Consider the case of N-point complex DFT, it takes in N samples of (the complex-valued) time-domain waveform  $x[n]$  and produces an array  $X[k]$  of length N.

$$X[k] = \sum_{n=0}^{N-1} x[n] e^{-\frac{i2\pi}{N}kn} \quad (8.3)$$

$$X[k] = \sum_{n=0}^{N-1} x[n] \left[ \cos\left(\frac{2\pi}{N}kn\right) - i \sin\left(\frac{2\pi}{N}kn\right) \right] \quad (8.4)$$

From these equations ((8.1) and (8.2)), one can see that the real DFT is calculated by projecting the signal onto cosine and sine basis functions. However, the complex DFT (eq. (8.3)) projects the input signal onto exponential basic functions (Euler's formula combines these two concepts (see eq. (8.4))) [44].

If the input signal is a real value in the time domain, the complex DFT fills the imaginary part with zero during the calculation. The following Figure 8.3 shows how the raw FFT results are interpreted in MATLAB, which calculates the complex DFT.

The values in the arrays are interpreted as below

- X [0] represents the component of the DC frequency
- Next N/2 terms are positive frequency components with X[N/2] being the Nyquist frequency (which is equal to half of sampling frequency)
- Next N/2-1 terms are negative frequency components (note: negative frequency components are the phasors turning in the opposite direction, they can optionally be omitted depending on the application)

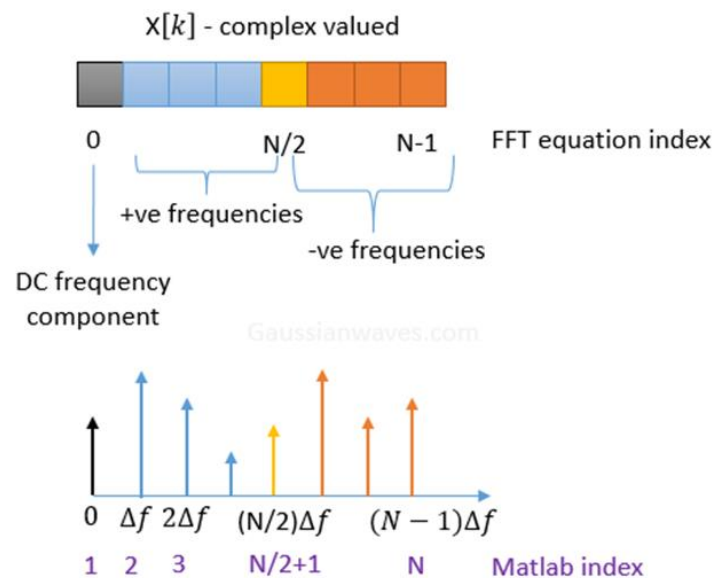


Figure 8.3: Interpretation of frequencies in complex DFT output [44].

### 8.1.2 Fast Fourier transform (FFT)

The FFT function in MATLAB is an algorithm published in 1965 by J.W. Cooley and J.W. Tuckey for the efficient calculation of the DFT. It uses the special structure of the DFT when the signal length is a power of 2. In this case, the computing complexity is significantly reduced [44].

FFT is widely used in software packages such as MATLAB, Scipy, etc. MATLAB's FFT implementation computes the complex DFT, which is very similar to the above equations except for the scaling factor. For comparison, the MATLAB's FFT implementation calculates the complex DFT and its inverse as

$$X[k] = \sum_{n=0}^{N-1} x[n] e^{-\frac{i2\pi}{N}kn} \quad (8.5)$$

$$x[n] = \frac{1}{N} \sum_{k=0}^{N-1} X[k] e^{\frac{i2\pi}{N}kn} \quad (8.6)$$

The MATLAB commands that implement the above equations ((8.5) and (8.6)) are FFT and IFFT, respectively (for details refer to [45]). The respective syntax is as follows

$$X = \text{fft}(x, N)$$

$$x = \text{ifft}(X, N)$$

### 8.1.3 Interpreting the FFT results

N-point complex DFT is computed with the FFT function. The transformation length N should cover the signal of interest otherwise we will lose some valuable information in the process of conversion to the frequency domain. However, if we know about the nature of the signal, we can select a reasonable length [44].

Each point / bin in the FFT output array is spaced by the frequency resolution  $\Delta f$ , which is calculated as

$$\Delta f = f_s / N \quad (8.7)$$

Where  $f_s$  is the sampling frequency and N is the FFT size taken into account.

#### 8.1.3.1 Extract amplitude of frequency components (amplitude spectrum)

The FFT function calculates the complex DFT and thus the results in a sequence of complex numbers of the form  $X_{re} + j X_{im}$ . The amplitude spectrum is obtained

$$|X[k]| = \sqrt{X_{re}^2 + X_{im}^2} \quad (8.8)$$



### 8.1.3.2 Extract phase of frequency components (phase spectrum)

The phase of the spectral components is calculated as

$$\angle X[k] = \tan^{-1} \left( \frac{X_{im}}{X_{re}} \right) \quad (8.9)$$

Extracting the right phase spectrum is a tricky problem. Above equation looks simple, but when calculating the inverse tangents using computers one should be careful. Function `atan()` in Matlab seems to be the obvious option for implementation. Use of `atan()` function, however, may prove inaccurate if no further precautions are taken. The `atan()` function only computes the inverse tangent over two quadrants, i.e. it will only return values within the interval of  $[-\pi/2, \pi/2]$ . Hence the phase needs to be properly unwrapped. One can easily solve this problem by using `atan2( $X_{im}, X_{re}$ )` function to calculate the inverse tangent over all the four quadrants [44].

## 8.2 Experimental parameters and model description

### 8.2.1 Experimental parameters

Table 8.1 describes the normal operating parameters of the PEMFC, which are also used in the simulation.

**Table 8.1: Normal operating conditions of the PEMFC.**

Operating Parameters	Unit	Value
Temperature	K	353
Pressure	Pa	$10^5$
<b>Cathode inputs:</b>		
Volumetric flow rate of air	$\text{m}^3\text{s}^{-1}$	$10^{-5}$
Dew point temperature	K	328
Oxygen partial pressure	Pa	$1.7713 \times 10^4$
Water partial pressure	Pa	$1.565 \times 10^4$
Relative air humidity	%	33
<b>Anode inputs:</b>		
Volumetric flow rate of $\text{H}_2$	$\text{m}^3\text{s}^{-1}$	$1.42 \times 10^{-5}$
Dew point temperature	K	328
Hydrogen partial pressure	Pa	$8.435 \times 10^4$
Water partial pressure	Pa	$1.565 \times 10^4$
Relative air humidity	%	33
<b>Fuel cell parameters:</b>		
Porosity of GDL	-	0.7
Thickness of GDL	m	$190 \times 10^{-6}$
Thickness of Membrane	m	$127 \times 10^{-6}$
Active Area	$\text{m}^2$	$26 \times 10^{-4}$

## 8.2.2 Model description

A simplified view of the structure and the individual segments that comprise a PEM fuel cell is shown in Figure 8.4. In the following model description, all the main dynamic phenomena are included that comprise (i) the charging (or discharging) of the double layer at the electrode surface, (ii) the mass transport of the gaseous reactants, and (iii) the water transport in the Nafion membrane.

The dynamic mass balances were formulated for all the species that are present in all the segments of the cell. Concentration variations taken into account along the sandwich coordinate  $x$ , while the composition along the axis coordinate  $y$  is considered constant. Moreover, isothermal and isobaric conditions are assumed inside the cell.

In order to correlate the effect of the various transport phenomena with the electrical responses, a dynamic charge balance on the catalyst surface was expressed. More realistic boundary conditions, which relate to the dynamics of the different compartments of the cell was formulated. In the following tables, detailed information on the model equations for the different domains of the cell, the boundary conditions, and the values of the model parameters are given. For details, refer to this paper [3].

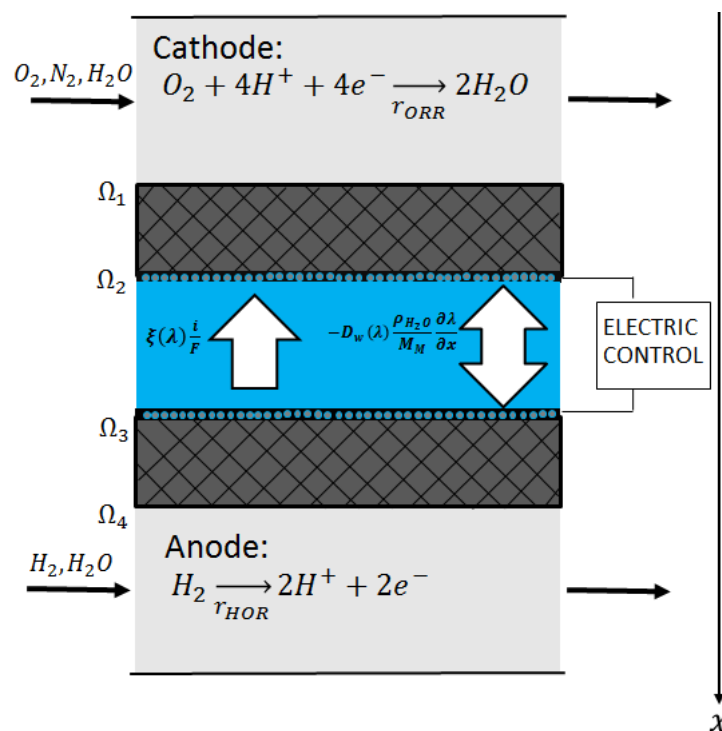


Figure 8.4: A scheme of a PEMFC [3].

Table 8.2: Balance equations of the cell.

	Equations	References
Mass balance in CH	$V \frac{dP_{\alpha}^{CH}}{dt} = P_{\alpha,in}^{CH} F_{in} - P_{\alpha}^{CH} F_{out} + RTA J_{\alpha}   \Omega_i, t \quad i = 1,4$	[3]
Mass balance in GDL	$\frac{\partial P_{\alpha}^{GDL}}{\partial t} = D_{\alpha,\beta}^{eff} \frac{\partial^2 P_{\alpha}^{GDL}}{\partial x^2}$	[46]
Mass balance in membrane	$\frac{\rho_M}{M_M} \frac{\partial \lambda_M}{\partial t} = - \frac{\partial N_W}{\partial x}$	[3]
Charge balance for anode	$i = C_{dl}^a \frac{d\eta_a}{dt} + 2Fr_{HOR}$	[3]
Charge balance for cathode	$i = C_{dl}^c \frac{d\eta_c}{dt} - 4Fr_{ORR}$	[3]
Potential loss due to Ohmic resistance	$\Delta\Phi_M = i \int_0^{l_M} \frac{1}{k_M(\lambda_M)} dx$	[3]
Polarization equation	$U = U_{OCP} - \eta_a + \eta_c - \Delta\Phi_M$	[3]

Table 8.3: Constitutive equations.

	Equations	References
Effective diffusivity	$D_{\alpha,\beta}^{eff} = \epsilon^{1.5} D_{\alpha,\beta}$	[3]
Water flow in membrane	$N_W = -D_W(\lambda_M) \frac{\rho_M}{M_M} \frac{\partial \lambda_M}{\partial x} - \xi(\lambda_M) \frac{i}{F}$	[3]
Water diffusivity in membrane	$D_W(\lambda_M) = \lambda_M D_W^0 \exp\left(-\frac{2436}{T}\right)$	[47]
Electro-osmotic drag constant	$\xi(\lambda_M) = K_M \lambda_M$	[48]
Membrane conductivity	$k_M = (0.005139\lambda_M - 0.00326) \exp\left(1268 \left(\frac{1}{303} - \frac{1}{T}\right)\right)$	[48]
Kinetic equation for HOR	$r_{HOR} = \frac{K_{HOR} (P_{H_2}^{CL})^{1/2}}{2\sqrt{K_{H_2,ad}}} \sinh\left(\frac{\alpha_a F}{RT} \eta_a\right)$	[49], [50]
Kinetic equation for ORR	$r_{ORR} = \frac{P_{O_2}^{CL}}{RT C_{O_2,ref}} t_{ccl} \frac{a_{i_0}}{4F} \exp\left(-\frac{\alpha_c F}{RT} \eta_c\right)$	[49], [50]

The model contains six-second order partial differential equations (PDE). Hence, twelve boundary conditions (BC) are required to solve these equations.

**Table 8.4: Boundary conditions.**

Assumptions	Equations	References
The continuity of the partial at the GDL/CH interface of the cathode.	$P_{\alpha}^{GDL} _{x=\Omega_1,t} = P_{\alpha}^{CH}$ where $\alpha = O_2, N_2, H_2O$	[3]
The continuity of the partial at the GDL/CH interface of the anode.	$P_{\alpha}^{GDL} _{x=\Omega_4,t} = P_{\alpha}^{CH}$ where $\alpha = H_2, H_2O$	[3]
Oxygen diffusion equals the rate of oxygen consumption	$-\frac{D_{O_2,air}^{eff}}{RT} \frac{\partial P_{O_2}^{GDL}}{\partial x} \Big _{x=\Omega_2,t} = r_{ORR}$	[3]
Nitrogen does not participate in the ORR	$-\frac{D_{N_2,air}^{eff}}{RT} \frac{\partial P_{N_2}^{GDL}}{\partial x} \Big _{x=\Omega_2,t} = 0$	[3]
The steady-state water balance at cathode side	$-\frac{D_{H_2O,air}^{eff}}{RT} \frac{\partial P_{H_2O}^{GDL}}{\partial x} \Big _{x=\Omega_2,t} - D_W(\lambda_M) \frac{\rho_M}{M_M} \frac{\partial \lambda_M}{\partial x} \Big _{x=\Omega_2,t}$ $= 2r_{ORR} + \xi(\lambda_M) \frac{i}{F}$	[3]
Hydrogen diffusion equals the rate of Hydrogen consumption	$-\frac{D_{H_2,H_2O}^{eff}}{RT} \frac{\partial P_{H_2}^{GDL}}{\partial x} \Big _{x=\Omega_3,t} = r_{HOR}$	[3]
The steady-state water balance at anode side	$-\frac{D_{H_2O,H_2}^{eff}}{RT} \frac{\partial P_{H_2O}^{GDL}}{\partial x} \Big _{x=\Omega_3,t}$ $= -D_W(\lambda_M) \frac{\rho_M}{M_M} \frac{\partial \lambda_M}{\partial x} \Big _{x=\Omega_3,t}$ $+ \xi(\lambda_M) \frac{i}{F}$	[3]
At the catalyst/Nafion interface, the water vapour is considered in equilibrium with the water inside the Nafion membrane,	$\lambda_W = 0.043 + 17.81 \frac{P_{H_2O}^{CL}}{P_{sat}} \Big _{x=\Omega_i,t} - 39.85 \frac{P_{H_2O}^{CL}}{P_{sat}} \Big _{x=\Omega_i,t}^2$ $+ 36 \frac{P_{H_2O}^{CL}}{P_{sat}} \Big _{x=\Omega_i,t}^3$ where $i = 3,4$	[48]

Table 8.5: Model parameters.

Quantity	Unit	Value
Double-layer capacitance for cathode and anode $C_{dl}$	F m <sup>-2</sup>	100
Reference concentration O <sub>2</sub> $C_{O_2,ref}$	mol m <sup>-3</sup>	40
Product of specific catalyst area and exchange current $ai_0$	A m <sup>-3</sup>	10 <sup>4</sup>
Cathode catalyst layer thickness $t_{ccl}$	m	10 <sup>-5</sup>
Kinetic constant for hydrogen oxidation $K_{HOR}$	mol m <sup>-2</sup> s <sup>-1</sup>	4.15 × 10 <sup>-1</sup>
Kinetic constant for hydrogen adsorption $K_{H_2, ad}$	Pa <sup>-1/2</sup>	5.07 × 10 <sup>4</sup>
Charge transfer coefficient at the anode $\alpha_a$	-	0.5
Charge transfer coefficient at the cathode $\alpha_c$	-	0.55
Effective diffusivity for O <sub>2</sub> $D_{O_2, N_2}^{eff}$	m <sup>2</sup> s <sup>-1</sup>	6.69 × 10 <sup>-7</sup>
Effective diffusivity for H <sub>2</sub> O $D_{H_2O, N_2}^{eff}$	m <sup>2</sup> s <sup>-1</sup>	6.6 × 10 <sup>-6</sup>
Open circuit potential $U_{OCP}$	V	1.2
Volume of the channel $V$	m <sup>3</sup>	7.2 × 10 <sup>-6</sup>

### 8.3 Different verifications

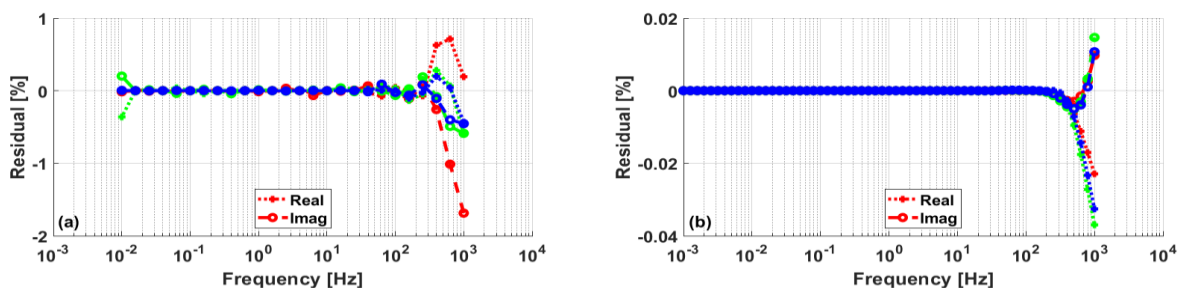


Figure 8.5: Relative residuals corresponding to the experimental (a) and simulated (b) EIS spectra in Figure 4.12.

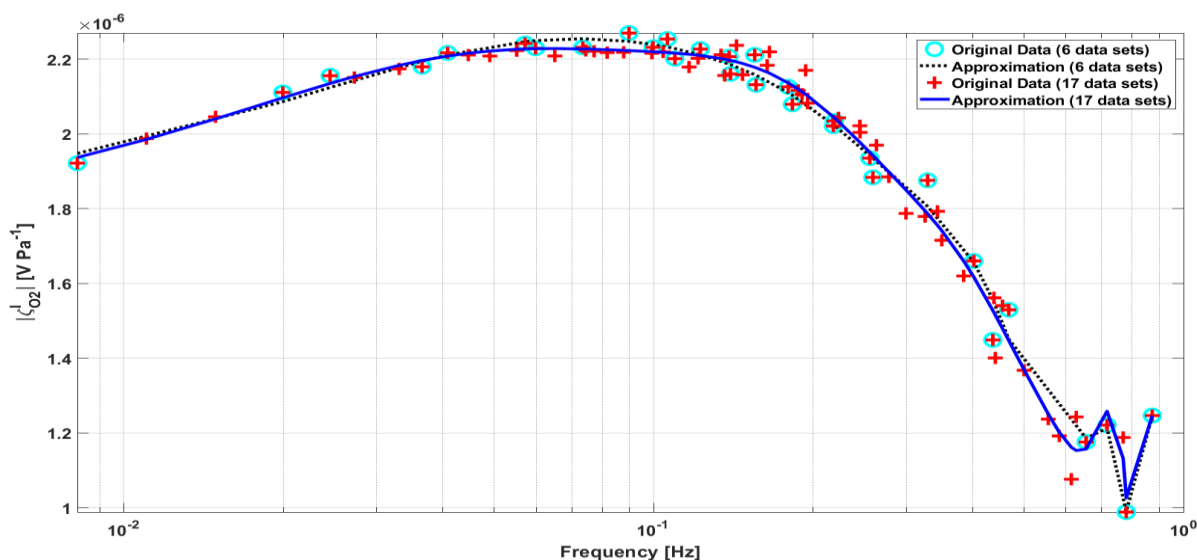


Figure 8.6: Magnitude spectra of galvanostatic cFRA O<sub>2</sub> for both all-17 data sets and six data sets (Verification with other cFRA experimental data).

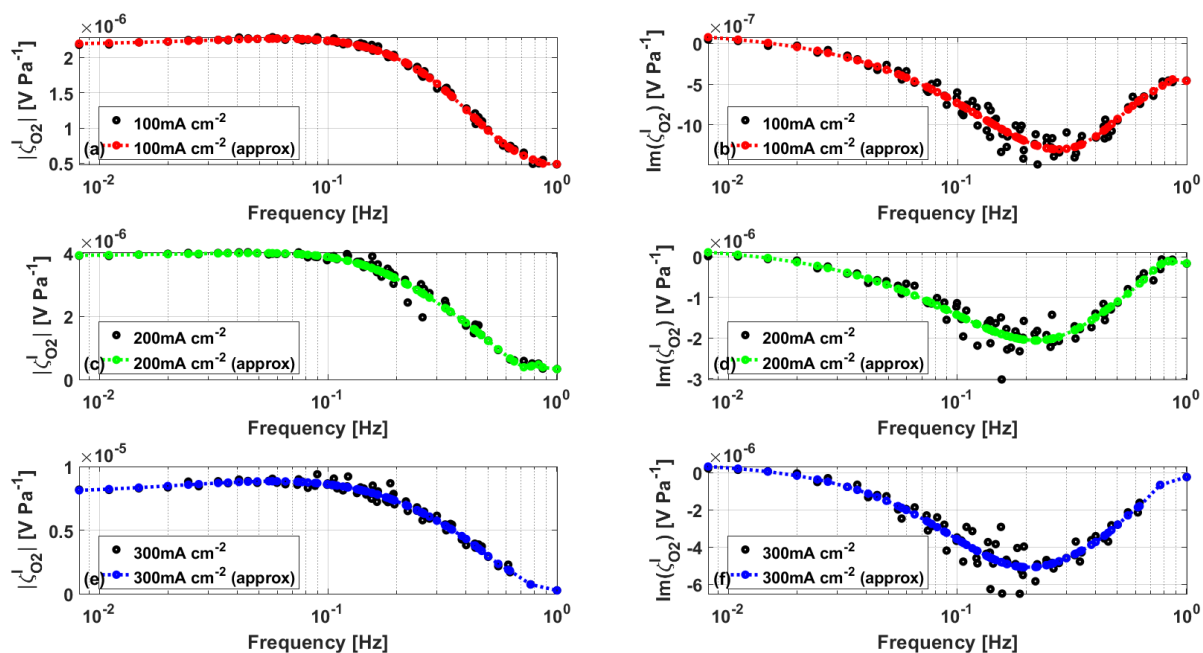


Figure 8.7: Original data of Experimental cFRA  $O_2$  spectra shown in Figure 5.9 (a-b) under galvanostatic control for 100, 200, and 300  $mA\ cm^{-2}$ .

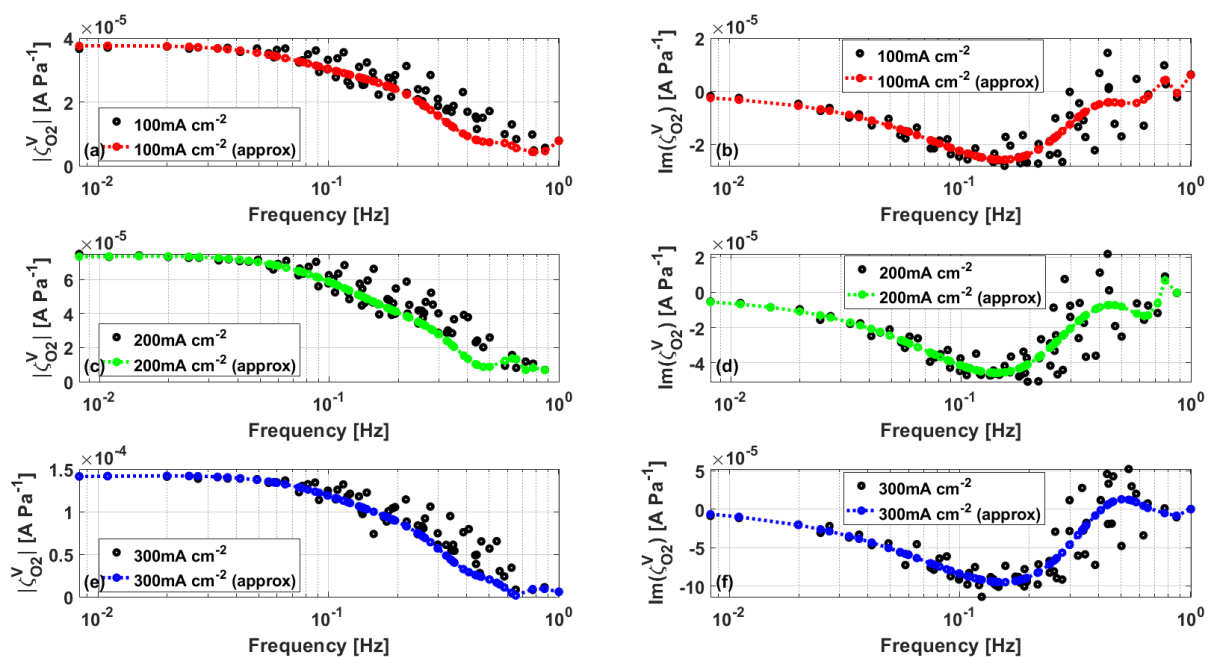


Figure 8.8: Original data of Experimental cFRA  $O_2$  spectra shown in Figure 5.9 (c-d) under voltastatic control for 100, 200, and 300  $mA\ cm^{-2}$ .

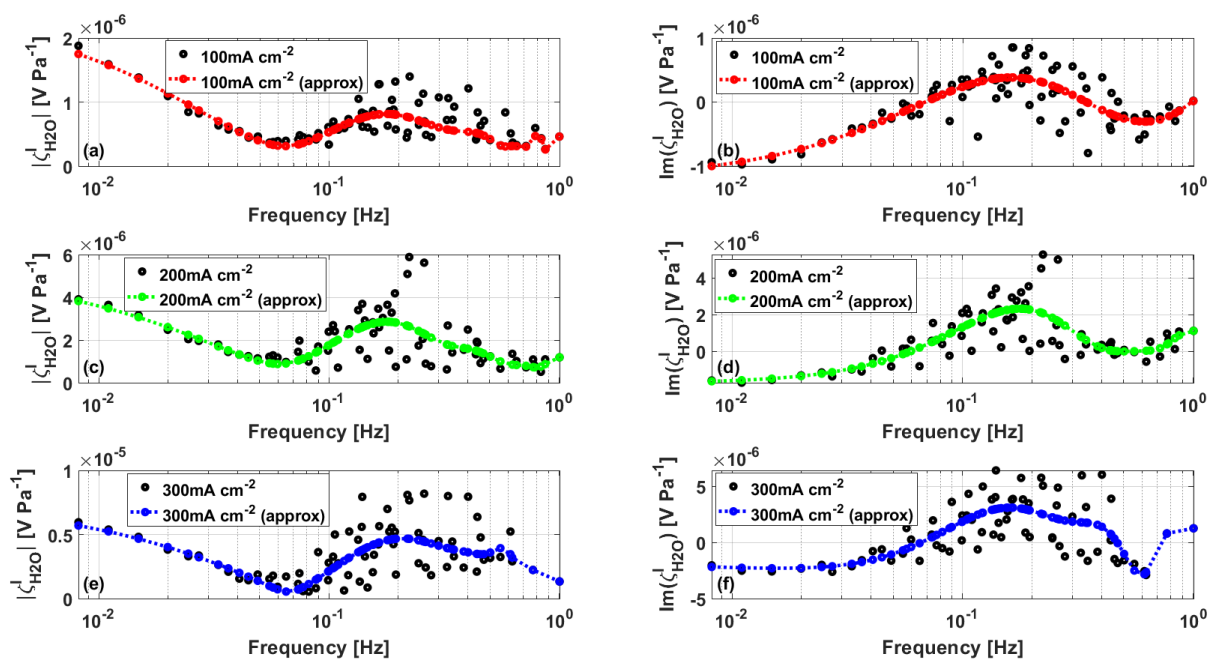


Figure 8.9: Original data of Experimental cFRA  $\text{H}_2\text{O}$  spectra shown in Figure 5.13 (a-b) under galvanostatic control for 100, 200, and 300  $\text{mA cm}^{-2}$ .

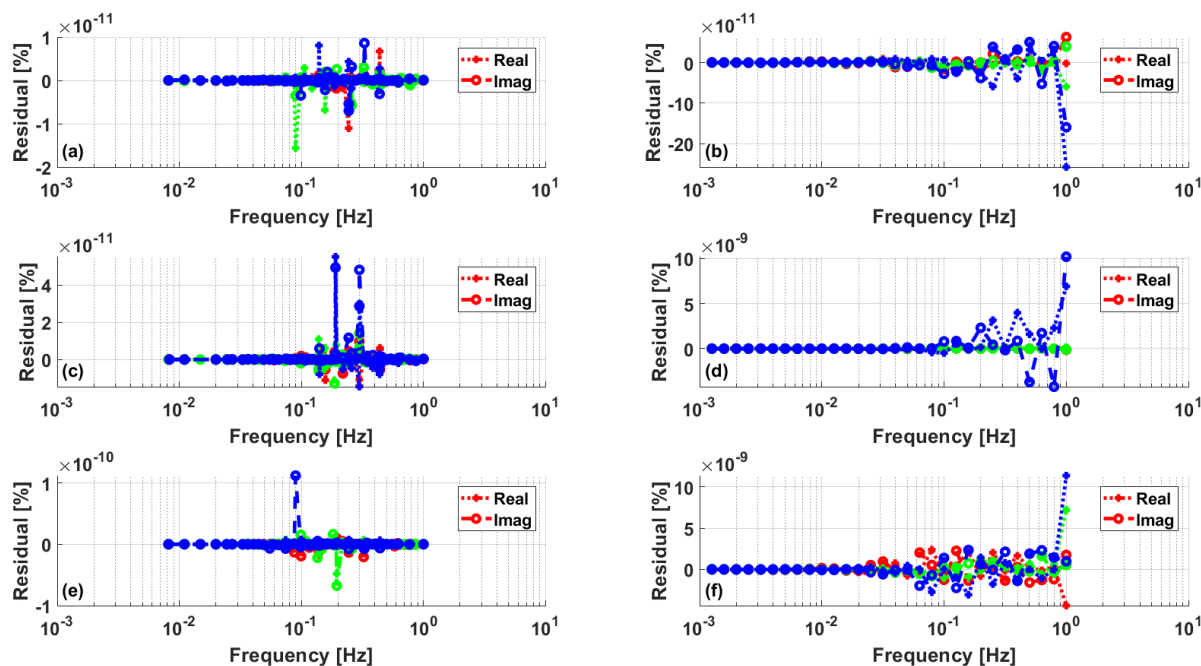


Figure 8.10: Relative residuals corresponding to the experimental (a, c, e) and simulated (b, d, f) cFRA spectra shown in Figure 5.9, Figure 5.11, and Figure 5.13. (a, b) cFRA  $\text{O}_2$  under galvanostatic control, (c, d) cFRA  $\text{O}_2$  under voltastatic control, and (e, f) cFRA  $\text{H}_2\text{O}$  under galvanostatic control.